An improved carbon-dioxide thermodynamic model applied for reservoir simulation

N.W. Morshuis

Implementation of an improved thermodynamic model in Delft Advanced Terra Simulator (DARTS) and an investigation into the effects of impurities on gas plume behaviour.

An improved carbon-dioxide thermodynamic model applied for reservoir simulation

by

N.W. Morshuis

to obtain the degree of Master of Science
at the Delft University of Technology,
to be defended publicly on Friday November 22e, 2019 at 1:30 PM.

Student number:	4228952	
Project duration:	December 1, 2018 – November 22, 2019	
Thesis committee:	Prof. dr. ir. D. V. Voskov,	TU Delft, supervisor
	Prof. dr. ir. F. C. Vossepoel,	TU Delft
	Prof. dr. ir. K. H. A. A. Wolf,	TU Delft
	PhD. X. Lyu,	TU Delft

An electronic version of this thesis is available at `http://repository.tudelft.nl/`.

Abstract

Geological storage of CO_2 is a crucial and upcoming technology to reduce anthropogenic greenhouse gas emissions. Due to the buoyant characteristic of injected gas, the security of underground storage is a major concern. To asses the security of CO_2 storage, an accurate prediction of the gas plume behaviour is essential. In this study, a fully physical 2D model is developed to describe gas behaviour in a saline aquifer. In particular, we investigate the effect of gas impurities on injectivity, macroscopic dissolution and resulting plume migration. The model includes an investigation of 4-component buoyancy driven multiphase convective flow with miscible convective mixing. For an accurate description of the phase behaviour, a recently developed thermodynamic model based on a combination of cubic Equation of state with activity model has been implemented. The implemented thermodynamic model includes a specific description for the behaviour of water and an activity model describing component behaviour of the aqueous phase making this model more accurate than conventional cubic EoS. The phase behaviour based on this thermodynamic model and a consistent set of physical properties have been implemented in Delft Advance Research Terra Simulator, a new simulation framework developed at TU Delft. The results show that the presence of the gas impurities (tested here) have a negative effect on the solubility of CO_2 which in turn reduces the security of gas storage in saline aquifers and increase the risk of leaking. This is the first time when this accurate physical model is applied for large-scale simulation of CO_2 sequestration. Additionally a framework regarding the energy cost of the total CO_2 sequestration process, from separation to injection, is implemented.

Acknowledgements

First and foremost, I would like to express my sincere gratitude to the supervisor of my project Dr. Denis Voskov for his time, support, knowledge and most importantly his enthusiasm to tackle challenging problems. Secondly, I want to give my special thanks to PhD. Xiaocong Lyu for his advice and support on using the DARTS reservoir simulator and resolving technical difficulties I encountered. I want to thank Dr. Femke Vossepoel for her advice on structuring my thesis and feedback on the report. Lastly, I want to thank Dr. Karl-Heinz Wolf for his role in the defense committee and providing his informative feedback on the project.

This project has been a long and challenging journey which I would not have been able to complete without the continuous support I have received from my family and friends. I want to give a special thanks to my parents, my father for providing me with motivation and my mother for putting my goals into perspective. Without them, this would never have been possible. I want to thank my mates from “Huize Stier” for the time they took (or were forced) to listen to my complaints and providing their reflections.

Contents

List of Figures xi

List of Tables xv

1 Introduction 1
- 1.1 Effect and Consequences of Greenhouse Gas Emissions . . . 1
  - 1.1.1 History. . . . 1
  - 1.1.2 International Agreements and Mitigation of Anthropogenic Emissions . . . 1
- 1.2 Carbon Capture Storage . . . 2
- 1.3 Behaviour of injected CO_2 gas streams . . . 2
  - 1.3.1 Thermodynamic Model . . . 4
  - 1.3.2 Numerical Modeling . . . 5
- 1.4 Msc Thesis research project . . . 5
  - 1.4.1 Motivation of this research . . . 5
  - 1.4.2 Assignment description and Research question . . . 5
  - 1.4.3 Outline of the thesis . . . 6

2 Literature Study 7
- 2.1 Capture & Separation Processes . . . 7
  - 2.1.1 Capture . . . 7
  - 2.1.2 Separation Techniques . . . 8
- 2.2 Impurities from different Carbon Capture streams . . . 10
  - 2.2.1 Classes of impurities . . . 10
  - 2.2.2 Post-Combustion Capture impurities . . . 10
  - 2.2.3 Pre-combustion (IGCC) Capture Impurities . . . 11
  - 2.2.4 Oxy-fuel Combustion and Capture Impurities . . . 12
- 2.3 Summary and relation to further chapters . . . 12

3 Physics 15
- 3.1 Physics of CO_2 injection and post-injection processes . . . 15
- 3.2 Model Description . . . 15
  - 3.2.1 Components and Phases . . . 16
  - 3.2.2 Modelling processes and assumptions . . . 16
- 3.3 Governing equations . . . 17
  - 3.3.1 Mass balance equation. . . . 17
  - 3.3.2 Thermodynamic relations . . . 17
  - 3.3.3 Closing relations . . . 18
- 3.4 Delft Advance Research Terra Simulator (DARTS) . . . 18
  - 3.4.1 Nonlinear Formulation . . . 18
  - 3.4.2 Operator Based Linearization . . . 19

4 Thermodynamic Model 21
- 4.1 Phase Partitioning - Negative Flash . . . 21
- 4.2 Solving Thermodynamic phase Equilibrium . . . 22
  - 4.2.1 Conventional Fugacity-Fugacity Models. . . . 22
  - 4.2.2 Fugacity-Activity Model. . . . 23
  - 4.2.3 Initial K-value estimation . . . 25

5 **Physical properties** 27
- 5.1 Flow Properties . . . 27
  - 5.1.1 Porosity . . . 27
  - 5.1.2 Permeability and Relative Permeability . . . 27
  - 5.1.3 Capillary pressure . . . 28
  - 5.1.4 Diffusion. . . . 28
- 5.2 Phase Properties . . . 29
  - 5.2.1 Aqueous Phase Properties. . . . 29
  - 5.2.2 Non-Aqueous Phase Properties . . . 31

6 **Process Energy Framework** 33
- 6.1 Introduction to Framework . . . 33
  - 6.1.1 Power Consumption of CO_2 Capture and Purification . . . 33
  - 6.1.2 Power Consumption of Transportation and Sequestration Stage . . . 34
  - 6.1.3 Process Energy Model - Generic model. . . . 35

7 **Results** 39
- 7.1 Validations . . . 39
  - 7.1.1 Validation F-A Thermodynamic model. . . . 39
  - 7.1.2 Validation of phase property correlations . . . 42
- 7.2 Reservoir Model . . . 45
- 7.3 Convective mixing . . . 46
- 7.4 Gas Injection Results. . . . 46
- 7.5 Post-Injection Plume Migration Results . . . 49
  - 7.5.1 CO_2 plume migration for buoyancy dominated regime . . . 49
  - 7.5.2 CO_2 plume migration for full physics . . . 50
  - 7.5.3 Plume with impurities for buoyancy dominated regime . . . 52
  - 7.5.4 Plume with impurities for full physics . . . 52
- 7.6 Behaviour of impure components . . . 53
- 7.7 Process power consumption . . . 54
  - 7.7.1 Natural Gas fired powerplant and post-combustion MEA separation . . . 54
  - 7.7.2 Coal fired powerplant and post-combustion MEA separation . . . 56

8 **Discussion** 57

9 **Conclusion** 59

10 **Recommendations and Future Work** 61

A **Appendix chapter 4 - thermodynamic model** 63
- A.1 Derivation of Fugacity-Activity equilibrium definition . . . 63
- A.2 Derivation of water equilibrium constant. . . . 64
- A.3 Derivation of Henry's Constant . . . 64
- A.4 Derivation of Activity Coefficient . . . 65
- A.5 Derivation of empirical parameters for initial k-value estimation . . . 67

B **Appendix chapter 5 - Physical Properties** 69
- B.1 Derivation of Brine Density. . . . 69
  - B.1.1 Empirically Derived Parameters . . . 69
- B.2 Derivation of parameters for aqueous phase viscosity . . . 70

C **Appendix chapter 6** 73
- C.1 Validation of Thermodynamic model. . . . 73
- C.2 Additional plume migration results. . . . 74
  - C.2.1 Impure gas plume migration . . . 74
  - C.2.2 Pure CO_2 gas plume migration . . . 75

Bibliography 77

Nomenclature

Physical Constants

g	Gravitational acceleration	$9.81\ m/s^2$
R	Gas constant	$84.144598\ cm^3 \cdot bar \cdot K^{-1} \cdot mol^{-1}$

Greek symbols

γ	activity coefficient	[-]
μ	Viscosity	cp
ω	Accentric factor	[-]
Φ	Fugacity coefficient	[-]
ϕ	Porosity	[-]
ρ	Density	m^3/kg

Other Symbols

c_r	Rock compressibility	[-]
f	Fugacity	
h	Henry's constant	
i	Superscript for component	
j	Superscript for phase, gaseous (g) or aqueous (Aq)	
k	Absolute permeability	m^2
k_r	Relative permeability	[-]
l	Total flux	
m	Total mass	
p	Pressure in	bar
Pc	Critical pressure	
q	Source or sink term	
S	Saturation	[-]
S_e	Effective saturation	[-]
$S_{g,r}$	Residual gas saturation	[-]
$S_{w,c}$	Connate water saturation	[-]
T	Temperature	$Kelvin$
Tc	Critical temperature	
u	Darcy velocity	m^2/s

x	Liquid mol fraction	[-]
y	Vapour mol fraction	[-]
z	Overall composition	[-]
D	Diffusion coefficient	m^2/day
J	Diffusion-dispersion tensor	
K	Thermodynamic Equilibrium constant	[-]

List of Figures

1.1 A schematic overview of the CCS process chain [45] 3
1.2 A basic overview of the various mechanisms for trapping CO_2 and the related security with time [27] 4

2.1 Pro's and con's of capture technologies [3] 8
2.2 Classes of potential CO_2 impurities by origin, [46] 11

4.1 Schematic overview of the Fugacity-Activity model 26

5.1 Relative permreability curves for the aqueous and gaseous phase with a residual saturation of both phases at 0.2 [-]. 28

6.1 Schematic overview of the functions used to determine the power consumption of each stage in the CCS process 36
6.2 Schematic overview of generic model to determine the total power consumption of the CCS process 37

7.1 Validation of liquid mol fraction CO_2 for pressures up to 650 bars, at 90 degrees C and at 2 molal NaCl salinity. (a) Results of developed F-A model, (b) Results found in literature [58] 39
7.2 Validation of liquid mol fraction CO_2 and gaseous mol fraction H_2O over pressur at 25 degrees C in pure water. (a) Results of developed F-A model, (b) Results found in literature, [58] 40
7.3 Validation of liquid mol fraction CO_2 during injection of CO_2, CH_4, H_2S mixture with mol fraction of 0.6, 0.3 and 0.1 respectively. (a) Result of developed F-A model, (b) Results found in literature [58] 40
7.4 Validation of liquid mol fractions of pure H_2S injection over pressure at 60 and 90 degrees C for a range of brine salinity's. (a) & (b) show the results generated by the developed F-A model, (c) & (d) show the results found in literature [58] . 41
7.5 Validation of the solubility of CO_2 with presence of single component impurities at 50 $°C$, (a) show the results generated by the developed F-A model, (b) show the results found in literature [58] 42
7.6 Validation of the density of the aqueous phase for a range of CO_2 liquid mol fractions in pure water,at 22$°C$. (a) Results generated by the developed model, (b) Results from literature [25] 42
7.7 Validation of the aqueous phase viscosity over temperature for pure water (H_2O), saline water (H_2O+NaCl) and an aqueous saline solution including dissolved CO_2 (H_2O+NaCl+CO_2) at conditions shown in figure. (a) shows the results generated by the developed in the model, (b) show the results found in literature, [4] . . . 43
7.8 Validation of the brine viscosity over pressures for varying temperatures and salinity's. (a) & (b) show the resutls generated by the model, (c) & (d) show the results found in literature, Mao and Duan [42] 43
7.9 Validation of the non-aqueous phase density for pressure up to 800 bars and at 35 and 70$°C$ and no salinity. (a) Result generated by developed F-A model in combination with the molar volume from PR EoS. (b) Results from literature Shabani and Vilcáez [49] 44
7.10 Visual overview of the two dimensional reservoir models used for simulation. . 45

7.11 Results of convective behaviour of gas plume, shown by the dissolved CO_2 profile (x_{CO_2}). Here gas plume consists of multiple components with initial composition of [0.8, 0.09, 0.09]. Modeled using a Time-Step of 10 days and a Diffusion coefficient of 2.5e-9 m^2/day 46
7.12 Resulting CO_2 composition profiles of gas injection for pure CO_2 (a,b) and impure gas stream (c,d). Note that figures b and d are zoomed in versions of figures a and c. Injection composition of the gas mixture is CO_2, N_2, CH_4, z=[0.8, 0.09, 0.09]. 47
7.13 Resulting pressure profile of gas injection for pure CO_2 and impure gas stream. 47
7.14 Resulting gas saturation and CO_2 dissolution profiles for gas injection of pure CO_2 and gas mixture. Note that all these figure are zoomed in simimlar to figure 7.12b, d. Injection composition of the gas mixture is [0.8, 0.09, 0.09]. 48
7.15 Results of plume migration shown by gas saturation (on the left) and dissolved CO_2 (on the right) profile without accounting for diffusion and capillarity over a range of time periods after injection. Here only pure CO_2 is injected. 49
7.16 A close up of the saturation and composition profile of CO_2 at 100 years after injection. Here cells bounding injection exceed gas saturation limit of 0.8 [-]. . 50
7.17 Figure (a) shows the gas saturation profile at 2000 years after injection and figure (b) gives a detailed, zoomed in, presentation of the unphysical gridcells. . 50
7.18 Results of plume migration shown by gas saturation (on the left) and dissolved CO_2 (on the right) profile accounting for gravity, diffusion and capillarity over a range of time periods after injection. Here only pure CO_2 is injected. 51
7.19 Results of plume migration shown by the gas saturation and dissolved CO_2 profile for a range of periods after injection. Here impure mixture has composition [CO_2, N2, CH4], z=[0.8, 0.09, 0.09]. 52
7.20 Results of plume migration accounting for gravity, diffusion and capillarity up to 2000 years after injection. Here impure gas mixture of [CO2, N2, CH4], with composition [0.8, 0.09, 0.09] is injected. 53
7.21 Results of the behaviour of impurities N_2 and CH_4, accounting for gravity and Diffusion at 2000 years after injection. Here impure mixture is [CO2, N2, CH4], [0.8, 0.09, 0.09]. 53
7.22 Results of the behaviour of impurities N_2 and CH_4, accounting for gravity, diffusion and Capillarity at 2000 years after injection, with 5 years of gas injection as input. Here impure mixture [CO2, N2, CH4], [0.8, 0.09, 0.09] is injected into an aquifer with 0 molal NaCl salinity 54
7.23 Results of power consumption (in [MW]) of the CCS process chain using natural gas fired power-plant and MEA separation. 55
7.24 Results of power consumption CCS process chain using coal gas fired power-plant and MEA separation. 56

C.1 Validation of liquid mol fraction N_2 at 60 degrees C and gaseous mol fraction H_2O at 366.45 Kelvin. (a) & (b) show the results generated by the developed F-A model, (c) & (d) show the results found in literature, [58] 73
C.2 Validation of liquid mol fractions of CH_4 for a range of salinity's at 60 degrees C and vapour mol fractions of H_2O at 377.59 kelvin. (a) & (b) show the results generated by the developed F-A model, (c) & (d) show the results found in literature, [58] 74
C.3 Composition, pressure,saturation and dissolved CO_2 profiles for post-injection migration for an impure CO_2 gas mixture. Results include gravity, diffusion and capillarity physics. Gas mixture is consist of CO_2, N_2 and CH_4, [0.8, 0.09, 0.09]. 74
C.4 Phase density profiles for post-injection migration for an impure CO_2 gas mixture. Results include gravity, diffusion and capillarity physics. Gas mixture is consist of CO_2, N_2 and CH_4, [0.8, 0.09, 0.09]. 75
C.5 Viscosity profiles for post-injection migration for an impure CO_2 gas mixture. Results include gravity, diffusion and capillarity physics. Gas mixture is consist of CO_2, N_2 and CH_4, [0.8, 0.09, 0.09]. 75

C.6 Relative permeability profiles for post-injection migration for an impure CO_2 gas mixture. Results include gravity, diffusion and capillarity physics. Gas mixture is consist of CO_2, N_2 and CH_4, [0.8, 0.09, 0.09]. 75
C.7 Composition, pressure,saturation and dissolved CO_2 profiles for post-injection migration for pure CO_2 gas. Results include gravity, diffusion and capillarity physics. 75
C.8 Phase density profiles for post-injection migration for pure CO_2 gas. Results include gravity, diffusion and capillarity physics. 76
C.9 Viscosity profiles for post-injection migration for pure CO_2. Results include gravity, diffusion and capillarity physics. 76
C.10Relative permeability profiles for post-injection migration for pure CO_2. Results include gravity, diffusion and capillarity physics. 76

List of Tables

2.1 Classes of potential CO_2 impurities for Amine and MEA separation of Post-Combustion capture [46] 11
2.2 Impurities resulting from selexol and rectisol separations in pre-combustion of pulverised coal, [46] 12
2.3 Impurities resulting from oxy-fuel combustion, [6] 12

7.1 Dimensions Reservoir models 45
7.2 inputs for the reservoir model 46
7.3 Inputs for power consumption model. (Here subscript *sc* implies super-critical conditions.) 55

A.1 The calibrated input parameters for Henry's constant for various components . 65
A.2 The Calibrated second-order interaction parameters (λ) for various components used for calculation of the activity coefficient. 66
A.3 The Calibrated second-order interaction parameters (ζ) for various components used for calculation of the activity coefficient. 66
A.4 Empirical parameters used in equations A.29 and A.30 67
A.5 Empirical parameters used in equations A.32 67

B.1 Coefficients for equation of state for pure water 70
B.2 Coefficients for Brine compressibility 70
B.3 Coefficients for density of brine as function of temperature at 70 MPa 70
B.4 Empirical input constants for equations B.9 and B.10 71

1

Introduction

1.1. Effect and Consequences of Greenhouse Gas Emissions

Scientific research has shown that global temperatures have increased substantially and the majority of scientists agree that this is directly linked to the emission of greenhouse gasses such as carbon dioxide [48]. In this section a short overview is given of the research done on climate change and how it is caused by greenhouse gas emission.

1.1.1. History

In 1827 J. Fourier, a French mathematician and physicist, showed that the temperature of the Earths atmosphere should be lower than it actually is if solar radiation was its only source of heat. He was the first to understand that certain gasses in our atmosphere help to keep our planet warm by interfering with escaping radiation. He argued that the earths atmosphere keeps our planet warmer than expected in the vacuum of space, which was the first step to the concept of the greenhouse effect [20].

Half a century later in 1896 Swedens nobel prize winner Svante Arrhenius was the first to put hard figures on the greenhouse effect. He calculated at the time that doubling the CO_2 concentration would increase global temperatures by 5-6 degrees Celsius [7]. Subsequently he was the first scientist to predict the possibility of global warming due to human induced emissions of CO_2 (anthropogenic CO_2). While it must be noted that fluctuation in CO_2 levels and global temperature have always been a part of our planets past, a stable greenhouse atmosphere is extremely important to sustain life on earth as we know it. The calculations of Arrhenius show that the CO_2 emissions of the human population do certainly have an effect on the mean global temperature rise, which in turn can have consequences such as global sea level rise, changing weather patterns and extreme local cooling and warming. These effects will lead to a diminished availability of fresh drinking water and agricultural productivity [22].

Recent measurements have shown that the global concentration of CO_2 in the atmosphere has increased from around 277 ppm in 1750 to roughly 405 ppm in 2017, [11]. An increase of over 45 % is an extreme inflation compared with natural carbon cycles of the past millions of years and clearly an effect of human interference. The burning of fossil fuels and emission of CO_2 is a big contributor to the problem and should not exceed certain levels where it can impose irreversible climate change.

1.1.2. International Agreements and Mitigation of Anthropogenic Emissions

Since the effects of increasing CO_2 emissions has become more public knowledge at the end of the last century, numerous international agreements have been signed. The first treaty was signed by 165 countries in 1992, forming the United Nations Framework Convention on Climate Change (UNFCCC), and stated that the concentration of greenhouse gasses must be stabilized to prevent the triggering of major irreversible climate change [56]. Three years later in 1995 the participating parties of UNFCCC finalized the Kyoto Protocol in Japan where the first commitments were made to reduce the emissions of greenhouse gasses [1]. In 2010 the UNFCCC conference in Cancun, Mexico, quantified a maximum increase of global temperature at $2°C$ to avoid dangerous effects of climate change [56].

The most recent international agreement on climate change was signed in 2015 by 176 countries and is known as the Paris agreements. In these agreements the goals have been adjusted to keep global temperature increase well below $2°C$ and to pursue a limited increase of $1.5°C$ [55].

Since the Paris agreements, large steps and ambitious goals towards reducing greenhouse gasses have been constructed, however, there is still a long way to go. Many new technologies involving renewable energy, electric vehicles and energy storage have made substantial progress. Furthermore, many studies agree on the fact that to achieve emission reduction most efficiently, we need to combine different technological developments. These technological developments can range from renewable production of energy to technologies that retrieve CO_2 emissions from the atmosphere like carbon capture storage (CCS). Due to the fact that large industries will remain dependant on fossil fuels they are inevitably going to keep producing large amounts of CO_2 emissions in the foreseeable future, capturing and storage of these emissions will become a necessity. The IEA predicts that to reach the Paris agreement goal CCS will need to achieve an annual storage capacity of 4.9 Gt by 2060 [2].

1.2. Carbon Capture Storage

Carbon Capture storage (CCS) is now seen as an important new technology to reduce the emission of anthropogenic CO_2 emissions. The process of CCS consists of multiple steps including, capture, separation, transportation, intermittent storage and injection. In the first stage the flue gasses are captured from a point emission source (for example a power plant), which consists of a wide variety of components including CO_2. Before injection can be performed efficiently, the CO_2 gasses must be separated from the rest of the flue gasses. For separation, there are multiple methods available which are usually related to a certain capturing technique. Each capturing approach is combined with its related separation technique and produces a specific purity of CO_2 while consuming a certain amount of energy. What all techniques do have in common is that the amount of energy they consume is substantial. It is estimated that the costs of purification of the gas stream can reach to 75% of the total cost of CCS [9].

Since the purification processes of the gas stream is such an energy intensive process, it is of particular interest to analyse what the consequences are of impurities and the level of impurities when injecting and storing large amounts of CO_2 in the subsurface. In chapter 2 of this study, an extensive overview of the Carbon Capture and Sequestration processes are described.

1.3. Behaviour of injected CO_2 gas streams

In the process of storing large amounts of CO_2 in the subsurface, safety is the number one concern. During injection and storage in typical underground aquifers, the injected CO_2 is less dense and less viscous than the resident formation water, which causes it to be buoyant and mobile. Due to the buoyancy and mobility of the injected gas, the most pressing concern of underground storage is the risk of gas leakage to the surface via fractures or abandoned well boreholes. To determine the security of CO_2 storage, an accurate assessment of the gas plume migration and trapping of CO_2 after injection is critical.

To make an useful prediction on the gas plume migration and trapping of CO_2, the relevant physics must be implemented in simulation software. During the propagation of the gas plume, gas will be partially trapped by a variety of physical processes along the way, including residual trapping, dissolution and mineral trapping. A basic overview of the CO_2 trapping processes with related storage security can be found in figure 1.2. The residual trapping of small amounts of CO_2 occurs due to capillary imbibition and dissolution trapping occurs when CO_2 is dissolved into the brine solution. Trapping of CO_2 due to mineral precipitation or any other geochemical process will not be taken into account in this study.

Dissolution of CO_2 in the resident formation water will occur due to phase behaviour

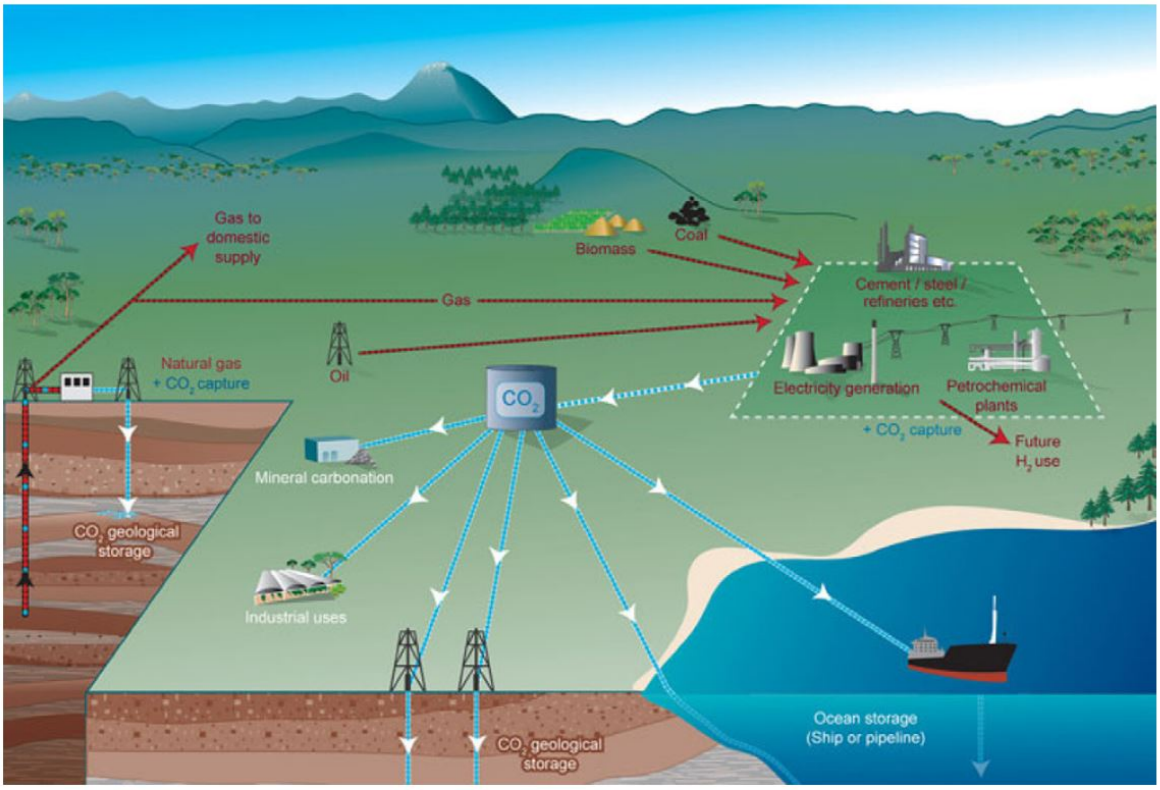
Gas to
domestic
supply
Biomass
Coal
Gas
Cement / steel /
refineries etc.
Oil
Natural gas
+ CO_2 capture
CO_2
Electricity generation
Petrochemical
plants
+ CO_2 capture
Future
H_2 use
Mineral carbonation
CO_2 geological
storage
Industrial uses
CO_2 geological
storage
Ocean storage
(Ship or pipeline)

Figure 1.1: A schematic overview of the CCS process chain [45]

(dependant on P, T, composition and salinity, which will be described by a thermodynamic model) and by diffusion. Dissolved CO_2 is considered to be trapped because it will no longer be buoyant, which means it will not rise and be able to leak to the surface [39]. As CO_2 dissolves in the resident brine solution, the density of the resulting aqueous solution will increase causing the boundary between the (mobile) gas plume and the brine formation water to become unstable. The denser aqueous solution will sink down in finger-like forms causing the brine solution to rise up. This process forms the basis of convective mixing that will occur and increase the overall dissolution rate of CO_2. Macminn and Juanes [40] and MacMinn et al. [39] have shown that dissolution and buoyant currents of CO_2 of the gas plume have an arresting effect of plume speed and therefore on plume migration.

Over the years more realistic large scale (long time) descriptions of CO_2 gas plume migration have been developed such as Class et al. [13] and Elenius et al. [18]. The study by Elenius et al. [18] is a very important paper because it contains the only converged benchmark study of a large scale CO_2 injection problem, considering simplified physics and pure CO_2 injection. In a more recent study Sin et al. [52] has attempted to make a more complex investigation of the CO_2 gas plume behaviour by including a cubic EoS to describe phase behaviour and by including chemical reactions (and thus mineral trapping of CO_2). Yet again another attempt to model CO_2 gas plume behaviour using a cubic PR EoS to describe phase behaviour and accounting for the presence of impurities was done by G. van Loenen et al. [23]. The limitation of the works of [52] and [23] is that the use of a cubic EoS is not accurate in the prediction of gas component behaviour with water or brine solution, as the component behaviour of water is not accurately solved for an cubic EoS.

In this research study, the injection of a CO_2 gas stream into a slightly inclined reservoir will be modeled. The dimensions and characteristics of the reservoir will be set identical to that of Elenius et al. [18] to allow for future comparison of the results. In this research, an accurate simulation of CO_2 gas plume behaviour will be achieved by implementing an accurate thermodynamic model, instead of using a general cubic EoS. Using correlations for phase densities and viscosity's dependant of pressure, temperature and composition, an accurate description of phase behaviour is obtained. The developed thermodynamic model and phase property correlations are implemented in Delft Advance Reserach Terra Simulator (DARTS) framework developed at TU Delft.

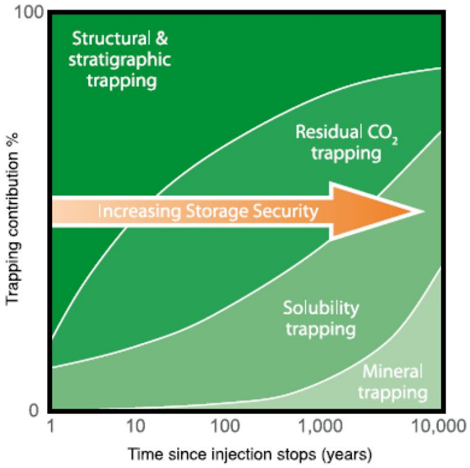

Figure 1.2: A basic overview of the various mechanisms for trapping CO_2 and the related security with time [27]

1.3.1. Thermodynamic Model

The phase behaviour of the different components in brine is crucial to understand the migration of the gas plume through the reservoir as well as understanding the effect impurities have on the CO_2 solubility [38]. To model and understand these processes, an accurate thermodynamic model must be implemented. The first works on thermodynamic modeling of hydrocarbon components (such as CO_2, CO) where done by Harvey and Prausnitz [26] 1989, Gao et al. [24] 1999 and Zuo et al. [61] 1991. However, these works were limited to low salinity, low temperatures and low pressures which are not representative to reservoir conditions.

The next step in gas solubility models was taken by Duan and co-workers who did extensive research on the solubility of single components (CO_2, CH_4, H_2S) in pure water or brine, see Duan and Sun [16] 2003, Mao and Duan [41] 2006, Duan et al. [15] 1992, Li and Duan [37] 2011, Mao et al. [43] 2013 for more details. The limitations of their work was that the models were not valid for implementation of gas mixtures.

In 2012 the modeling of CO_2, CH_4, H_2S gas mixture in brine was achieved by Ziabakhsh-Ganji and Kooi [58] and Zirrahi et al. [60] 2012. The results from their work were found to be consistent with existing experimental data for both single gas component solubility as that of a gas mixture. An important aspect which increases the accuracy of this model is that the thermodynamic equilibrium water is calculated separately using the approach of Spycher et al. [54].

The thermodynamic models that were developed for the solubility of individual gas components and gas mixtures differ in the thermodynamic properties used to determine the equilibrium conditions. These models can be divided into two groups, the fugacity-activity (F-A) models and the fugacity-fugacity (F-F) models [49]. For the F-A models the equilibrium condition of each component is described by fugacity coefficients for the gaseous phase (or non-aqueous phase) and by activity coefficients for the aqueous phase. Here the fugacity coefficients are determined by an EoS and the activity coefficients by an activity model. For F-F models both the gas phase and liquid phase of a component is described by the fugacity coefficient, which are both determined by an EoS.

For this research the F-A model was implemented to obtain the equilibrium conditions of each component in the gas mixture. The F-A model developed by Ziabakhsh-Ganji and Kooi [58] was taken as base structure to develop the thermodynamic model used in this research project. It is therefore important to note that the restriction of the thermodynamic model comes from the fact that the model is only valid for temperatures lower than 110°C and lower than 600 bar and lower than salinity of 6 molal NaCl.

1.3.2. Numerical Modeling

In this research, the injection and post-injection migration of the CO_2 gas plume will be modeled in an existing simulation framework Delft Advance Research Terra Simulator (DARTS). Modeling the injection of CO_2 and propagation of the CO_2 gas plume with consideration of all the complex physics involved requires a significant amount of simulation performance. To meet these performance demands, the newly proposed modeling technique called Operator Based Linearization (OBL) is used in DARTS.

1.4. Msc Thesis research project

This graduation research project is the final stage of the Master of Science program in Petroleum Engineering at the Delft Unversity of Technology and a demonstration that the author has reached the required academic level.

1.4.1. Motivation of this research

This research concerns the implementation of an accurate thermodynamic equilibrium model into an existing OBL transport model (DARTS) to describe the interaction of gas components with water or brine solutions at specific pressure, temperature and salinity conditions. Due to the present-day high profile problem of global warming, this model will be implemented to investigate the effects of gas impurities on the process of CO_2 sequestration. In particular, the effect impurities will have on the security of underground CO_2 storage, which is highly correlated with the propagation of the CO_2 gas plume. The less it propagates, the smaller the chance the plume will reach a fracture or other leakage point which leads to CO_2 escaping to the surface.

Additionally, a framework to investigate the total energy cost of the CO_2 sequestration process (CCS) is implemented into the model to get a basic understanding of how physics of injection effect the total process energy costs. Motivation for the implementation of this framework comes from the fact that high grade purification processes are extremely expensive.

In this research, a newly developed simulator DARTS, based on Operator Based Linearization approach, has been used to simulate the injection (and further migration) of gas into a saline reservoir. The use of this OBL modeling allows for combining of multiple complex physics in nonlinear solution of governing equations. By generating tables for all possible physics at a range of conditions, interpolation for properties at specific grid cells can be made which improves the performance of simulation.

1.4.2. Assignment description and Research question

This research aims to implement an accurate thermodynamic model in an Operator Based Linearization environment to obtain a better understanding of the role impurities have in secure storage of CO_2 in deep saline aquifers. Additionally, a framework is implemented to study and optimize the energy consumption related to the whole CCS process chain.

In trying to obtain knowledge on the subject the following research questions have been addressed:

- What type of impurities are commonly found in gas emissions after capturing and separation?
- How do impurities effect the solubility of CO_2 in the practical range of p, T and salinity?
- What are the effects of impurities on phase properties (density and viscosity) in the practical range of p, T and salinity?
- What effect impurities have on plume migration?

- How to obtain basic understanding of the total energy cost of CCS process?

1.4.3. Outline of the thesis

The start of this thesis report is initiated with a literary study (in chapter 2) which explores the various carbon dioxide capturing and separation technologies presently available with the resulting impurities of the produced gas stream. Here the answer to the first research question will be answered as the findings made in this chapter are used to define the inputs of the gas injection model. In Chapter 3, the physics related to the modeling of transport and phase behaviour will be explained extensively. Chapter 4 will present a detailed explanation of the implemented thermodynamic model. Chapter 5 addresses the calculation of the physical properties that are defined in our model, such as the phase viscosity, density and relative permeability. In chapter 6 a basic framework is presented to obtain a basic understanding of the power consumption of the whole CCS process chain. Chapter 7 will start by presenting validations of the implemented thermodynamic model and used phase property correlations. In these validations with literature the effect of CO_2 solubility in the practical range of p, T and salinity will be presented. Similarly, the effect of impurities on the phase properties will be shown in the validations of the properties with literature. After the validations, the results of the fully physical simulation results in large scale models will be presented. Here the effects of various physics and impurities have on plume behaviour will be analysed. The chapter will eventually end with the preliminary results obtained from the process power consumption framework.

2

Literature Study

2.1. Capture & Separation Processes

Carbon capture storage is a term which describes a range of processes which starts with capturing CO_2 at large point-emission sources and ends with the injection of a CO_2 gas stream into the subsurface. Before carbon dioxide can be injected into geological reservoirs it must have been captured, separated and transported to the injection location. These operations are complex and characterized by high energy and capital costs. Another important characteristic of the process is that the end product is never a 100% pure CO_2, impurities will always be present. Due to the fact that the whole purification process of CO_2 can take up to 75% of general cost [44], it is crucial to explore and understand the process of purifying CO_2. In this chapter a short description of the major capture and separation techniques will be given with their accompanying end product compositions.

2.1.1. Capture

The first step in the CO_2 sequestration process is the capturing of flue gasses from major fixed point CO_2 emitting sources, e.g. coal fired power plants, cement manufacturing facilities [45]. There are multiple methods for capturing emission gasses and they are divided into the following three groups.

- **Post-combustion Capture**

  A process which removes CO_2 from flue gas after combustion and is applicable on conventional facilities. A major challenge for this method is the large percentage of non-CO_2 gasses present with only 4-14% v/v of CO_2 concentration [3]. For the capturing of of CO_2 from the emission stream, solvents are usually used to absorb the CO_2 compounds. Since the typical flue gasses have low CO_2 concentrations and are just above atmospheric pressure, this results in low partial pressures which favours liquid solvents for the chemical absorption of CO_2. Disadvantages for this process is that large a volume of flue gas is needed (due to low concentration CO_2) and that powerful chemical solvents need to be used. Regeneration of the solvents to release the CO_2 requires a large amount of energy [3] which effects the efficiency of the process. .

- **Pre-combustion capture**

  The second method captures the CO_2 before fuel combustion. The process produces synthetic gas (syngas) from the fuel, after which the resulting CO_2 is captured and the H2 is used as carbon free fuel. In pre-combustion capture the fuel sources are treated before combustion with a gasification or partial oxidation process which produces the syngas. For example solid fuels such as coal or biomass are converted to syngas in an oxygen blown gasifier via partial oxidation [46]. Due to higher partial pressure of the resulting CO_2, it is possible to use physical solvents (selexol or rectisol) for the separation of CO_2. For this process the fuel must be pre-treated which will have a negative effect on the efficiency of a power plant.

The advantage of pre-combustion capture using syngas is that the chemical energy of carbon is transformed to the chemical energy of hydrogen with the added advantage over post-combustion capture of higher CO_2 concentrations and pressures achieved in the output stream [45]. Also hydrogen combustion does not produce any sulphur dioxide, which can have a substantial effect on the corrosion of installations and pipelines. A major disadvantage of pre-combustion capturing are the high investment costs [3].

- **Oxy-fuel combustion**

  In this last process pure oxygen is injected during the combustion process instead of air. The result of which is that the amount of nitrogen present in the exhaust gasses is strongly reduced, as well as substantial reduction of NO_x compounds. Due to the reduction in the formation of impurities high CO_2 concentrations in the range of 80-98% are produced. With these high concentrations of CO_2 the volume of gas to be treated is greatly reduced, which in turn will also lead to a substantial reduction in the separation costs. However, to obtain the pure oxygen needed for combustion a separator is needed which uses large amounts of energy. Also, due to combustion with pure oxygen the flame temperature will become excessively high, which will have to be reduced by recycling some of the CO_2 rich flue gas [3].

Of the three major CO_2 capturing methods, pre-combustion is mainly used for specifically coal gasification, while post-combustion and oxyfuel can be applied to both coal and gas plants. The pre-combustion process for coal is the most developed process and therefore currently has the lowest cost per ton of CO_2 [36]. Figure 2.1 shows an overview of the pro's and con's of carbon capture technologies.

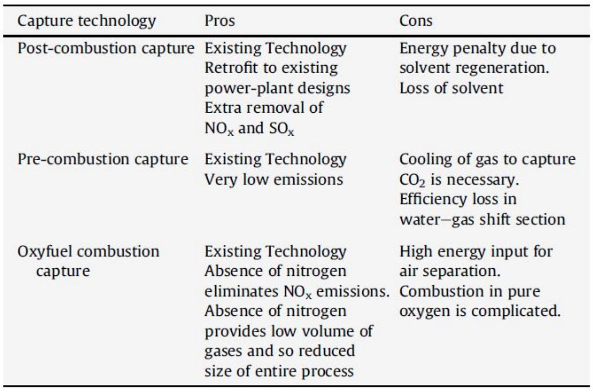

Capture technology	Pros	Cons
Post-combustion capture	Existing Technology Retrofit to existing power-plant designs Extra removal of NO_x and SO_x	Energy penalty due to solvent regeneration. Loss of solvent
Pre-combustion capture	Existing Technology Very low emissions	Cooling of gas to capture CO_2 is necessary. Efficiency loss in water–gas shift section
Oxyfuel combustion capture	Existing Technology Absence of nitrogen eliminates NO_x emissions. Absence of nitrogen provides low volume of gases and so reduced size of entire process	High energy input for air separation. Combustion in pure oxygen is complicated.

Figure 2.1: Pro's and con's of capture technologies [3]

2.1.2. Separation Techniques

Based on the three major capturing methods, separation techniques have been developed to further purify CO_2 in the gas stream. A wide range of separation techniques have been designed. However, not all of them are applicable for large scale operations such as power plants. The different techniques consist of absorption, adsorption [1], cryogenics and a variety of membrane separations.

Each of these techniques works most efficiently for a specific type of flue gas stream, which in turn depends on the point-emission source and capturing methods applied [44]. For example in the pre-combustion capture of a coal fired power plant the CO_2 concentration in the emission stream would be roughly 35-40% at a pressure that can exceed 20 bar. For these conditions an application of selexol, a physical solvent, would be a good separation technique because CO_2 can be released mainly by depressurization by which the high heat consumption of amine-scrubbing processes are avoided. A short description of the different separation techniques available can be found below.

---

[1] Absorption is the process in which a fluid is dissolved by a liquid or a solid (absorbent). Adsorption is the process in which atoms, ions or molecules from a substance (it could be gas, liquid or dissolved solid) adhere to a surface of the adsorbent. Adsorption is a surface-based process where a film of adsorbent is created on the surface while absorption involves the entire volume of the absorbing substance, `https://www.diffen.com/difference/Absorption_vs_Adsorption`.

- **Absorption** *(most mature method, using liquids)*

  Absorption processes can be divided into chemical and physical absorption. In chemical absorption the acid CO_2 gas is removed (absorbed) from the gas stream due to an acid-base neutralization reaction. The solvent chemically reacts with the CO_2 compound to form a weak intermediate compound which in time can be broken down releasing the CO_2 with the introduction of heat [44]. Typical liquid solvents are monoethanolamine (MEA), diethanolamine (DEA) and potassium carbonate.

  MEA is found to be the most efficient for CO_2 absorption with upwards of 90% efficiency, which is highly dependant on the CO_2 concentration of the gas stream [36]. After the solvents have absorbed the CO_2, it can be regenerated by heating and/or depressurization, for which a significant amount of heat is needed. The degradation of the amine solvent stills proves to be a major challenge which can lead to solvent loss, equipment corrosion and the generation of volatile degradation compounds. Some of the amine emissions can potentially degrade into nitro- and nitra-amines which are potentially harmful for the environment and human health [36]. Environmental impact of absorbents still have to be better understood.

  Physical absorption of CO_2 by solvents works by introducing the solvent and the gas to a certain state (pressure and temperature) whereby the gas components will dissolve in the solvent [44]. This process works according to Henry's law where the solubility of a component depends on the partial pressure and the temperature, where higher partial pressures and lower temperatures will increase the solubility of the CO_2 compound in the solvent. These solvents can eventually be regenerated by heat introduction or pressure reduction. The most used physical solvent are selexol and rectisol which have been in use commercially for decades to separate CO_2 from natural gasses.

- **Adsorption** *(using solids)*

  Unlike absorption where the CO_2 compound is bound to a solvent in a liquid phase, adsorption is the process of a gas compound attaching itself to the surface of a solid material. For a compound in the gas phase to attach itself to a solid surface (or adsorbent) relies strongly on the thermodynamic properties of the substance and can be achieved physically or chemically [44]. Typical adsorbents are; molecular sieves, activated carbon, zeolites, calcium oxides, hydrotalcites and lithium zirconate. The properties of the adsorbed particles and the adsorbent surface determine the quality of adsorption [45]. By changes in pressure (pressure-swing adsorption) and temperature (temperature-swing adsorption) CO_2 is attached and released from the adsorbent making the adsorbents reusable. Absorbent efficiency of >85% achievable, however this also requires high energy cost [36].

  The main disadvantage for using adsorption processes in post-combustion CO_2 separation is the need of cooling and drying the flue gas which requires a substantial amount of energy which makes the process very inefficient [45].

- **Chemical looping combustion**

  Chemical looping combustion is a process where combustion of the carbon fuel is driven by oxidation and reduction reactions using metal-oxides as oxygen carriers [44]. It is a process similar to oxyfuel combustion only where metal oxides are used as delivery unit of oxygen [36]. The advantage of this process (as with oxyfuel combustion) is that CO_2 is the main combustion product with a very high purity level (not mixed with N_2) which makes additional separation processes abundant. Also, there will be no thermal formation of NO_x since regeneration of the oxygen carrier takes place without flame and at moderate temperatures [3]. This is a very promising technology but is has not been tested yet on a large scale.

- **Membrane separation**

  Another new promising separation technology is the use of membranes to selectively separate gas compounds from an injection stream. This is a technology which is very versatile, meaning that it can be implemented in most combustion systems. For example membranes are able to separate CO_2 compounds from flue gas streams in post combustion systems, CO_2 from hydrogen from pre-combustion systems and oxygen from nitrogen in a oxyfuel combustion system [44]. Membranes are used to separate the flue gases by allowing only CO_2 to pass through while excluding other components. CO_2 separation achieved from membrane separation is around 82-88%, but is highly dependent on the concentration of the CO_2 in flue gas [36]. It is a promising technology but still in development.

- **Cryogenic distillation**

  Cryogenic distillation is also known as separation by condensation where gas mixtures undergo fractional condensation and distillation at low temperatures.The gas mixture will be cooled so that the CO_2 compounds will liquefy and separate [44]. A major advantage of this process is that the end product of purified CO_2 is already in liquefied form which is convenient for transportation to the injection location. Efficiencies can be reached of around 90-95% [36].Another advantage of this process is that it eliminates water consumption, usage of chemicals and corrosion related issues [45].

2.2. Impurities from different Carbon Capture streams

In the process of carbon dioxide capture and separation a large range of impurities will be formed from various product streams. The impurities present in the gas streams can have a large impact on the storage, compression and economic transportation wherefore it is crucial to keep the concentrations of impurities as low as possible. In this chapter the types and concentration of impurities will be described per capturing method. To limit the scope of this research, the impurities of coal fired power plants is considered.

2.2.1. Classes of impurities

Impurities in CO_2 streams can be broadly classified into three main categories: (1) fuel oxidation, (2) excess oxidant ingress (e.g. inerts) and (3) process fluids. In figure 2.1 an overview of all impurities found in coal/biomass oxidation is given. This type of carbon fuel produces a larger range and higher level of impurities in comparison with natural gas combustion.

Complete oxidation of coal or biomass forms the most common impurity products such as H_2O, SO_x, NO_x and halogens (Br, F, Cl, I, At). Partial oxidation impurities are primarily carbon monoxide (CO) and hydrogen sulfide (H_2S), which are mostly the result of fuel rich conditions such as in the production of syngas by gasifiers. Volatile mixture consist of hydrogen and light hydrocarbons which are formed due to heating of the fuel before combustion. Trace metals contained in the fuel may also be released to the gas phase during combustion and can propagate into the emission stream. These metals can be present in elemental or oxidized form. Oxygen, nitrogen and argon are the result of excess oxidants used for combustion or air ingress into the boiler. The final class of CO_2 impurities are the process fluids (solvents) used to separate CO_2, such as menoethanolamine (MEA) and selexol [46].

2.2.2. Post-Combustion Capture impurities

In the post-combustion capturing process, raw flue gas is fed into a separator unit that uses different types of solvents or absorbents to extract the CO_2 compounds from the gas mixture. For the post-combustion flue gasses absorption by solvents like amine and MEA are most effective and will be the only solvents considered here. Table 2.1 gives a detailed overview of the range and levels of impurities from post-combustion capture from different authors. The data used is taken from a range of sources which can be found in Richard T.J. Porter [46].

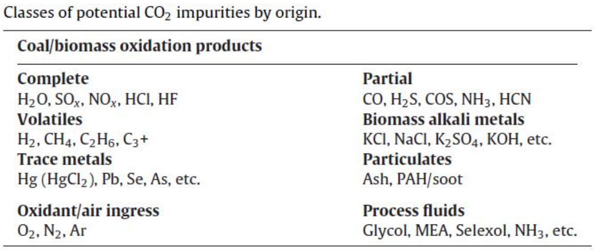

Classes of potential CO_2 impurities by origin.

Coal/biomass oxidation products	
Complete	**Partial**
H_2O, SO_x, NO_x, HCl, HF	CO, H_2S, COS, NH_3, HCN
Volatiles	**Biomass alkali metals**
H_2, CH_4, C_2H_6, C_3+	KCl, NaCl, K_2SO_4, KOH, etc.
Trace metals	**Particulates**
Hg ($HgCl_2$), Pb, Se, As, etc.	Ash, PAH/soot
Oxidant/air ingress	**Process fluids**
O_2, N_2, Ar	Glycol, MEA, Selexol, NH_3, etc.

Figure 2.2: Classes of potential CO_2 impurities by origin, [46]

Important findings of post-combustion capture are that CO_2 purity is very high at 99.6-99.8% v/v of CO_2. The most present impurity found is N_2 which can arise from excess air in the boiler, air ingress into the process or from NO_x conversion. The second most present impurity found is H_2O, which will predominantly arise from the post-combustion solvent which can contain around 30% amine in aqueous solution. A small amount of fuel oxidation products and trace metals can also be found but are negligible.

Component	unit	Amine PC plant	MEA PC plant
CO_2	% v/v	99.8	99.7
N_2	% v/v	0.045	0.18
Ar	ppmv	-	22
H_2O	ppmv	100	640
NO_x	ppmv	20	1.5
SO_x	ppmv	10	<1
CO	ppmv	10	-
O_2	ppmv	150	61
Ash	ppmv	-	11.5

Table 2.1: Classes of potential CO_2 impurities for Amine and MEA separation of Post-Combustion capture [46]

2.2.3. Pre-combustion (IGCC) Capture Impurities

Pre-combustion process captures CO_2 before combustion by producing syngas of the carbon fuel via partial oxidation. In coal fired power plants this process is defined as an Integrated Coal Gassification Combined Cycle (IGCC). In a IGCC the syngas produced mainly consists of a mixture of CO, H_2, CO_2 and H_2O. Here partial oxidation products are produced in significant quantities due to the incomplete oxidation that occurs during syngas formation, which is different to post-combustion and oxy-fuel capture where complete oxidization occurs.

A water-gas shift reactor is used to let the partial oxidation product CO react with water to produce CO_2 and H_2. The next step in the purification process is the removal of sulfur in the partially oxidized form of H_2S using solvents. Since selexol and rectisol are mostly used and most effective, these will be the only solvents considered here. After CO_2 removal the syngas stream is rich in H_2 which can be used to produce energy [46].

The quality of the resulting CO_2 stream is highly influenced by the quality of the fuel which is used for combustion. Particularly, the levels of sulfur in solid fuels will dictate the levels of gas-phase sulfur species in the syngas produced by the gasifier. The efficiency of CO_2 removal will also have an effect on the resulting product stream. The efficiency can be influenced by process temperatures, residence times, loading rates and solvent selection (such as selexol).

Table 2.2 gives detailed ranges and levels of impurities from pre-combustion capture form different authors and with different methods of separation [46]. This data is specifically given for pulverized coal combustion. Here H_2 is the most voluminous impurity found. N_2 is also a significant impurity resulting from impure oxidant or air ingress. Ar and H_2O make up impurities at lower levels.

Component	unit	Selexol	Rectisol
CO_2	% v/v	98.1	95-98.5
N_2	% v/v	0.0195	<1
H_2	% v/v	1.5	0.002
Ar	ppmv	178	150
H_2O	ppmv	378	0.1-10
H_2S	ppmv	1700	0.2-20
CH_4	ppmv	112	100
CO	ppmv	1300	400
CH_3OH	ppmv	-	20-200
Ash	ppmv	1.2	-
NH_3	ppmv	38	-
Cl	ppmv	17.5	-

Table 2.2: Impurities resulting from selexol and rectisol separations in pre-combustion of pulverised coal, [46]

2.2.4. Oxy-fuel Combustion and Capture Impurities

The current process for purification of oxyfuel combustion consist of two stages: (1) raw flue gas cooling and compression to processing conditions and (2) low temperature purification. In the first stage, the raw flue gasses from oxy-fuel combustion are brought to pre-purification conditions at 35°C and 1 bar. The second stage consists of a low temperature purifaction process where oxygen, nitrogen and argon are removed from the flue gasses. The resulting product gas streams of both stages can be found in table 2.3.

Component	unit	**stage 1** - Raw flue gas at 35°C & 1.02 bar	**stage 2** - CO_2 product at 35°C & 110 bar
CO_2	mol %	71.5	95.8
N_2	mol %	14.3	2.0
O_2	mol %	5.9	1.1
Ar	mol %	2.3	0.6
SO_2	mol %	0.4	0.5
NO	mol %	0.04	0.01
H_2O	mol %	5.6	0.0

Table 2.3: Impurities resulting from oxy-fuel combustion, [6]

One of the parameter which has a large effect on the CO_2 purity is the ASU (air separation unit), which supplies the oxygen for combustion. The ASU typically provides oxygen in 95-99% v/v purity range, which will impact the N_2 and Ar concentration in the raw CO_2 flue gas stream. Higher O_2 purity requires more power for the ASU and more costs. Solid fuel properties that effect the CO_2 purity are high sulfur coals leading to higher levels of SO_x.

Eventually, after the purification stages, a high CO_2 purity is reached of around 96%, with nitrogen and oxygen as the main impure components.

2.3. Summary and relation to further chapters

In this chapter, an in-depth investigation was performed on the capture and separation techniques and their related emission streams. The focus of this chapter was but put on coal fired powerplants to limit the scope of the research. From the investigation performed it can be concluded that the three main capturing and separation techniques (post-combustion MEA solvent separation, pre-combustion IGCC, and oxy-fuel combustion) all produce relatively highly purified CO_2 gas streams (>0.96 %). The main impurity components found differ per separation technique, however, the most common impurities overall were found to be N_2,

CH_4, Ar, H_2, CH_4, H_2S and SO_2. The significance of these findings in relation to the following chapters is that the discovered impurities will be used used as inputs in the thermodynamic model. Eventually, only three impurity components were chosen to limit the scope of the thesis which were: N_2, CH_4 and H_2S.

3

Physics

In this chapter, first an extensive description of the physical process involved in injection and post-injection migration of a gas plume are described. A description of how these physical processes are implemented into the model with accompanying assumptions is presented hereafter. Section 3.3 will give the governing equations describing these physical processes. The chapter will then be concluded by the an explanation of the numerical implementation of the governing equations into the Delft Advanced Research Terra Simulator (DARTS).

3.1. Physics of CO_2 injection and post-injection processes

In the process of CO_2 injection and storage in the subsurface formations, there are several physical phenomena that we need to consider. The first important physical process is related to the fact that the injected CO_2 stream is less dense and less viscous than the resident formation brine which causes the injected gas to become buoyant. As a result, the gas plume will migrate to the top of formation and gas plume will be able to migrate significant distances over time.

The second important phenomenon is the residual trapping of CO_2 stream during the migration through the saline aquifer. In addition, at longer timescale, dissolution and mineral trapping starts playing important role. Usually, mineral trapping of CO_2 or any other chemical reactions become significant at very long timescales (several tens thousands of years) and therefore will not be taken into account in this study. The residual trapping of small amounts of gas components occurs due to capillary imbibition and dissolution trapping occurs when gas components are dissolved into the brine solution. Dissolved CO_2 is considered to be trapped because it will no longer be buoyant, which means it will not be able to leak to the surface [39]. Gas components will dissolve into the resident brine due to component phase partitioning at specific (pressure & temperature) conditions and due to diffusion.

The combination of miscible gas and a buoyant gas plume convection is very important phenomenon. As CO_2 dissolves in the resident brine solution, the density of the resulting aqueous solution will increase causing the boundary between the (mobile) gas plume and the brine formation water to become unstable. The denser aqueous solution will start sinking down in finger-like forms, causing the brine solution to rise up. This process forms the basis of convective mixing that will occur which will enhance the dissolution rate of CO_2.

3.2. Model Description

The objective of this model is to simulate the transport and phase behaviour of gas mixtures at injection and post-injection stage. In this model only two phases are considered, the gaseous (super-critical) phase and the aqueous phase. The injection and post-injection gas dynamics are modeled in an inclined reservoir which has the same dimensions as the reservoir used in Elenius et al. [18] study. An extensive description of the reservoir dimensions and properties will be given chapter 7, section 7.2.

To model the physics of the gas plume behaviour during injection and post-injection stage, it is imperative to predict accurate phase behaviour. In the compositional transport model developed in this research, an accurate thermodynamic model will be implemented to solve the phase equilibrium and to determine component phase partitioning. Using the obtained component phase partitioning the phase properties (density and viscosity) will be determined. Note that due to lack of an accurate gas viscosity correlation a constant value was used similar to the one used in Elenius et al. [18].

In this model the injection of super-critical gas is treated as a gas phase. Salt is assumed to have a uniform concentration throughout the reservoir and remains constant during simulation. The presence of individual salt components is not taken into account when solving the thermodynamic phase behaviour. The formation of a separate solid phase is neglected which means that the effect of salt precipitation on the permeability will not be taken into account. Note that chemical reactions are not included in the model.

The simulation of injection of a gas mixture with up to four components will require significant performance of the simulator. In addition to the nonlinear iterations which need to be performed through solution, the thermodynamic equilibrium needs to be solved in every grid block at each nonlinear iteration. To meet the performance demand required for this type of simulation, a recently-proposed Operator Based Linearization (OBL) technique is implemented to solve the nonlinear problems. An extensive description of the OBL method and its implementation will be given in the last section of this chapter.

3.2.1. Components and Phases

During the injection of flue gasses from capturing and separation processes, a large variety of components will be present. In this study, a maximum of 4 component composition of the gas stream is considered. The employed gas components are CO_2, N_2, CH_4, H_2S and H_2O. As mentioned earlier sodium chloride salinity is also taken into account, however, the changes in NaCl composition are not considered.

The mass components in this system are present only in two possible phases j: the aqueous phase Aq and the non-aqueous or vapour phase V. The partitioning of gas components in each phase will be determined by the thermodynamic model, which in turn can be used to calculate the properties of each phase. The formation of two-phase regions are possible.

3.2.2. Modelling processes and assumptions

For the modeling of gas stream injection, several processes need to be considered and multiple assumptions and simplifications should be introduced. In the model the following physical processes will be simulated:

1. convective flow of mass through formation,
2. phase behaviour resulting from component equilibrium phase partitioning, and
3. transport of soluble gas components over time due to diffusion.

The assumptions applied to simplify some of the modeled processes are:

1. Darcy's law,
2. instantaneous thermodynamic equilibrium,
3. iso-thermal conditions throughout reservoir,
4. salinity of brine stays constant over time and space,
5. slight compressibility of reservoir rock, and
6. chemical reactions are neglected.

3.3. Governing equations

For any description of flow in porous media, the conservation of mass must be solved to describe the amount of components present at any location in the reservoir. For a gas injection system, the most important physical flow mechanisms are convection, diffusion and dispersion. For simplicity, the dispersion processes are assumed to be compensated by numerical dispersion which results in a simplified continuity equation for isothermal, multi-phase flow. In addition to mass transport, the composition of each phase and its corresponding physical properties (density and viscosity) need to be determined using a multiphase flash procedure and empirical formulations respectively.

3.3.1. Mass balance equation

In vector form the mass balance equation of the system with n_p phases (aqueous and vapor) and n_i components can be written as

$$\frac{\partial m_{ij}}{\partial t} + \nabla l_{ij} + q_{ij} = 0, \tag{3.1}$$

where m_{ij} is the total mass present of component i in phase j, l_{ij} is the total flux of component i in phase j and q_i is the source or sink term. They defined as

$$m_{ij} = \phi \rho_j s_j x_{jj}, \tag{3.2a}$$

$$l_{ij} = \rho_j x_{jj} u_j + j_{ij}, \tag{3.2b}$$

$$q_{jj} = \rho_j x_{jj} q_j. \tag{3.2c}$$

Substituting these parameters into the vector form governing equation we obtain:

$$\frac{\partial}{\partial t}\Big(\phi \sum_{j=1}^{n_p} x_{ij}\rho_j s_j\Big) + \frac{\partial}{\partial x}\Big(\sum_{j=1}^{n_p}(x_{ij}\rho_j \mathbf{u}_j + s_j\rho_j \mathbf{J}_{ij})\Big) + \sum_{j=1}^{n_p} x_{ij}\rho_j q_j = 0, \quad i = 1,..,N_c. \tag{3.3}$$

Here $\mathbf{u}_j$ is the Darcy velocity which is proportional to the pressure gradient and is defined as

$$\mathbf{u}_j = -\frac{K k_{rj}}{\mu_j}(\nabla P_j - \rho_j g). \tag{3.4}$$

Here $\mathbf{j}_{ij}$ is the diffusion-dispersion tensor of component i in phase j, which is described by

$$\mathbf{J}_{ij} = -\phi D_{ij} \nabla x_{ij}. \tag{3.5}$$

Here K is the permeability, k_{rj} is the relative permeability of phase j, μ_j is the viscosity of phase j, ∇P_j is the pressure gradient over phase j and g is the vector of gravitational acceleration. The saturation of phase j, the volume fraction the phase occupies, is given by the following relation:

$$s_j = \frac{v_j/\rho_j}{\sum_{j=1}^{np} v_j/\rho_j}, \tag{3.6}$$

where v_j is the molar fraction of phase j.

3.3.2. Thermodynamic relations

For the simulation of flow and transport in porous media, an accurate input of physical properties of each phase is required in the system with a mass balance equation. To obtain these physical properties, the composition of each phase needs to be determined and therefore an exact thermodynamic equilibrium is necessary. Assuming local instantaneous thermodynamic equilibrium, the phase behaviour calculations are only dependant on pressure and molar composition of the mixture. The phase behaviour calculations are therefore decoupled from flow and transport due to the instantaneous equilibrium assumption. The definition of the thermodynamic equilibrium states that the chemical potentials of the component in both phases are equal:

$$f_{Li}(p, T, \mathbf{x}) = f_{Vi}(p, T, \mathbf{y}), \tag{3.7}$$

where **x** and **y** are phase composition in liquid and vapor phases respectively.

There are multiple methods to solve the thermodynamic phase behaviour such as the EoS based methods and methods using constant K-values. In this research, two EoS based methods will be used: one based on conventional cubic EoS and another using a Fugacity-Activity based method. An extended explanation on thermodynamic models in study will be given in Chapter 4.

3.3.3. Closing relations

For the completeness of the model a set of closing relations must be applied:

$$z_i - \sum_{j=1}^{n_p} x_{ij} v_j = 0, \quad i = 1, .., n_c, \tag{3.8}$$

$$\sum_{i=1}^{n_c} z_i - 1 = 0. \tag{3.9}$$

Here, equations 3.8 and 3.9 represents the overall composition and the composition constraint of components in the system, respectively. In addition, two more constraints should be added regarding the phase constraints as:

$$\sum_{i=1}^{n_c} (x_{i1} - x_{ij}) = 0, \quad j = 2, .., n_p, \tag{3.10}$$

$$\sum_{j=1}^{n_p} v_j - 1 = 0, \quad j = 1, ..., n_p. \tag{3.11}$$

Here v_j is volume fraction of phase j and calculated by:

$$v_j = \frac{\rho_j S_j}{\sum \rho_k S_k}, \tag{3.12}$$

where S_k is saturation of phase k.

3.4. Delft Advance Research Terra Simulator (DARTS)

The governing properties and corresponding flash calculation were implemented in DARTS. A short description of this framework is presented below.

3.4.1. Nonlinear Formulation

Governing equations 3.3 depends on pressure, temperature, salinity and overall composition of present components. For a system of n_c components, the equations needs to be solved for n_c nonlinear variables, given in a value vector as: $\{p, z_1, ..., z_{n_c - 1}\}$. Here we assume that temperature and salinity remain constant.

To solve this system, the governing equations are discretized over space and time using the finite volume method. The application of a finite-volume discretization in space and backward Euler approximation in time generates the following form of the governing equation:

$$V\Big[\Big(\phi \sum_{j}^{n_p} x_{ij} \rho_j s_j\Big)^{n+1} - \Big(\phi \sum_{j}^{n_p} x_{ij} \rho_j s_j\Big)^{n}\Big] - \Delta t \sum_{l} \Big(\sum_{j}^{n_p} x_{ij}^l \rho_j^l T_j^l \Delta \Psi^l + \rho_j s_j J_{ij}^l\Big) + V \Delta t \sum_{j}^{n_p} x_{ij} \rho_j q_j = 0. \tag{3.13}$$

Here Ψ^l represents the pressure difference between two grid blocks, T_j^l is the transmissibility of phase j and is defined as: $T_j^l = k_{r,j}^l/\mu_j^l$. V is the total control volume of a grid block and superscript l represents the interface which connects the control volume with other grid blocks.

The backward Euler approximation in time introduces strong nonlinearity to the system of governing equations. To solve the nonlinear governing equation, the problem needs to be linearized. The linearization of the problem requires the determination of all the partial derivatives with respect to nonlinear unknowns and assembly of the Jocabian and residuals. For every nonlinear iteration, the following linear system of equation is solved:

$$J(\omega^k)(\omega^{k+1} - \omega^k) = -r(\omega^k), \tag{3.14}$$

where $J(\omega^k)$ and $r(\omega^k)$ are the Jacobian and residual defined at the nonlinear iteration k [33].

3.4.2. Operator Based Linearization

The simulation of CO2 sequestration processes is based on solution of strongly nonlinear governing equations which describe conservation of mass and energy (in isothermal assumptions only mass). The Operator Based Linearisation (OBL) technique solves this problem using a multi-linear representation of combined coefficients (operators) in governing equations.

In the OBL approach, each term of the discretized conservation equation is represented by a product of two operators: (i) state- and (ii) space-dependant. The state-dependant operators describe the part of the conservation equations which is dependant on rock- and fluid physical properties. The space dependant operator represents the spatially altered part of the properties. The state-dependant operators are parameterized over the physical space of the simulation problem. In the course of simulation, the state-dependant operators are calculated based on a multilinear interpolation in a multidimensional space of nonlinear parameters. The space-dependant operators are calculated in a conventional manner [33].

The state-dependent operator values are linearly interpolated on the mesh with a predefined accuracy. The values of the state dependant operators are calculated adaptively using conventional property estimators based on various correlations and the solution of EoS K. Kala and D. Voskov [32]. This way, the OBL technique improves simulation time by skipping routine evaluation of computationally expensive phase behaviour calculations performed in the course of simulation.

Below, we define all governing properties involved in the governing equations:

- State based properties (fluid and rock interactions): [32]
  - $k_{rw}(\omega)$ - relative perm,
  - $\rho_j(\omega)$ - density in $[mol/m3]$,
  - $S_j(\omega)$ - saturation,
  - $x_{ij}(\omega)$ - mole-fraction of component i in phase j,
  - $\mu_j(\omega)$ - phase viscosity.
- Space based properties (altered in space / reservoir structure and heterogeneity):
  - $K(\xi)$ - permeability tensor,
  - $\phi(\omega,\xi)$ - porosity,
  - $u_j(\xi)$ - phase velocity.

Applying the state and space based operators, the conservation equation can be rewritten as:

$$a(\xi)\big(\alpha_i(\omega) - \alpha_i(\omega_n)\big) + \sum_l \big(b(\xi,\omega)\beta_i(\omega) + c_i(\xi,\omega)\gamma_i(\omega)\big) + \theta_i(\xi,\omega,u) = 0, \tag{3.15}$$

where

$$a(\xi) = \Phi_0(\xi)V(\xi), \tag{3.16a}$$

$$\alpha_i(\omega) = \left(1 + c_r(p - p_{ref})\right) \sum_{j=1}^{n_p} x_{ij}\rho_j S_j, \tag{3.16b}$$

$$b(\xi, \omega) = \delta t \Gamma^l(\xi)(p - p^l), \tag{3.16c}$$

$$\beta_i(\omega) = \sum_{j=1}^{n_p} x_{ij}^l \rho_j^l \frac{k_{rj}^l}{\mu_j^l}, \tag{3.16d}$$

$$c(\xi) = \triangle t V(\xi), \tag{3.16e}$$

$$\gamma_i(\omega) = -\phi \rho_j S_j D_{ij} \nabla x_{ij}, \tag{3.16f}$$

$$\theta_i(\xi, \omega, u) = \Delta t \sum_{j=1}^{n_p} x_{ij}\rho_j q_j(\xi, \omega, u). \tag{3.16g}$$

Here

- α_i is the accumulation operator,
- β_i is the flux operator,
- θ_i is the source/sink operator,
- γ is the diffusion operator.

4

Thermodynamic Model

To determine how each phase flows in a reservoir, the phase properties must be defined. However, to determine the phase properties, the composition of each phase must be known. In this chapter, the determination of phase composition is described with using phase equilibrium assumptions.

As we have assumed local chemical equilibrium, the compositions of the phases are determined by the pressure, temperature, salinity and molar composition of the fluid present. A relationship between pressure, temperature and composition can be specified by an equation of state (EoS), which in turn can be used to calculate the composition of the equilibrium phases by performing flash calculation. Solving the thermodynamic equilibrium gives the partitioning of species in each phase using a flash calculation procedure. There are multiple flash procedures that will output the component composition x_{ij} and molar fraction v_j, however, in this research, the negative flash procedure will be used [57].

There are two approaches to represent the thermodynamic phase behaviour such as the EoS-based and constant K-values [21]. In this research, a fugacity-activity EoS-based method will be used, as this provides a more accurate determination of the aqueous phase behaviour.

4.1. Phase Partitioning - Negative Flash

Solving the thermodynamic equilibrium commonly consists of two stages: the phase stability test followed by flash calculation. Iranshahr et al. [29] developed a generalized negative-flash strategy based on compositional space parametrization to solve the phase partitioning at thermodynamic equilibrium where no phase-stability test is required.

The material balance of mixture described by the overall mole fraction z_i is given as follows:

$$z_i = y_i V + x_i(1 - V), \tag{4.1}$$

where V is the fraction of vapour or gaseous phase, x is the mole fraction of component i in the liquid (aqueous) phase and y is the mole fraction of component i in the vapour phase.

To solve component partitioning at phase equilibrium the flash calculation must be performed which is an iterative process of solving the Rachford-Rice equation

$$g(L_j) = \sum_{i=1}^{n_c} \frac{z_i(K_i - 1)}{1 + L_1(K_i - 1)} = 0. \tag{4.2}$$

In the EoS-based approach, this iteration process is a part of global Successive Substitution Iteration (SSI).

The Rachford Rice (RR) equation (equation 4.2) can also be solved for the phase volume fraction (L_1) when only 1 phase forms, this is called the negative flash. This method is more mathematically abstract as the molar fraction of a phase can become negative. A single phase mixture can also be seen as a linear combination of the phase compositions. What this means is that the single-phase composition must lie on the extension of the line that connects the equilibrium compositions on a phase diagram [21]. Whitson and Michelsen [57] showed that the negative flash calculation will converge as long as L_1 lies on in the range of:

$$\frac{1}{1-K_{max}} < L_1 < \frac{1}{1-K_{min}}. \tag{4.3}$$

The value for the phase volume fraction (L_1) is calculated iteratively using the RR until it converges. After obtaining the phase volume fraction, the phase compositions can be found using equations 4.4 and 4.5 and will be equilibrium compositions that can be combined to make the single-phase mixture [21]:

$$x_i = \frac{z_i}{1+L_1(K_i-1)}, \tag{4.4}$$

and

$$y_i = \frac{K_i z_i}{1+L_1(K_i-1)}. \tag{4.5}$$

4.2. Solving Thermodynamic phase Equilibrium

To understand the thermodynamic behaviour of phases, it is essential to understand how the thermodynamic equilibrium behaves. For a system to be in thermodynamic equilibrium, the chemical potential of the component in both phases are equal. This definition is shown in equation 4.6 where the chemical potential is expressed in terms of fugacity

$$f_{Li} = f_{Vi}. \tag{4.6}$$

The fugacity is a measure of the chemical potential in the form of an adjusted or partial pressure, which is used to show the deviation from ideal behaviour. In other words, the fugacity is the pressure correction an ideal gas would need to have to equal the chemical potential of a real gas at a certain temperature. For an ideal gas, the fugacity is equal to the pressure. The fugacity of a substance is related directly to the phase preference of a substance. When two different phases with different chemical potentials are mixed, the composition of two phases will be changing until the fugacities in both phases are equal. Only when the fugacities or chemical potential of both phases is equal, the system will obtain thermodynamic equilibrium.

Using EoS based approach, the thermodynamic behaviour of a system is solved for the equilibrium constant K_i of each component i. The equilibrium constant is in turn needed to solve the RR equation for molar fractions of the liquid (x_i) and vapour (y_i) phase. The phase equilibrium constant is given by the molar fraction of vapour phase y over the molar fraction of the aqueous phase x, as shown in equation 4.7

$$K_i = \frac{y_i}{x_i}. \tag{4.7}$$

How this equilibrium constant is derived differs with the EoS method used.

4.2.1. Conventional Fugacity-Fugacity Models

Solving the thermodynamic phase behaviour with the conventional EoS-based method consists of deriving the fugacity for each component in each phase. This is an iterative procedure where the solution of the new phase equilibrium constant is found when it converges below a certain value.

Obtaining the fugacity for each component in each phase starts with solving the RR equation to obtain the phase partitioning of the species. The measure of how each component is distributed in each phase (x_i and y_i) are necessary inputs to solve the Equation of State for the molar volume of each phase. Which EoS is used can differ with the conditions present in a specific system. In this research, the Peng-Robinson (PR) EoS is used due to its high reliability for gas mixtures close to critical conditions. The PR EoS is given by equation 4.8

$$P = \frac{RT}{V - b_{mj}} - \frac{(a\alpha)_{mj}}{V^2 + 2b_{mj}V - b_{mj}^2}. \tag{4.8}$$

Having obtained the molar volume of each phase the fugacity of each component can be calculated using equation 4.9

$$\ln \frac{\hat{f}_{ij}}{x_{ij}P} = \frac{b_i}{b_m}(z-1) - \ln\Big(z\{1 - \frac{b_m}{V}\}\Big) + \Big(\frac{a_m}{2\sqrt{2}b_m RT}\Big)\Big(\frac{b_i}{b_m} - \frac{2}{a_m}\sum_{k=1}^{n_c} x_{kj}(a\alpha)_{ik}\Big) \times ln\Bigg(\frac{1 + (\sqrt{2}+1)\frac{b_m}{V}}{1 - (\sqrt{2}-1)\frac{b_m}{V}}\Bigg). \tag{4.9}$$

When the fugacity of each component is obtained, the new phase equilibrium constant K_i of each component i is derived as shown in equation 4.10. As long as the difference between the new and old k-value is not smaller than the convergence criterion ϵ the process will repeat itself (with the new k-value as input for the RR equation)

$$K_i^{k+1} = K_i^k \frac{\hat{f}_{i2}^k}{\hat{f}_{i1}^k}. \tag{4.10}$$

4.2.2. Fugacity-Activity Model

Solving the thermodynamic equilibrium is also possible using a Fugacity-Activity model. The F-A approach used here is based on the idea originally proposed by Kritchevsky et al. 1945 [35]. Later, this approach was further developed in Mao and Duan [41], Ziabakhsh-Ganji and Kooi [59], Li et al. [38] and Shabani and Vilcáez [50]. As discussed previously, the system is assumed to be in an instantaneous thermodynamic equilibrium which means that the fugacity of each phase is equal to each other. However, in this method, the fugacity of the gas phase will be expressed in terms of the fugacity-coefficient and the liquid phase in terms of activity.

Here the fugacity of gas phase is expressed in equation 4.11 as:

$$f_i^g = p\Phi_i y_i, \tag{4.11}$$

where p is the total pressure in the system, Φ is the fugacity coefficient of the gas phase and y_i is the molar fraction of each component in the gas phase. The liquid phase can be expressed as a function of Henry's constant h_i, activity coefficient γ and the aqueous molar fraction of component x_i (Spycher and Pruess [53], 2005):

$$f_i^l = h_i \gamma_i x_i. \tag{4.12}$$

Similar to the reference paper Ziabakhsh-Ganji and Kooi [58], the binary interaction between dissolved gasses in the aqueous phase is ignored which causes the activity coefficients in equation 4.12 for individual gas components not to depend on the presence of other gasses. This is an important assumption in the EoS used because it allows for a simplified, non-iterative solving method. A more detailed derivation of the phase fugacity expressions can be found in Appendix A.1.

Substituting the expressions for the vapour and aqueous phase fugacities gives the following expression of the thermodynamic equilibrium (see equation 4.13):

$$P\Phi_i y_i = h_i \gamma_i x_i. \tag{4.13}$$

Equation 4.13 can be rearranged to obtain the phase equilibrium constant of each component K_i:

$$K_i = \frac{y_i}{x_i} = \frac{h_i \gamma_i}{P\Phi_i}. \tag{4.14}$$

In the model used in this research study, equations 4.14 will be used to calculate K_i values for the different gas components. The equilibrium constant for the water component is calculated with a separate relation. Water is an important system component because the EoS should quantify thermodynamic equilibrium between gas mixtures and brine. The equilibrium between vapor and liquid water is determined using the relation proposed by Spycher et al. [54].

In the temperature range we are interested (5-110 degrees Celsius), the solubility of gas in water is low, which allows us to use the description of the equilibrium constant portrayed in equation 4.15. The effect of dissolved salts in the system is accounted for in the activity of water (a_{h2o})

$$K_{H_2O} = \frac{y_{H_2O}}{x_{H_2O}} = \frac{K^0_{H_2O}}{\Phi_{H_2O}P} exp\Big[\frac{(P-1)V_{H_2O}}{RT}\Big], \tag{4.15}$$

where $K^0_{H_2O}$ is the equilibrium constant of H_2O at the reference pressure of 1 bar, T is temperature in Kelvin. A more detailed derivation of the equilibrium constant of water can be found in Appendix A.2. For the partial molar volume an average value is used of 18.5 cm^3/mol, Spycher et al. [54] uses this average value because further adjusting of this parameter did not improve results significantly.

Again Spycher et al. [54] is used to calculate the equilibrium constant at reference pressure ($K^0_{H_2O}$):

$$\log(K^0_{H2O}) = -2.209 + 3.097x10^{-2}\theta - 1.098x10^{-4}\theta^2 + 2.048x10^{-7}\theta^3, \tag{4.16}$$

where θ is the temperature in degrees Celsius. Having defined a relation for the equilibrium constants of all components in the system the phase partitioning of each component can be derived using the negative flash procedure. Similar to the conventional EoS method the process will keep repeating itself until convergence criteria ϵ is met. The convergence of the equilibrium constants is defined in equation 4.17

$$max \,||\, \frac{k_i - k_i^{old}}{k_i^{old}} \,||< \epsilon. \tag{4.17}$$

Derivation fugacity parameter of the Gaseous phase

The fugacity coefficient is the a ratio between the fugacity of a component to the pressure. It is a dimensionless value and depends on the nature of the gas, temperature and pressure. By definition the fugacity coefficient of component i in solution is expressed as:

$$\phi_i^s = \frac{f_i^s}{y_i P}. \tag{4.18}$$

To obtain the fugacity coefficent in equation 4.18 the fugacity of each component is obtained from the Peng-Robinson cubic equation of state.

Derivation fugacity parameters of the Aqueous phase

The first parameter that describes the fugacity in the aqueous phase is Henry's constant of each component, h_i, which is a product of Henry's Law. Henry's Law is a gas law that states that the amount of dissolved gas is proportional to the partial pressure of that gas above the liquid. The proportionality factor related to this is Henry's law constant.

Herny's constant is obtained using the correlation of Akinfiev and Diamond [5]. The correlation is a virial-like equation for the thermodynamic properties of the aqueous phase components at infinite dilution. The correlation requires a few empirical parameters which are constrained by experimental data and are independent of temperature and pressure. The correlation can be found in equation 4.19:

$$\ln(h_i) = (1-\eta)\ln(f^0_{H2O}) + \eta \ln\Big(\frac{RT}{Mw_{H2O}}\rho^0_{H2O}\Big) + 2\rho^0_{H2O}\Delta B. \tag{4.19}$$

where temperature T is expressed in Kelvin, η is a constant for each gas component dissolved in water [-], the density of water ρ_{H_2O} is expressed in [g/cm^3], R is the gas constant and ΔB is the difference in interaction between dissimilar molecules and that of identical solvent molecules expressed in $[g/cm3]$. A full description of how the individual parameters in equation 4.19 are determined can be found in Appendix A.3

The Activity coefficient is a factor used to account for deviations from ideal behaviour in a mixture of chemical substances. Deviations from ideality are realized by modifying the concentration by a so-called activity coefficient. The activity coefficients are obtained using the approach used by the correlation of Pitzer (1973)[47], shown in equation 4.20:

$$\ln \gamma_i = \sum_c 2m_c\lambda_{i-Na} + \sum_a 2m_a\lambda_{i-Cl} + \sum_c\sum_a 2m_a m_c \xi_{i-Na-Cl}, \tag{4.20}$$

where m_c and m_a are cation and anion molalities respectively. Here λ_{i-Na} and $\xi_{i-Na-Cl}$ are second and third order interaction parameters respectively and are both dependant on pressure and temperature. In addition, λ_{i-Cl} is assumed to be equal to zero. λ_{i-Na} and $\xi_{i-Na-Cl}$ are calculated using equation 4.21

$$Par(T,P) = c_1 + c_2T + \frac{c_3}{T} + c_4P + \frac{c_5}{P} + c_6\frac{P}{T} + c_7\frac{T}{P^2} + \frac{c_8P}{630-T} + c_9T\ln(P) + c_10\frac{P}{T^2}. \tag{4.21}$$

Values for c for λ_{i-Na} and $\xi_{i-Na-Cl}$ are component specific constants. The constant can be found in the table of Appendix A.4 together with a more detailed explanation of the activity coefficient.

The molality of anions and cations is assumed to be solely dependant on the salinity of our reservoir brine solution. There would be some anions and cations present resulting from the dissolved gasses but this amount is assumed to be negligible. The salinity of the brine is assumed to be constant throughout the reservoir, so the molality of anions and cations can also be assumed to be constant. The benefit of using the Pitzer correlation is that it is reliable for a high molality of salt (up to 6 molal NaCl).

4.2.3. Initial K-value estimation

The ideal equilibrium constant K of each component, between the vapour and an aqueous phase, is used to initiate the thermodynamic model. The ideal k-values are only dependant on component properties and surrounding conditions and not dependant on component composition. To describe the ideal distribution between components in aqueous and vapour phase, the equilibrium constant is obtained from the standard Raoult's Law. The following derivation of the ideal equilibrium constant was obtained from Ballard [8]:

$$y_i\Phi_{iV}P = x_i\gamma_{iAq}p_i^{sat}\exp\left[\int_{p_i^{sat}}^{P}\frac{v}{RT}dP\right], \tag{4.22}$$

where x and y are the liquid and vapour mole fraction of component i respectively, Φ is the fugacity coefficient, γ is the activity coefficient, P^{sat} is the saturation pressure. Note that temperature T is given in Kelvin and pressures in bar. In equation 4.22 the following assumptions are made:

1. It is assumed that component i in the aqueous phase is so dilute that the activity coefficient can be approximated by the infinite dilution activity coefficient.
2. The fugacity coefficient of component i in the vapour phase is assumed to be equal to unity
3. The exponential term in equation 4.22, the Poynting factor, is also assumed to be equal to unity.

These assumptions will reduce the Raoult's Law as described in equation 4.22 to:

$$K_i = \frac{y_i}{x_i} = \frac{p_i^{sat}}{P}\gamma_{iAq}^{\infty}. \tag{4.23}$$

In equation 4.23 the saturation pressure for each component i is described by:

$$p_i^{sat} = P_{c_i} \exp\left[a_1 + \omega_i a_2\right]. \tag{4.24}$$

Here $P_{c,i}$ is the critical pressure of component i, and ω_i is the accentric factor of each component i. The empirical parameters are determined using equations A.29 and A.30 in the Appendix A.5.

The saturation pressure of water is described by a separate relation, also known as the Antoine equation as:

$$p_{H_2O}^{sat} = P_{c_i} \exp\left[a_1 - \frac{a_{2,i}}{T + a_{3,i}}\right]. \tag{4.25}$$

Here the unknown empirical parameters are given in appendix A.5. The activity coefficient with infinite dilution is described by:

$$\gamma_i^{\infty} = \exp\left[a_1 + a_2 N_i + \frac{a_3}{N_i}\right], \tag{4.26}$$

where N_i is the number of carbon atoms in each component i. Here again the empirical parameters a_x can be found in Appendix A.5 in table A.5. Note that the infinity diluted activity coefficient of water is assumed to be equal to one.

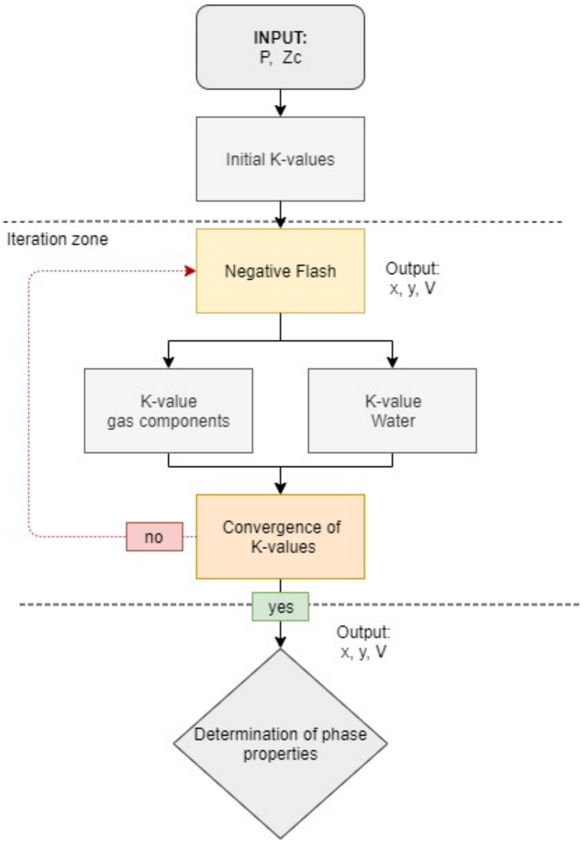
INPUT:
P, Zc
Initial K-values
Iteration zone
Negative Flash
Output:
x, y, V
K-value
gas components
K-value
Water
no
Convergence of
K-values
yes
Output:
x, y, V
Determination of phase
properties

Figure 4.1: Schematic overview of the Fugacity-Activity model

5

Physical properties

In this chapter, the physical properties that affect flow in the underground aquifer will be addressed. A distinction will be made between physical reservoir aspects that affect flow and phase properties.

5.1. Flow Properties

5.1.1. Porosity

In the model used in this research, the porosity is assumed to be homogeneous and slightly compressible. The value of the reservoir porosity is assumed to be 0.3 [-], which is typical for a sandstone formation. The rock compressibility is taken into account and this effects the porosity with pressure, as shown in eq .5.1:

$$\phi = \phi(1 + c_r(P - P_{ref}). \tag{5.1}$$

Here c_r is the rock compressibility and P_{ref} is the reference pressure taken at 1 bar.

5.1.2. Permeability and Relative Permeability

In the model used for this research, the permeability of the aquifer is assumed to be homogeneous throughout the reservoir. The permeability is assumed to be equal to that of a typical sandstone formation of 100 mDarcy.

The relative permeability is the dimensionless value of the effective permeability of each phase, which in our case is the vapour or aqueous phase. The relation of the relative permeability of both phases can be given by correlation used in Class et al. [13] and Elenius et al. [18]. The correlation is based on Brookes-Corey related functions as:

$$S_{e,w} = \frac{S_w - S_{wr}}{1 - S_{wr}}, \tag{5.2}$$

$$k_{r,Aq} = S_{e,w}^4, \tag{5.3a}$$

$$k_{r,V} = 0.4(1 - S_{e,w}^2)(1 - S_{e,w})^2 - C. \tag{5.3b}$$

Here S_w and S_{wr} are the water saturation and residual water saturation respectively, $k_{r,Aq}$ is the aqueous phase relative permeability, $k_{r,V}$ is the vapour phase relative permeability. C is a correction factor used to fix $k_{r,V}$ to zero when $S_g = S_{g,r}$, here C = 0.0109. Note that here the effective water saturation has a deviating definition compared to the classical Brookes-Corey definition.

In figure 5.1 the relative permeability curves resulting from the relations defined in equations 5.3 are shown.

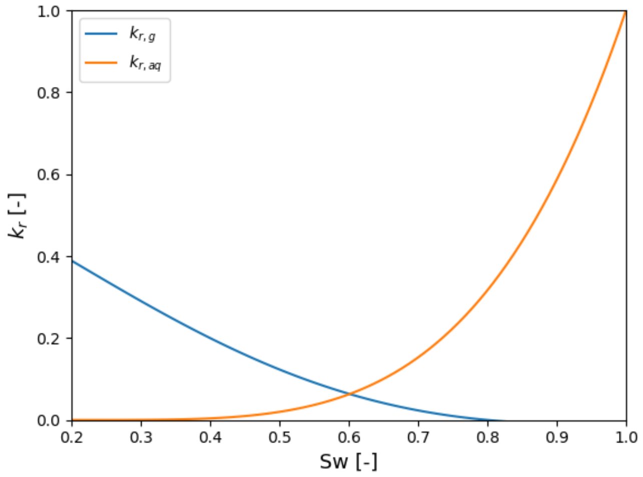

Figure 5.1: Relative permreability curves for the aqueous and gaseous phase with a residual saturation of both phases at 0.2 [-].

5.1.3. Capillary pressure

The capillary pressure in this model is also a function of the effective water saturation as shown by:

$$p_c = \frac{p_e}{\sqrt{S_e}}. \tag{5.4}$$

Here p_c is the capillary pressure, p_e is entry pressure and S_e is the effective saturation. The entry pressure p_e is taken to be 20 kPa.

5.1.4. Diffusion

In equation 3.5, the description of diffusive fluxes of components in mobile phases is given. Diffusion is the irreversible process of mixing driven by differences of concentration, which is described by Fick's Law as [10]:

$$J_{ij} = \sum_{i}^{n_c} D_{ik}^{j} \nabla x_{ij}. \tag{5.5}$$

Here J denotes the diffusive flux of component i in phase j, k is the component other than component i is this binary system and D_ik is the diffusivity coefficient between the two present components. Note that Fick's Law (shown here in equation 5.5) is only valid for binary components. For a binary system, the diffusivity coefficient matrix will be symmetric, resulting in $D_{ik}^{j} = D_{ki}^{j}$.

In a system of multi-component mixtures, there will be as many diffusion coefficients as there are pairs of components in the system. Furthermore, the fluxes and concentration gradients of all present components are inter-dependant on each other. This makes Fick's Law not applicable for a multi-component system, unless in specific circumstances when solutions are sufficiently dilute.

For addressing the diffusivity in a multi-component system the generalized Maxwell-Stephan equation can be used, shown here in equation 5.6

$$F_i = \sum_{k \neq i} \xi_{(i,k)} x_k (J_i - J_k).. \tag{5.6}$$

Here F_i is the driving force (concentration gradient) on component i, ξ is the friction coefficient between components i and k. x_k is the mol fraction of component k and J are the diffusive component velocities.

5.2. Phase Properties

In this section, the determination of density and viscosity of both phases will described.

5.2.1. Aqueous Phase Properties

In the model constructed in this study, the aqueous phase initially consists of a resident brine solution of sodium chloride. After injection of the gas stream, gas components will dissolve into the aqueous solution which will alter the properties of this phase.

For the determinations of the aqueous phase properties solely the amount of dissolved CO_2 is taken into account due to the correlations available. This simplifying assumption will affect the accuracy of the results of the model, however, since the solubility of CO_2 is still affected by the presence of impurities and since CO_2 is the heaviest component introduced, the effects may still be limited.

Density of the Aqueous Phase

The density of the aqueous phase is calculated in two steps, first the density of the aqueous brine solution is determined after which the effect of dissolved CO_2 is taken into account which results in the final density.

Brine density

The empirical correlation used to determine the brine solution density was developed by J.P. Spivey and W.D. McCain Jr [31]. This correlation is valid for a temperature range of 0-275°C, pressure range from 0.1-200 MPa and salinity levels from 0-25 wt% NaCl. The IAPWS-95 international standard equation of state for water was used to determine the coefficients applied in the correlation. The coefficients for the salinity term were found later by non-linear regression on the brine density database. The formulation of brine solution density is shown here in equation 5.7:

$$\rho_b(p,T,C_m) = \rho_{b0}(T,C_m)\exp\left[I_b(p,T,C_m) - I_b(p,T,C_m)\right]. \tag{5.7}$$

Where p_0 is the reference pressure and was taken as $70MPa$, $\rho_{b,0}$ is the brine solution density at reference pressure and I_b is an empirically derived parameter dependant of temperature. The derivation of these parameters can be found in Appendix B.1.

Aqueous Solution Density

For the density of brine with dissolved CO_2 components, the correlation developed by Garcia is used [25]. Garcia's correlation is give as follows:

$$\frac{1}{\rho_{aq}} = \frac{x_{Co_2}V_{\phi,CO_2}}{M_T} + \frac{M_{H_2O}x_{H_2O}}{\rho_b M_T}. \tag{5.8}$$

Where ρ_b is the density of the brine solution in $[kg/m^3]$, M_{H_2O} is the molecular weight of water in $[kg/mol]$, V_ϕ is the apparent molar volume of dissolved CO_2 in $[m^3/mol]$, x_{H_2O} and x_{CO_2} are the molar fraction of H_2O and CO_2 in the water phase respectively. M_T is the total molecular weight and is formulated as:

$$M_T = M_{H_2O}x_{H_2O} + M_{CO_2}x_{CO_2} + M_{imp}x_{imp} \tag{5.9}$$

The apparent molar volume (or partial molar volume) of CO_2 was determined using a correlation developed by Garcia [25]. In this correlation, the partial molar volume is only dependant on pressure because experimental results show that the partial molar volume is independent of pressure for temperatures below 300 °C. The correlation used for the partial molar volume is:

$$V_\phi = 37.51 - 9.585e - 2 * \theta + 8.740e - 4 * \theta^2 - 5.044e - 7 * \theta^3. \tag{5.10}$$

where θ is temperature in degrees Celsius.

Viscosity of the Aqueous Phase

Similar to the aqueous phase density, the aqueous phase viscosity is determined in two stages. First an accurate viscosity model developed by Moa and Duan [42] is used to derive the brine viscosity after which the correlation by Islam and Carlson [4] is used to account for dissolved CO_2.

The correlation by Moa and Duan is valid for temperatures between 273-623 Kelvin, 1-1000 bar and up to 6 mol/kg of NaCl concentration. The viscosity of aqueous solutions is mainly dependant on temperature, into a lesser extent on salinity and even less dependant on pressure [42]. The correlation developed by Mao and Duan is shown below by:

$$\ln \mu_r = Am + Bm^2 + Cm^3, \tag{5.11}$$

$$\mu_r = \frac{\mu_{sol}}{\mu_{H_2O}}. \tag{5.12}$$

Here μ_r is the relative viscosity, μ_{sol} is the viscosity of the solution and μ_{H_2O} is the viscosity of pure water in $[Pa \cdot s]$. Parameter m is the molality $[mol/kg]$ of salt present. A, B and C are polynomial parameters that are dependant on temperature. The derivation of these parameters can be found in Appendix B.2.

Using the viscosity of brine the correlation of Islam and Carlson [4] can be used to determine the effect of dissolved CO_2 on the viscosity. This correlation is valid for temperatures up to $100°C$ and for pressures ranging from 1-600 bar. The viscosity correlation of Islam and Carlson is shown by:

$$\mu_{brine+CO_2} = \mu_{brine}(1 + 4.65x_{CO_2}^{1.0134}). \tag{5.13}$$

5.2.2. Non-Aqueous Phase Properties

The non-aqueous phase consists of the injected gas components and very small (negligible) amounts of vaporized water. The behaviour of this phase is more interesting because under certain critical conditions the normal gas phase can transform into the supercritical phase. This super-critical phase is treated as a gaseous phase in the model but it can obtain the properties of a liquid phase.

Density of the Non-Aqueous phase

The density of the non-aqueous phase is determined using the Peng-Robinson EoS [14]. From the PR EoS the molar volume (V_m) is obtained which is used to calculate the phase density. The gaseous phase density is calculated using the relation shown in equation 5.14.

$$\rho_g = \frac{M_g}{Vm_g} \tag{5.14}$$

Here M_{aq} is the average molar mass of the non-aqueous phase, which is derived using equation 5.15

$$M_g = \sum_{i=nc} Mw_i * y_i, \tag{5.15}$$

where nc is the number of gas components present, Mw_i is the molecular weight of component i and y_i is the vapor mol fraction of component i.

Viscosity of the Non-Aqueous phase

Due to the lack of a simple and accurate correlation, (and due to time constraints), the gaseous phase viscosity was chosen to be constant. The viscosity value chosen is similar to that of Elenius et al. [18] at 15 centi-poise.

6

Process Energy Framework

In this chapter, an investigation into the energy costs of the complete carbon capture and storage (CCS) process is presented.

6.1. Introduction to Framework

The goal of this framework is to obtain a basic understanding of the total power consumption involved in the whole CCS chain and specifically how the total power consumption depends on different types of CCS stream. For this framework, the power consumption of the CCS process is divided into two main parts:

1. the power consumption of the capturing and purification stage,
2. and the power consumption for the transportation and injection stage.

Eventually, the framework will be implemented into a generic model that generates the total power consumption of the CCS process for a 1000 MW power plant. The inputs to this model is the type of combustion source and the separation-purification technique applied.

6.1.1. Power Consumption of CO_2 Capture and Purification

The energy costs of the capturing and purification depends on the type of capturing & separation technique combined with the combustion source. In chapter 2 of this study, a detailed investigation was performed on the type of capturing and separations techniques including the resulting impurity levels. For the determination of the total power consumption of the separation and purification stage, the method developed in Eftekhari et al. [17] was used. This approach assumes a 1000 MW power plant which is fueled by various fuels (e.g. natural gas) with a certain efficiency factor. Using the efficiency factor and the emission factor of the fuel source, the amount of produced CO_2 can be determined in [kg CO_2/s], as shown below:

$$Em_{rate} = \frac{1000[MW]}{\eta_{PP}} \cdot Em_{factor}. \tag{6.1}$$

Here E_{rate} is the resulting emission rate (or mass flow-rate) in [kg CO_2/s], Em_{factor} is the emission factor specific for the type of combustion fuel (coal or gas) used in [kg CO_2/MJ] and η_{pp} is the efficiency factor of the powerplant.

Similar to the method of Eftekhari et al. [17], we use a rough estimate of the energy penalty for each separation & purification technique. The energy penalty is specific to the type of technique used in combination with the combustion fuel type. For example, the energy penalty for a natural gas (NG) fired powerplant with liquid MEA purification is roughly 3.5 [MJ/kg CO_2]. Multiplying the energy penalty of the specific separation technique with the emission rate will results in the total power consumption of this first stage, shown as:

$$PC_1 = em_{rate} \cdot E_{purification}. \tag{6.2}$$

Here PC_1 is the power consumption of this first stage in [MW] and $E_{purification}$ is the energy penalty for CO_2 capture and separation in [MJ/kg CO_2]. A schematic overview of the calculation and variables related to the power calculation of this first stage is shown in figure 6.1. Here the power consumption calculations of the first stage are referred to as function 1.

6.1.2. Power Consumption of Transportation and Sequestration Stage

For this second stage, it is assumed that transportation takes place in a straight pipeline to the injection location where, after re-compression, it will be injected directly into a subsurface aquifer. By making this assumption, power consumption of the intermittent storage phase in the CCS process stream is neglected. For this framework, it is also assumed that the energy costs of transportation and injection are purely dependant on the amount of energy that is required to pressurize the pipeline and the wellbore during injection. Therefore possible energy costs for heating or cooling elements are ignored. By assuming a straight and constant diameter for the pipeline and wellbore, the possible pressure and temperature changes at choke-points etc. (Joule-Thompson effect) are neglected.

The compression power necessary for pipeline transportation depends on the pressure loss per kilometer pipe, the pump efficiency and the volumetric flow rate of the gas stream. This can be formulated in

$$Power_{compressor} = \frac{Q \cdot \Delta P}{\eta_{pump}}, \tag{6.3}$$

where Q is the volumetric flow-rate and can be determined by $Q = em_{rate}/\rho_g$. Since the power consumption of intermittent storage is neglected, the emission rate from the powerplant is also used as the mass flow rate for transportation and injection. Note that due to two-dimensional limitations of the injection model, the flow-rate used as input here is divided by 360 to obtain a rough estimate of the volumetric flow-rate in the 2-dimensional space. The pressure difference that the compressor (compressor A) has to achieve for transportation is defined as, the pressure at the beginning of transportation (P2) minus the initial pressure (P1). The pressure needed at the start of transportation is in turn dependant on the pressure drop over the length of pipe and the preferred pressure at injection location (P3).

In this framework, we assume a pressure loss of 0.25 bar/km of pipeline, which was taken from a similar study by Christiaanse [12]. For the determination of pressure drop along the pipeline Christiaanse [12] makes the following assumptions:

- single-phase fluid flowing through constant diameter pipe of 0.1 m and 0.5 mm roughness,
- fluid is fully turbulent and incompressible,
- and the pressure drop along the pipe occurs due to viscous effects and follows the Darcy-Weisbach equation.

To maintain single-phase flow through the pipeline, the gas stream must be kept at supercritical or liquid conditions. Supercritical conditions for pure CO_2 this means the pressure must be kept roughly above 74 MPa and at around 307 Kelvin [12]. To guarantee single phase flow through the pipeline the required pressure at the end of transportation (P3) is assumed to be 80 bar.

After transportation to the injection location, the gas stream will be re-pressurized one last time for injection into the subsurface reservoir. At this stage, different simplifying assumptions can significantly affect the injection dynamic and resulting power consumption. Assuming a constant injection rate (mass flow rate), the pressure needed for injection will increase over time and thereby affect the compression required for injection. Similar to transportation, power consumption before injection is determined using equation 6.3. Here the required pressure difference (ΔP) is defined as the pressure at the wellhead (P4) minus the pressure at the end of transportation (P3). As stated previously, pressure at the end of transportation is fixed at 80 bar to guarantee a single-phase flow through the transportation pipeline. The pressure at the wellhead is not fixed (P4) as it is dependant on the reservoir pressure (P5).

To determine the required pressure at the wellhead (P4), the hydrostatic forces must be taken into account. The wellhead pressure difference can be derived by:

$$\delta P_{grav} = \rho_{g,sc} \cdot g \cdot \Delta z. \tag{6.4}$$

Here $\rho_{g,sc}$ is the density the supercritical gas stream, g is the gravitational acceleration factor and Δz is the height difference along the wellbore. The pressure at the wellhead (P4) is defined as the reservoir pressure minus the wellhead pressure difference. The reservoir pressure is dynamic over time and will be obtained from the injection model build in DARTS.

The total power consumption is defined as the sum of the power consumption at both compressors. A schematic overview of the calculation and variables related the the power calculation of this second stage is shown in figure 6.1. Here the calculations related tot he power consumption of the second stage are referred to as function 2.

6.1.3. Process Energy Model - Generic model

The previously described functions to determine the total power consumption throughout the CCS process are implemented into the DARTS model to obtain a generic model. The input to this model is a combination of the fuel type of the powerplant and a specific capture and purification technique. This input is given to ”function 1”, which next to the power calculation will output the composition of the emitted gas stream and the emission rate (or mass flow rate). Both the gas composition and emission rate outputs will be used as inputs for the gas injection model built in DARTS. A schematic overview of the generic model can be found in figure 6.2.

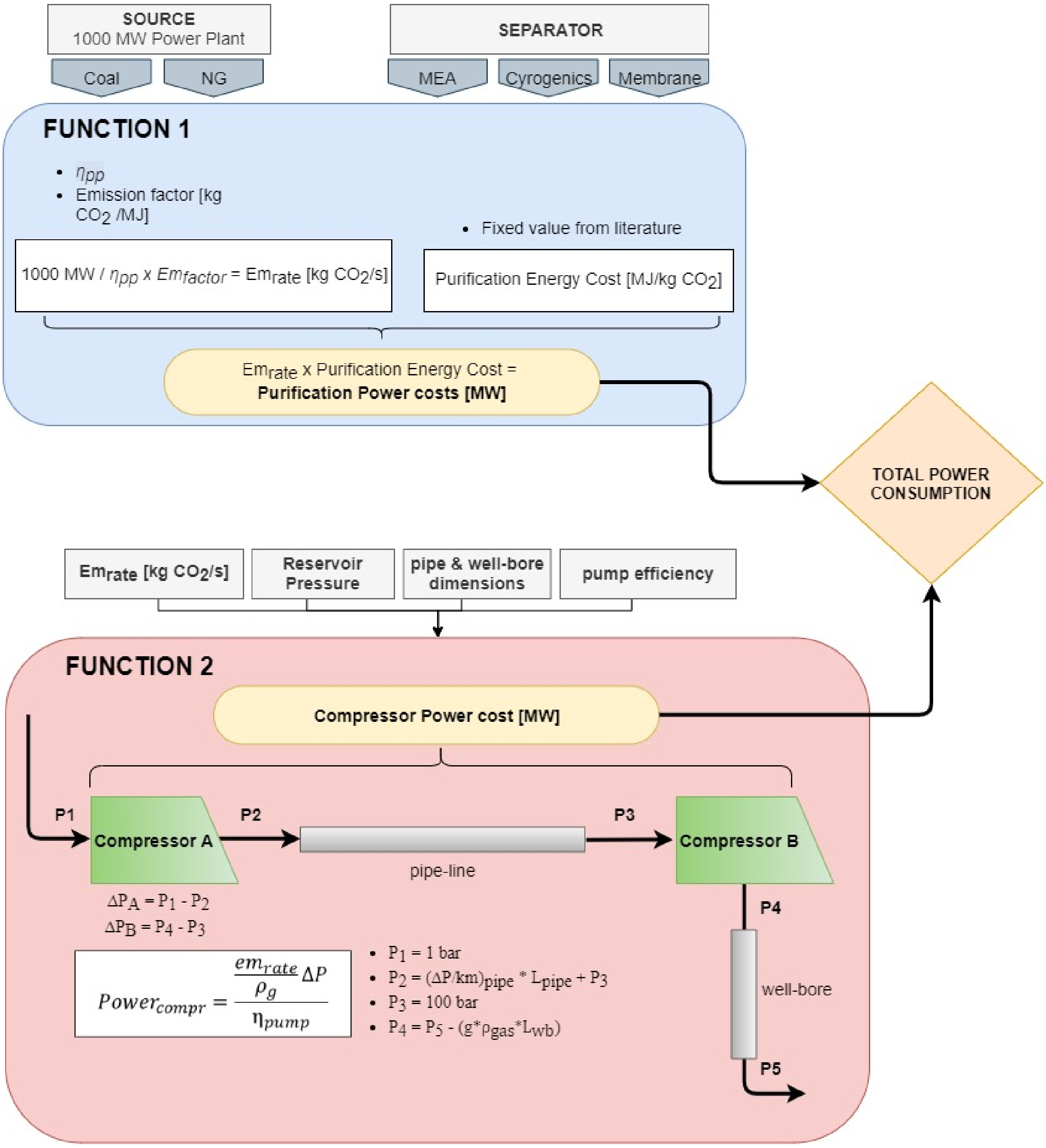
SOURCE
1000 MW Power Plant
Coal
NG
SEPARATOR
MEA
Cyrogenics
Membrane
FUNCTION 1
ηpp
Emission factor [kg CO2 /MJ]
Fixed value from literature
1000 MW / ηpp x Emfactor = Emrate [kg CO2/s]
Purification Energy Cost [MJ/kg CO2]
Emrate x Purification Energy Cost =
Purification Power costs [MW]
TOTAL POWER CONSUMPTION
Emrate [kg CO2/s]
Reservoir Pressure
pipe & well-bore dimensions
pump efficiency
FUNCTION 2
Compressor Power cost [MW]
P1
Compressor A
P2
pipe-line
P3
Compressor B
P4
well-bore
P5
ΔPA = P1 - P2
ΔPB = P4 - P3
Powercompr = (emrate/ρg ΔP) / ηpump
P1 = 1 bar
P2 = (ΔP/km)pipe * Lpipe + P3
P3 = 100 bar
P4 = P5 - (g*ρgas*Lwb)

Figure 6.1: Schematic overview of the functions used to determine the power consumption of each stage in the CCS process

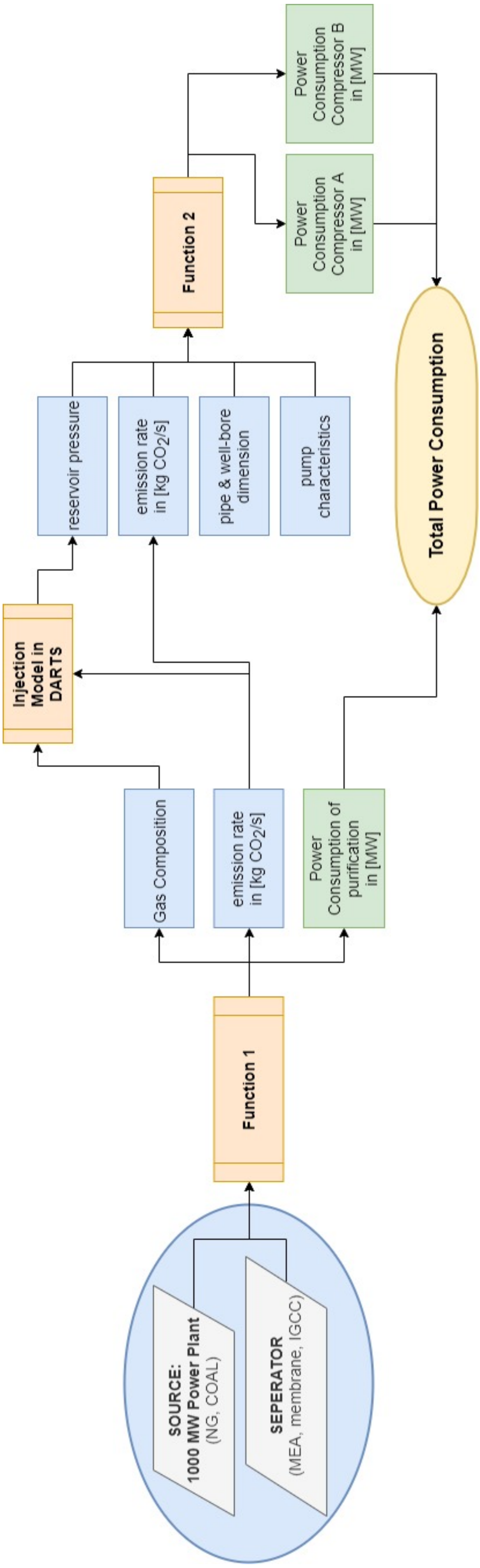
SOURCE:
1000 MW Power Plant
(NG, COAL)
SEPERATOR
(MEA, membrane, IGCC)
Function 1
Gas Composition
emission rate in [kg CO_2/s]
Power Consumption of purification in [MW]
Injection Model in DARTS
reservoir pressure
emission rate in [kg CO_2/s]
pipe & well-bore dimension
pump characteristics
Function 2
Power Consumption Compressor A in [MW]
Power Consumption Compressor B in [MW]
Total Power Consumption

Figure 6.2: Schematic overview of generic model to determine the total power consumption of the CCS process

7

Results

In this chapter, the results are presented for the validations of the implemented thermodynamic model and phase property correlations. Hereafter, an overview of the large scale reservoir models used for the fully physical simulations in DARTS are described. The simulation results in DARTS are presented from the section 7.3 onwards, starting with the results investigating convective mixing in a large scale horizontal reservoir. After which the results of gas injection, post-injection migration and eventually behaviour of impure components in a large scale inclined reservoir are presented. The last section of this chapter will focus on the results obtained from the process energy framework.

7.1. Validations

In this section, the validations of the thermodynamic model and the phase properties will be presented.

7.1.1. Validation F-A Thermodynamic model

In the following subsection, the results of the developed F-A thermodynamic model will be compared and visually validated with the results found by the base model developed by Ziabakhsh-Ganji and Kooi [58]. Due to the lack of simulation data from literature, validation of the results are done by visual comparison. In figures 7.1 and 7.2 are results obtained from injection of pure CO_2. Figure 7.1a shows the behaviour of the liquid mol fraction of CO_2 with pressure at 90°C and 2 molal NaCl salinity and is compared with the literature results in figure 7.1b. The results found in literature have in turn been validated against experimental

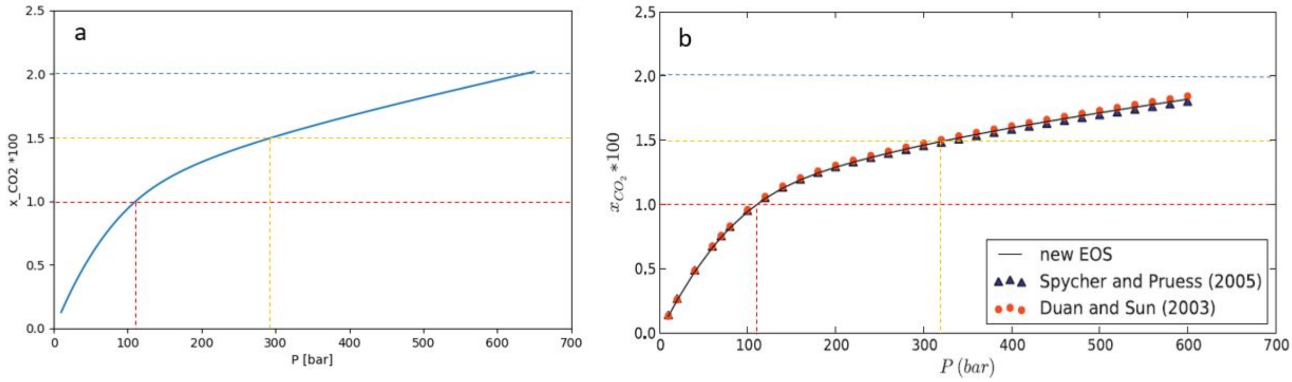

Figure 7.1: Validation of liquid mol fraction CO_2 for pressures up to 650 bars, at 90 degrees C and at 2 molal NaCl salinity. (a) Results of developed F-A model, (b) Results found in literature [58]

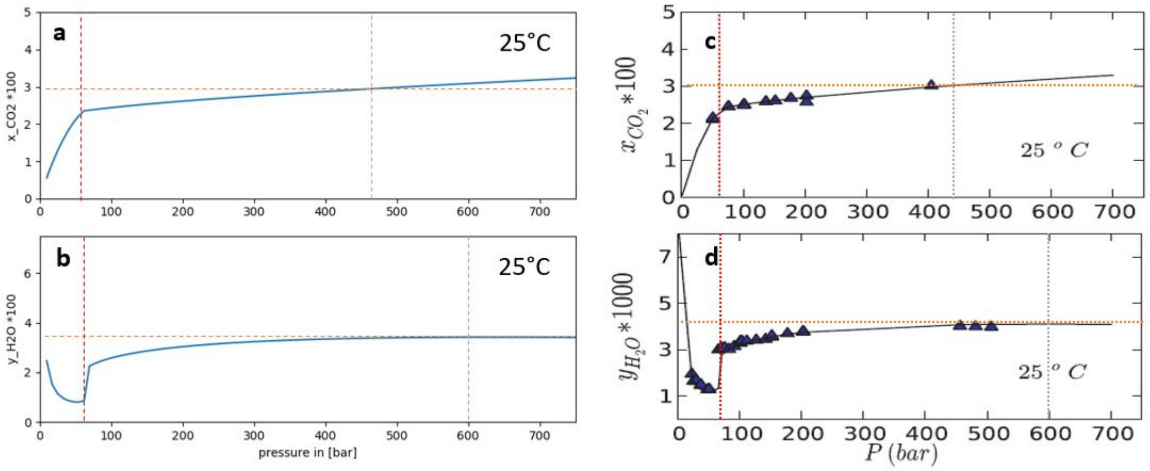

Figure 7.2: Validation of liquid mol fraction CO_2 and gaseous mol fraction H_2O over pressur at 25 degrees C in pure water. (a) Results of developed F-A model, (b) Results found in literature, [58]

data produced by Spycher and Pruess (2005) and Duan and Sun (2003), which can also be found in Ziabakhsh-Ganji and Kooi [58]. In figure 7.2 the liquid mol fraction of CO_2 and the gaseous mol fraction of H_2O are depicted over a pressure range at a temperature of 25°C in pure water. Visual comparison of both figures with literature [58] finds that the results are very reasonable.

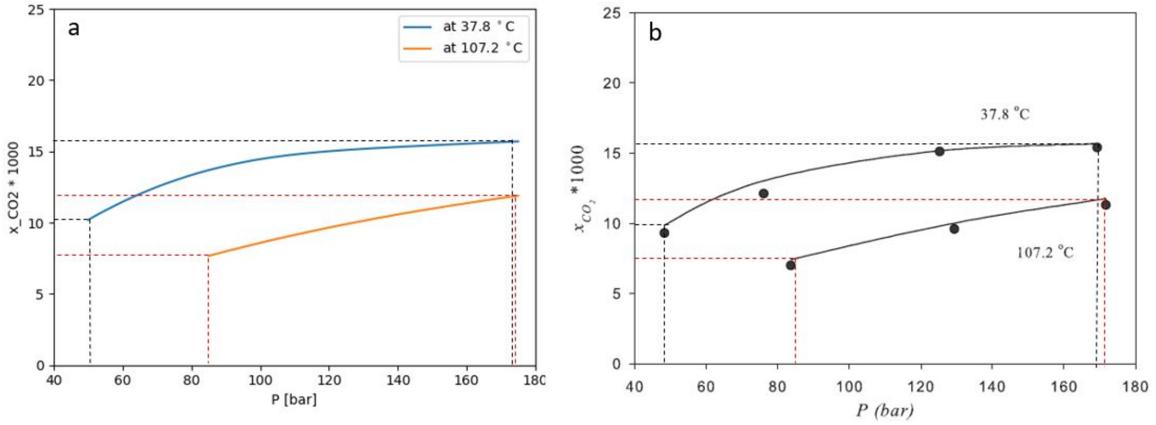

Figure 7.3: Validation of liquid mol fraction CO_2 during injection of CO_2, CH_4, H_2S mixture with mol fraction of 0.6, 0.3 and 0.1 respectively. (a) Result of developed F-A model, (b) Results found in literature [58]

In figure 7.3 the solubility of CO_2 is shown as result from injecting a gas mixture. The gas mixture consists of CO_2, CH_4, H_2S components which are injected in overall compositional mole fractions of [0.6, 0.3, 0.1]. The results shown here are under varying conditions of 37.8°C and 107.2°C and without any salinity present. Note that the symbols in the literature results represent experimental data points used to validate the model [58]. An important observation that can be made from these results is that the solubility of CO_2 is reduced in the presence of impure components compared to pure injection found in figures 7.1 and 7.2. Again using visual comparison the results are very compatible with the results found in literature [58].

In figure 7.4 the liquid mol fraction of single component H_2S injection has been generated for pressures up to 200 bar for a variety of salinity's at 60°C and 90°C. Again the generated results are compared with literature, however, some distinct differences are visible. In the

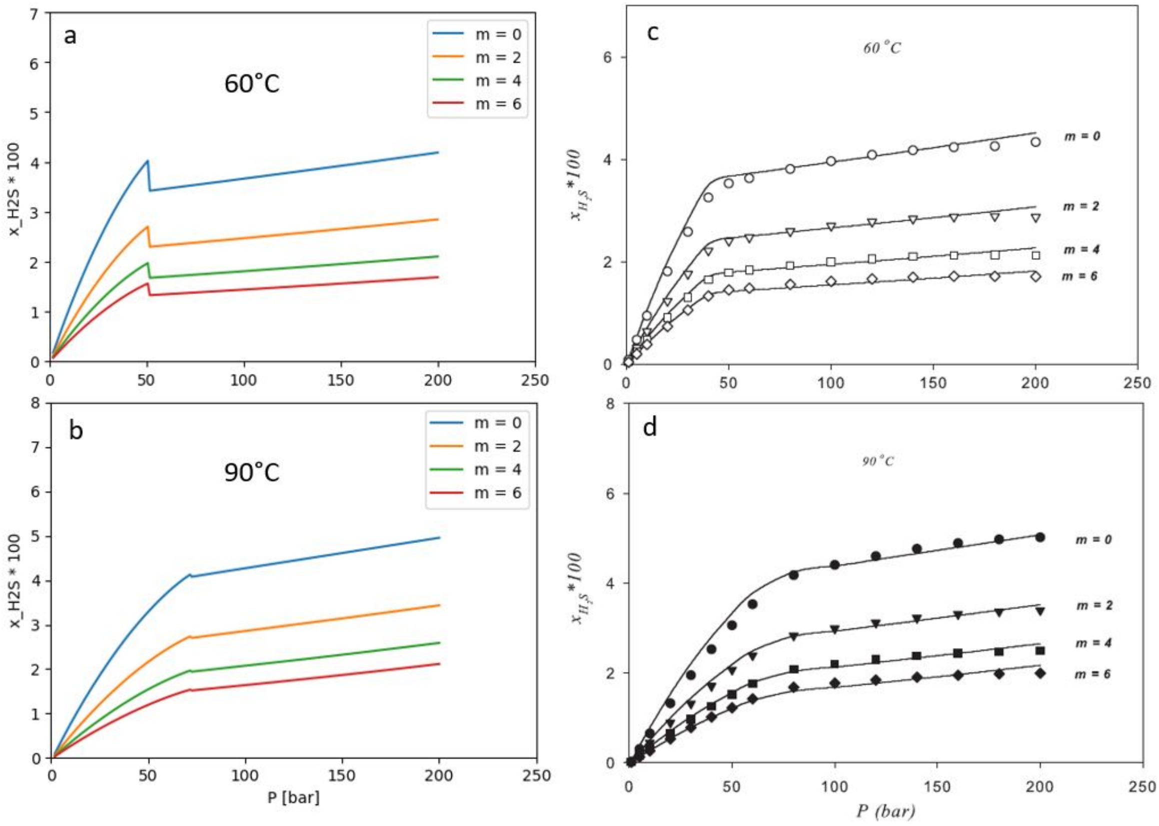

Figure 7.4: Validation of liquid mol fractions of pure H_2S injection over pressure at 60 and 90 degrees C for a range of brine salinity's. (a) & (b) show the results generated by the developed F-A model, (c) & (d) show the results found in literature [58]

generated results, an anomaly can be found at the curvature of the graphs. This anomaly seems to be greater at lower temperatures and reduces at higher temperatures. From further experiments, it has become clear that this erroneous result is only present with H_2S which might indicate that here some of the component specific parameters are not correctly introduced. Disregarding this erroneous anomaly, the result seems to be in the correct order of magnitude and show the correct behavioural trends with pressure.

The solubility of components N_2 and CH_4 including their validations with literature can be found in Appendix C.1.

In figure 7.5 the results of CO_2 solubility behaviour with the presence of impurities is compared with the results found in literature. This is an important result as it shows that in the presence of individual impure components the solubility of CO_2 is reduced. From the results, it is visible that the solubility of CO_2 is most impacted by the presence of methane and least by the presence of hydrogen sulfide. These findings correlate strongly with results found in literature where the same findings can be interpreted. Note that for these results a 5% mass percentage (not compositional %) of impurity component was used.

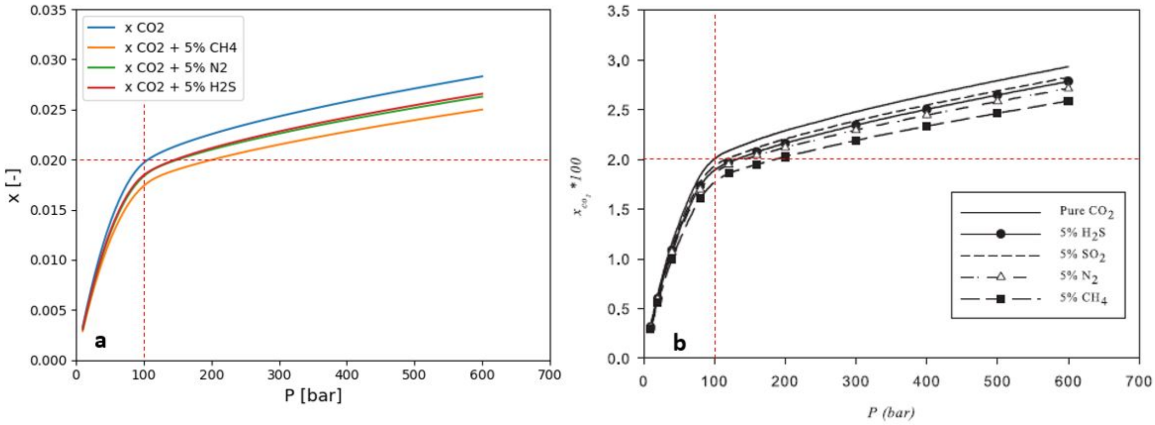

Figure 7.5: Validation of the solubility of CO_2 with presence of single component impurities at 50 $°C$, (a) show the results generated by the developed F-A model, (b) show the results found in literature [58]

7.1.2. Validation of phase property correlations

In this subsection, the generated phase properties are compared and validated with existing results from literature.

Validation of Aqueous phase density

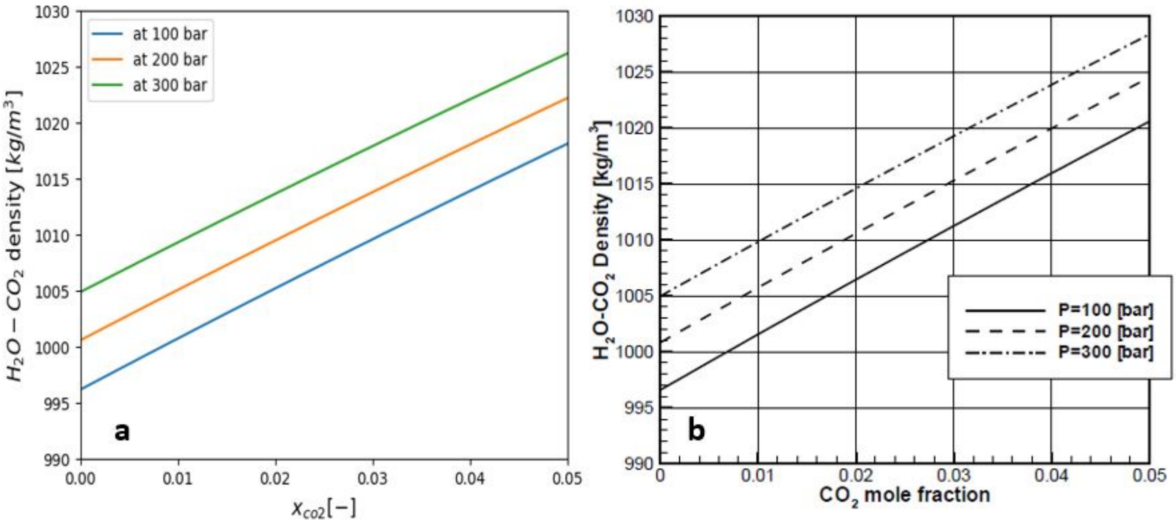

Figure 7.6: Validation of the density of the aqueous phase for a range of CO_2 liquid mol fractions in pure water,at 22°C. (a) Results generated by the developed model, (b) Results from literature [25]

In figure 7.6, the effect of dissolved CO_2 in pure water on density is shown at 22°C for a variety of pressures. For the generation of both results, the correlation for the effect of dissolved CO_2 on the density developed by Gacia [25] is used. The only input parameter that differs between the two results is the determination of pure water density.

The results match the findings in literature very decently.

Validation of the Aqueous phase viscosity

In figures 7.7 and 7.8, the viscosity of the aqueous phase is validated for temperature and pressure dependency respectively. In figure 7.7, the viscosity results of the aqueous phase over a temperature range up to 100°C is compared to results found in literature [4]. In these results comparisons can be made for pure water, a brine solution with 1 molal NaCl and an

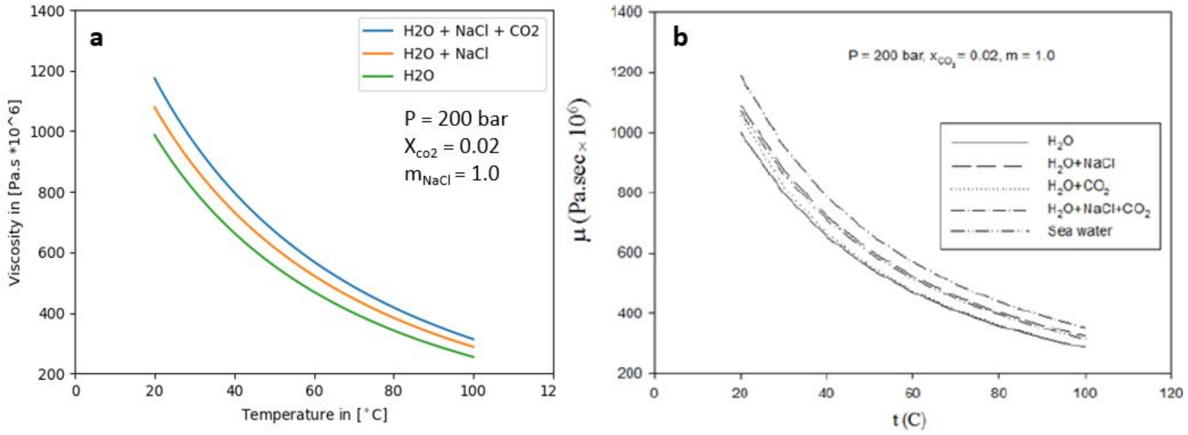

Figure 7.7: Validation of the aqueous phase viscosity over temperature for pure water (H_2O), saline water (H_2O+NaCl) and an aqueous saline solution including dissolved CO_2 (H_2O+NaCl+CO_2) at conditions shown in figure. (a) shows the results generated by the developed in the model, (b) show the results found in literature, [4]

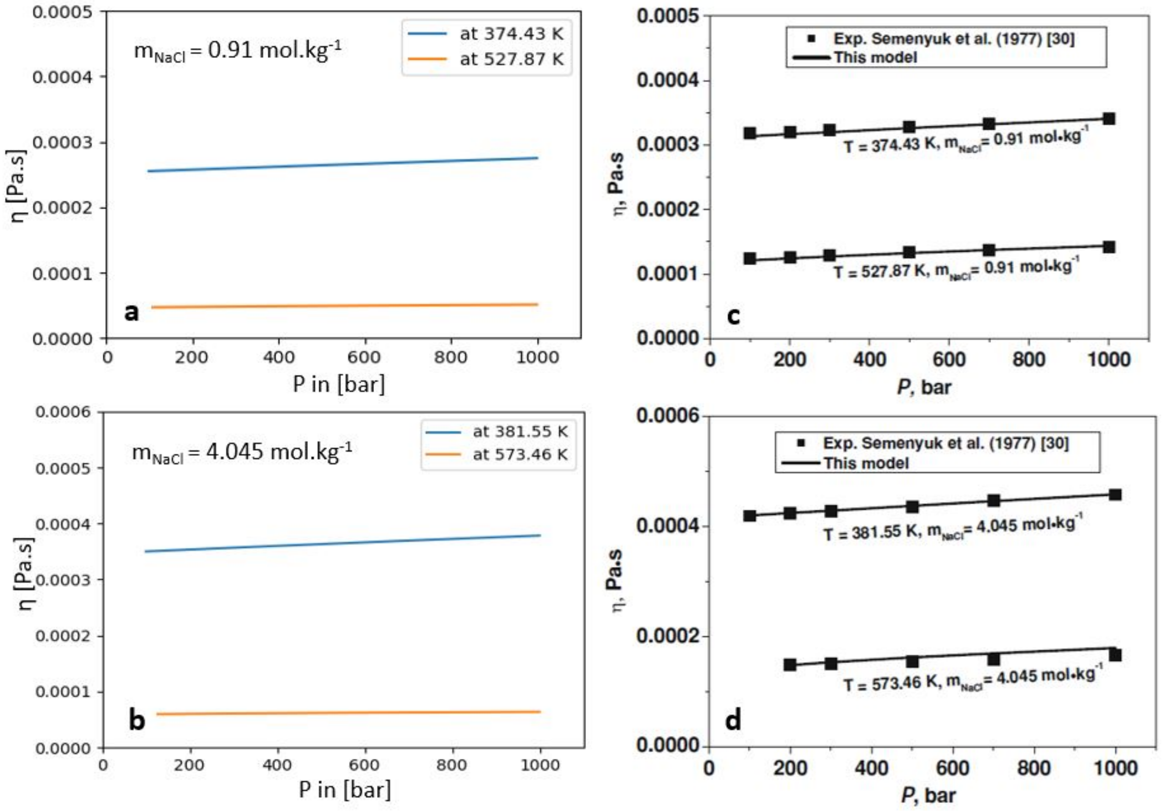

Figure 7.8: Validation of the brine viscosity over pressures for varying temperatures and salinity's. (a) & (b) show the resutls generated by the model, (c) & (d) show the results found in literature, Mao and Duan [42]

aqueous solution with CO_2 liquid mol fraction of 0.02 [-]. Both results generated in figure 7.7 use the same formulation to account for CO_2 in the aqueous viscosity [4]. The viscosity of pure water and brine that are needed as input for this correlation are, however, generated using varying correlations which could explain the small deviations witnessed. The differences between the results generated by the model and those found in literature are very small.

In figure 7.8 the viscosity of brine solutions with varying salinity are shown over a pressure range up to 1000 bars and are compared with results found in Mao and Duan [42]. For the generation of both literature and model results the same correlation for the viscosity are used, namely those developed by Mao and Duan [42]. However, the input of water density is different which might cause a slight deviation compared to literature.

Validation of Non-Aqueous Density

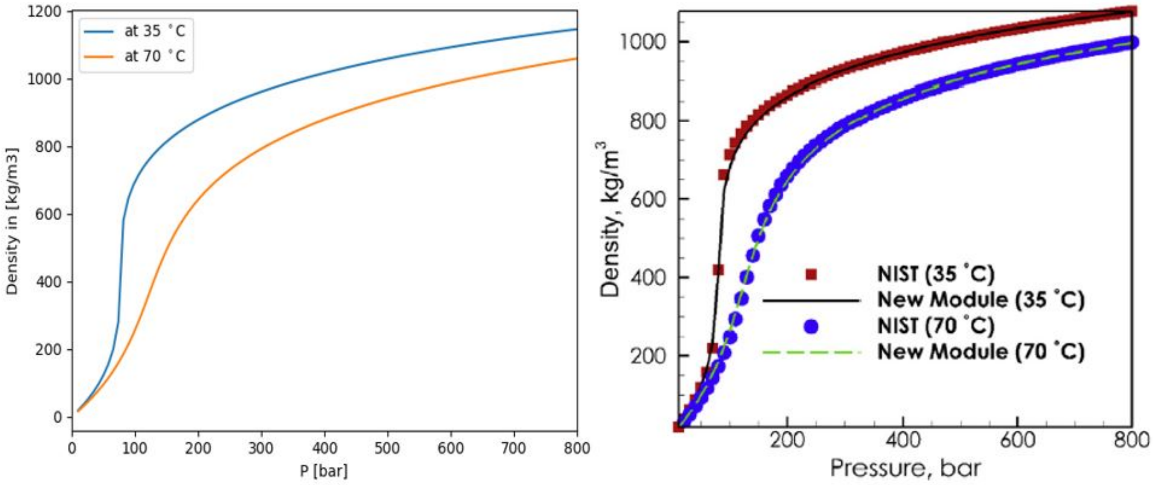

Figure 7.9: Validation of the non-aqueous phase density for pressure up to 800 bars and at 35 and 70°C and no salinity. (a) Result generated by developed F-A model in combination with the molar volume from PR EoS. (b) Results from literature Shabani and Vilcáez [49]

.

In figure 7.9, the density of the non-aqueous phase of pure CO_2 is compared with results obtained from literature [49]. The density in both modules is calculated based on the molar volume obtained from the Peng-Robinson EoS, however, the calculation of the density is slightly different which would explain the slight difference in results. We must note that these are just slight deviations.

7.2. Reservoir Model

In this section, the description of the two 2D reservoir models used for investigation of gas behaviour are provided.

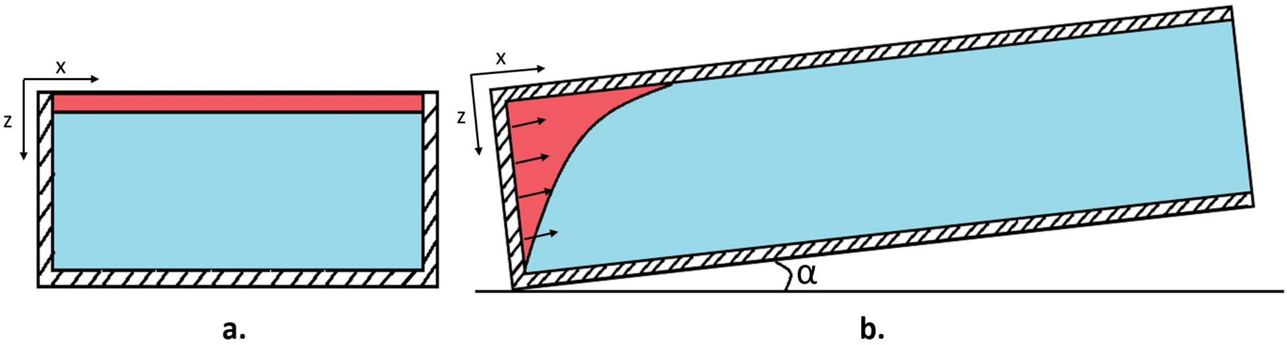

Figure 7.10: Visual overview of the two dimensional reservoir models used for simulation.

A horizontal reservoir where gas is placed on top of the reservoir is used to investigate the pure convective behaviour within the system. This model shown in 7.10a is bounded with three no-flow boundaries and constant pressure right boundary. The specific dimensions of this model can be found in table 7.1a.

A large scale model of an inclined reservoir is used to model gas injection and post-injection migration of a gas plume. In this model, the gas will be injected at the left boundary as shown in figure 7.10b. The highest point of the reservoir is 100 meters higher than the lowest point which causes a hydrostatic pressure difference of roughly 10 bar along the reservoir initially. The specific dimensions of the reservoir model can be found in table 7.1b. The properties of both reservoirs are identical and are given in table 7.2. All these inputs are kept constant over all simulation results except when stated otherwise.

Model A	Value	unit
top depth left boundary	1000	m
top depth right boundary	1000	m
x length	100	m
z length	50	m
inclination	0	°
dx	1	m
dz	1	m

Model B	Value	unit
top depth left boundary	1100	m
top depth right boundary	1000	m
x length	1000	m
z length	50	m
inclination	5.74	°
dx	10	m
dz	1	m

Table 7.1: Dimensions Reservoir models

Parameter	value	unit
Perm x	100	mD
Perm z	10	mD
m NaCl	0	mol/kg
Temp	100	$^\circ C$
Diffusion coeff.	2.5 e-5	m^2/day
OBL resolution	101	-
min P	1	bar
max P	300	bar
S_{wc}	0.2	[-]
S_{gr}	0.2	[-]
c_r	10^{-5}	[-]
Δt	100	days
Inj. Rate	30	m^3/s
porosity	0.3	[-]
R	83.144598	$[cm^3 barK^-1]$

Table 7.2: inputs for the reservoir model

7.3. Convective mixing

In this section, an investigation is made for the convective mixing within a reservoir.

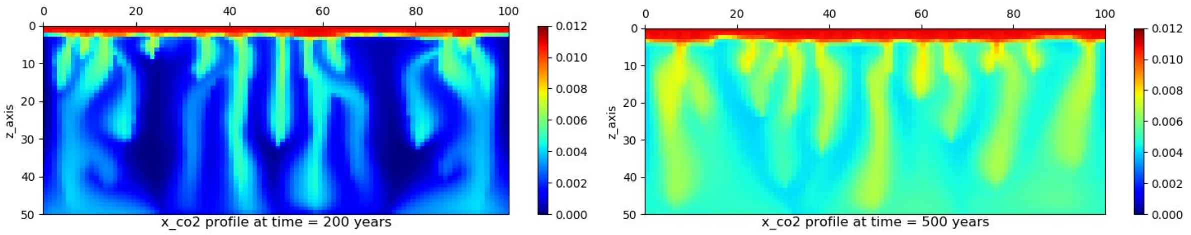

(a) CO_2 dissolution profile at 200 years

(b) CO_2 dissolution profile at 500 years

Figure 7.11: Results of convective behaviour of gas plume, shown by the dissolved CO_2 profile (x_{CO_2}). Here gas plume consists of multiple components with initial composition of [0.8, 0.09, 0.09]. Modeled using a Time-Step of 10 days and a Diffusion coefficient of 2.5e-9 m^2/day

For the investigation, reservoir model A was used as shown in figure 7.10a. Since the top boundary of this model has an infinite volume, the composition and pressure at the top of the reservoir will remain constant. In figures 7.11, the dissolution profile of CO_2 is plotted for 200 and 500 years. The gas plume placed in the top layer of the reservoir has a composition that is similar of that used in the other gas mixture models, CO_2, N_2, CH_4 [0.8, 0.09, 0.09].

In the results of figures 7.11a and 7.11b, the columns (fingers) of dissolved CO_2 are formed and migrating towards the bottom of the reservoir. In figure 7.11b these fingers will increase in size and migrated further as more CO_2 has dissolved in the resident water. With a longer time period more dissolved CO_2 has spread throughout the reservoir as less areas with no dissolved CO_2 are visible.

As the reservoir model A has similar dimensions as one of the models used in the benchmark paper by Elenius et al. [18], a comparison can be made. However, since Elenius et al. [18] uses a fully CO_2 saturated aqueous solution as initially placed cells (at the top boundary) instead of placing a gas mixture in the gas phase, a perfect comparison is not feasible. From comparison with [18] it is found that the convective behaviour is similar.

7.4. Gas Injection Results

In this section, the results of pure CO_2 and the gas mixture injection into reservoir B are presented. These results are simulated for an injection time of 5 years with a constant volumetric injection rate of 30 m^3/day. For the generation of these results, a time-step of 10 days was used combined with a large maximum of non-linear iterations. It is important to note that the results presented here for post-injection gas propagation are used then as an input for the long-term plum migration simulation.

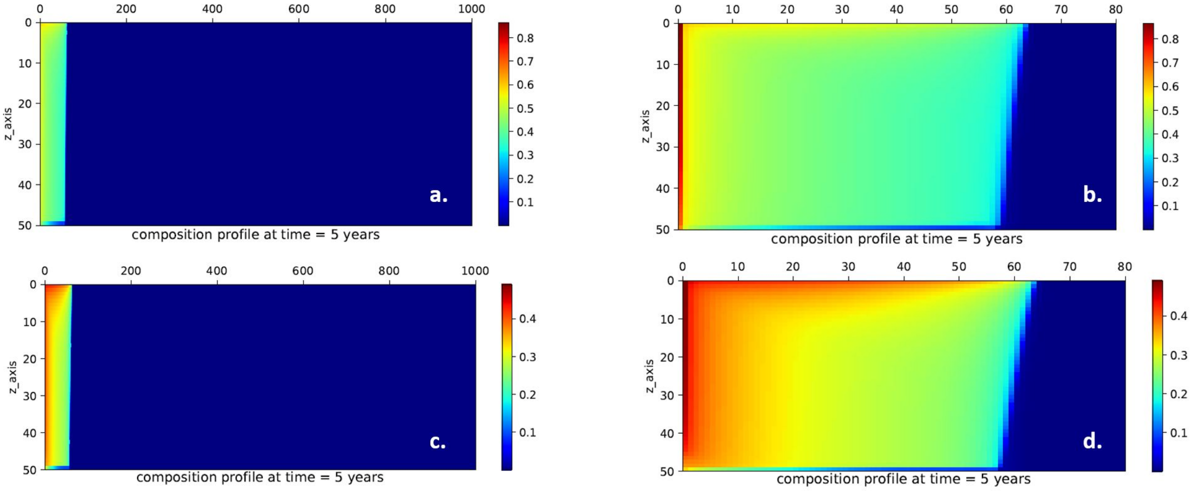

Figure 7.12: Resulting CO_2 composition profiles of gas injection for pure CO_2 (a,b) and impure gas stream (c,d). Note that figures b and d are zoomed in versions of figures a and c. Injection composition of the gas mixture is CO_2, N_2, CH_4, z=[0.8, 0.09, 0.09].

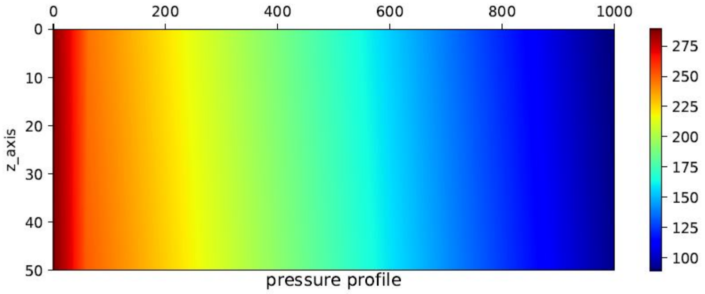

Figure 7.13: Resulting pressure profile of gas injection for pure CO_2 and impure gas stream.

In figures 7.12a,b and figures 7.12d,c, the results of CO_2 compositional profile related to gas injection for pure and impure mixture of CO_2 are shown respectively. The pressure profile related to injection is near identical for both pure and impure gas stream of CO_2 and is shown in figure 7.13. In comparison of the compositional profiles, however, more significant differences can be observed. The difference in CO_2 concentration between the cells bounding the injection well and the rest of the gas plume is much higher for pure CO_2 injection.

In figures 7.14a,b and figures 7.14d,c, the results of gas saturation and dissolution of CO_2 profiles related to gas injection for a pure and impure mixture of a CO_2 are shown respectively. An interesting observation that can be made from the gas saturation profile for pure CO_2 injection is that in the cells bounding the injection well (the left boundary), the water saturation has a value below the residual water saturation (0.2) due to the water vaporization. However, in the case of impurities, this does not happen.

The most important observation that can be made from the dissolution profiles, is that the concentration of dissolved CO_2 is much higher than we will find in the post-injection results due to the higher pressure during injection. Another important observation here is that the dissolution of CO_2 is lower at the front of the gas plume relative to the back for impure gas mixture injection. Impure components affect the dissolution of CO_2 and are migrated to the front of the gas plume due to chromatographic separation. This effect will be investigated

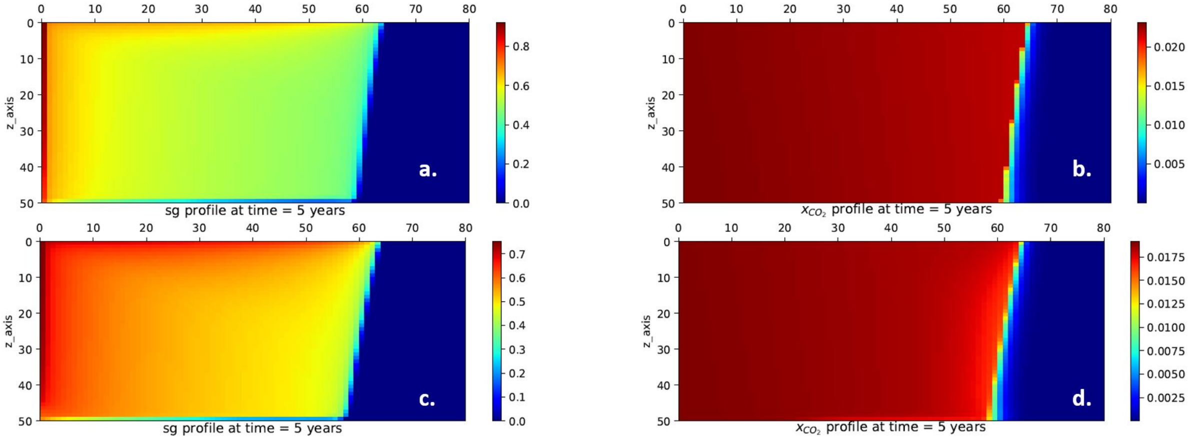

Figure 7.14: Resulting gas saturation and CO_2 dissolution profiles for gas injection of pure CO_2 and gas mixture. Note that all these figure are zoomed in simimlar to figure 7.12b, d. Injection composition of the gas mixture is [0.8, 0.09, 0.09].

further in section 7.6.

7.5. Post-Injection Plume Migration Results

In this section, the results of the post-injection migration of the CO_2 gas plume will be investigated for pure gravity conditions and for the model including diffusion. Comparisons will be made to earlier works by Elenius et al. [18] to observe how the implementation of a more accurate Equation of State affects the results. Please note that for all post-injection migration results the gas injection of 5 years with an injection rate of 30 m^3/day is used as input. Furthermore, a time-step of 50 days is used to simulate the post-injection results. The composition of injected pure CO_2 is, z=[0.99], and the composition of the gas mixture is always CO_2, N_2, CH_4, z=[0.8, 0.09, 0.09].

7.5.1. CO_2 plume migration for buoyancy dominated regime

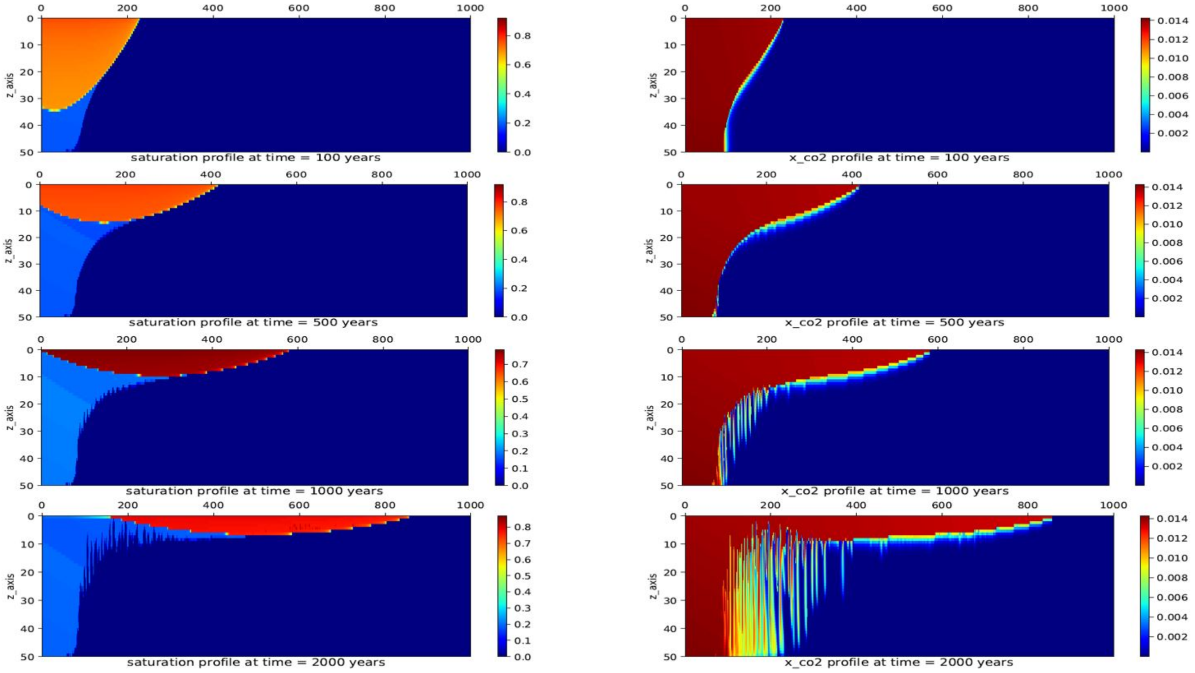

Figure 7.15: Results of plume migration shown by gas saturation (on the left) and dissolved CO_2 (on the right) profile without accounting for diffusion and capillarity over a range of time periods after injection. Here only pure CO_2 is injected.

In figures 7.15 the results of the post-injection migration of pure CO_2 saturation and dissolution profiles of CO_2 are shown. These profiles are shown for varying periods up to 2000 years. In the figures describing the gas saturation profiles, a clear distinction can be made between the gas plume and the residual trapped CO_2 left in the trail of the moving gas plume. The gas plume behaves as expected by migrating towards the top of the reservoir since it is less dense than the resident brine. In the early periods of 100 and 500 years after injection, we find that gas saturation in the grid-cells along the injection well location (left boundary) exceeds the maximum gas saturation of 0.8[-]. In figures 7.16 this anomaly can be seen in more detail. This anomaly can be addressed to the fact that the injected CO_2 evaporates the aqueous components which is migrated with the gas. At 2000 years after injection, some instabilities can be witnessed inside the gas plume where a few grid-cells will exceed the maximum gas saturation of 0.8 again. This anomaly is harder to justify and is most probably caused by an instability in the model.

In the figures describing the dissolution of CO_2, it is clear to see that everywhere where the gas plume has been, CO_2 has been dissolved to full saturation. At 1000 years after injection, the first fingers start to become clearly visible as they move downwards away from the gas plume and the residually trapped gas. This is the onset of the convective mixing that occurs due to the fact that brine density increases when CO_2 is dissolved in it. At 2000 years after injection the residually trapped gas on top of the reservoir, in the trail of the gas plume, will

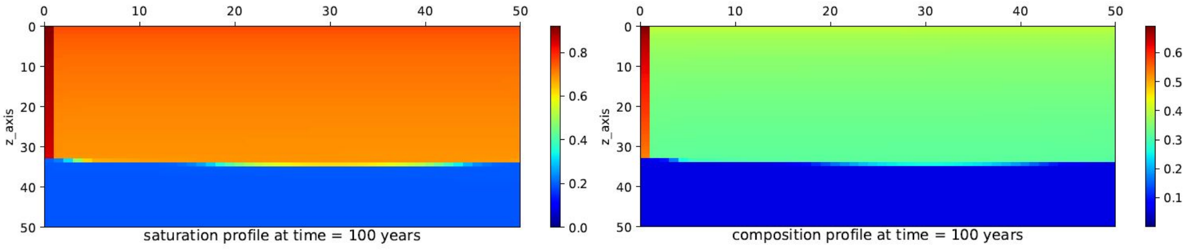

(a) Saturation profile

(b) Compositional profile

Figure 7.16: A close up of the saturation and composition profile of CO_2 at 100 years after injection. Here cells bounding injection exceed gas saturation limit of 0.8 [-].

start to disappear. Here nearly all residually trapped gas has been dissolved into the brine and due to convection has moved to the bottom of the reservoir. Convection on the left side of the reservoir does not occur because here the brine is fully saturated with CO_2 from bottom to top.

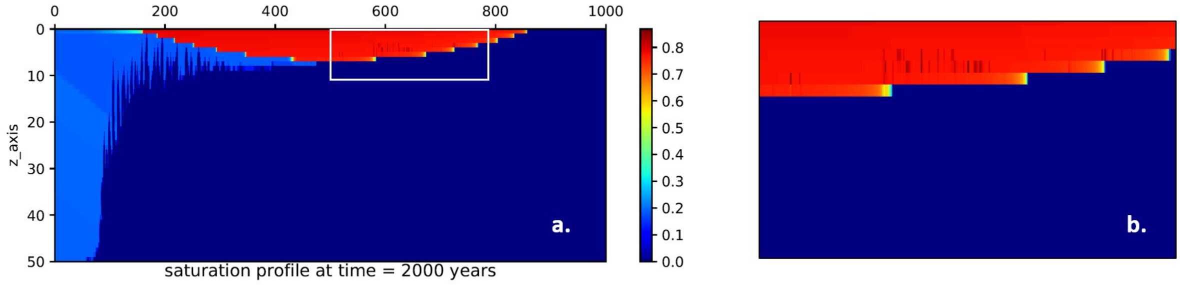

Figure 7.17: Figure (a) shows the gas saturation profile at 2000 years after injection and figure (b) gives a detailed, zoomed in, presentation of the unphysical gridcells.

7.5.2. CO_2 plume migration for full physics

In figure 7.18 the gas saturation and CO_2 dissolution profile for post-injection migration of pure CO_2 are presented. In these simulation results, the model accounts for gravity, diffusion and capillarity physics. From these results, a few important observations can be made in comparison with the result neglecting diffusion and capillarity. The main differences that can be observed are found in the convection behaviour, the gas-liquid interface, and the plume migration.

The difference in convective behaviour is most distinct at the late time period of 2000 years after injection. The number of fingers that are formed and the amount of dissolved CO_2 is substantially more than in the results neglecting diffusion and capillarity. Another clearly visible difference is that the interface between the liquid and the gaseous plume is more smoothed when the model accounts for capillarity. This smoothed interface is the result of accounting for capillary pressure in the model, as a capillary transition zone (CTZ) is formed.

The last observation is the difference in distance the plume migrates. In the result accounting for diffusion and capillarity, the plume propagation is reduced significantly. The reduction in plume propagation can be caused by two effects related to increased dissolution. One of these effects is that increased dissolution causes an uneven surface to form in the area with residual trapped CO_2, eventually causing the tip speed of the plume to reduce [18]. In the findings of MacMinn et al. [39] it is discussed that if dissolution was neglected the tip of the plume would travel with constant speed through the reservoir. The other effect of reduction of the plume propagation is that convection dissolution can have a negative effect on the slope migration of a buoyant plume. This effect was proven by MacMillan et al. using laboratory analog experiments on miscible CO_2 [40]. Since more dissolution takes place when including the effect of diffusion, the plumes speed will decrease, which explains why

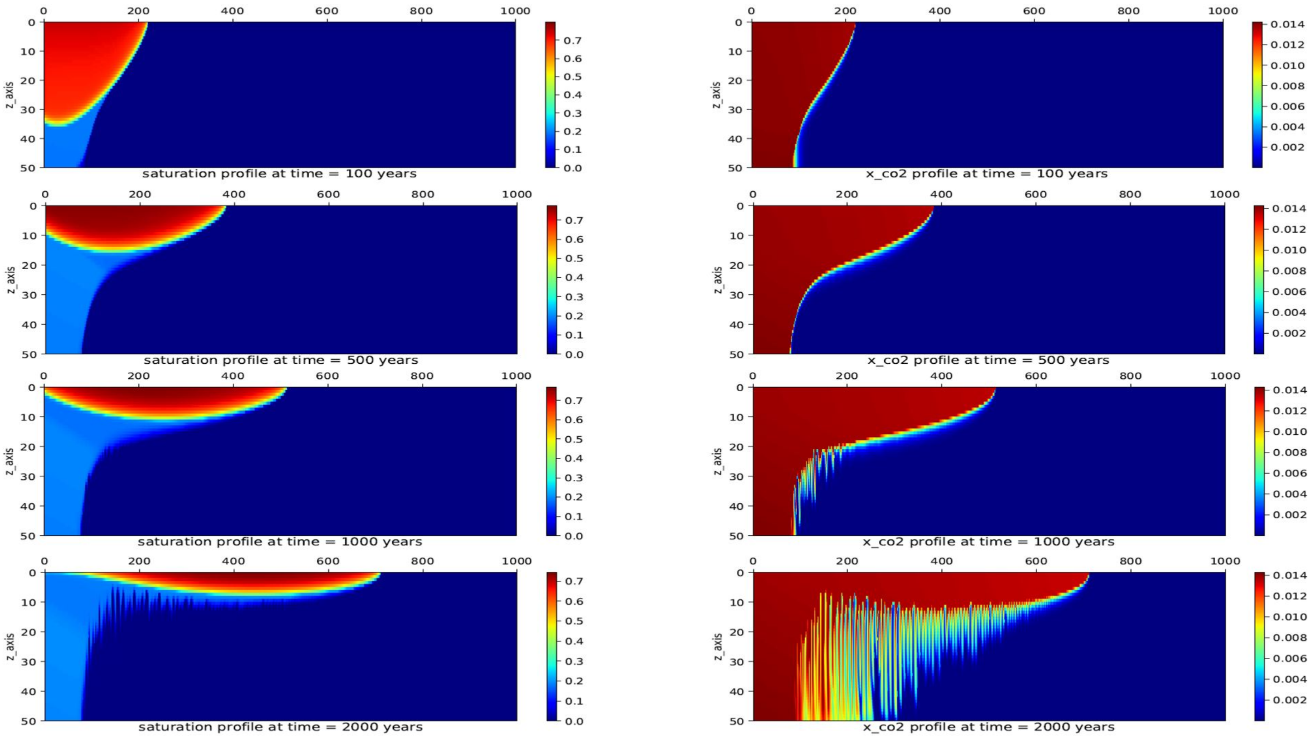

Figure 7.18: Results of plume migration shown by gas saturation (on the left) and dissolved CO_2 (on the right) profile accounting for gravity, diffusion and capillarity over a range of time periods after injection. Here only pure CO_2 is injected.

the plume propagates less far when accounting for diffusion.

For the situation of pure CO_2 plume migration including diffusion and capillarity, a comparison can be made with the findings of Elenius et al. [18], who made similar assumptions. One of the main differences between these models is that in our model, the thermodynamic equilibrium is solved using a cubic EoS together with an activity model, whilst a constant k-values were used in Elenius et al. [18] for phase equilibrium calculations. Another difference is that phase properties in this paper are calculated using realistic correlations dependent on pressure, temperature and salinity whilst constant phase properties with linear dissolution model were used in Elenius et al. [18].

In comparison of the results with Elenius et al. we find a few distinct differences in the saturation profile, dissolved CO_2 profile and lastly the plumes migration. The main difference in the saturation profile is in the trail of the gas plume. 2000 years after injection we find that the residual trapped gas gradually disappears as it dissolves into water and sinks to the bottom of the reservoir. This different in dissolution rate of the residually trapped gas could be addressed to the difference of thermodynamic models.

In the dissolved CO_2 profiles we find similar fingering anomalies as found in Elenius et al. [18]. The main difference comes from the fact that in our results, fingering is mostly limited to the areas halfway and behind the gas plume. The reason for this is most likely due to the difference in plume speed and resolution of the model. As is seems that in our model, the plume migrates further (and faster) it is logical that dissolution at the front of the gas plume is not as pronounced as when it travels slower. An explanation for the increased plume speed in regard of the result of Elenius et al. [18] can come from the phase properties used. In [18] the gas phase is assumed to have a constant density that is equal to that of a supercritical gas at 733 kg/m^3. At the reservoir conditions used for the simulations in this paper a gas density is obtained of roughly 175 kg/m^3, see figure C.8. A light gas will increase the effect of buoyancy and therefore increase the plume propagation speed.

7.5.3. Plume with impurities for buoyancy dominated regime

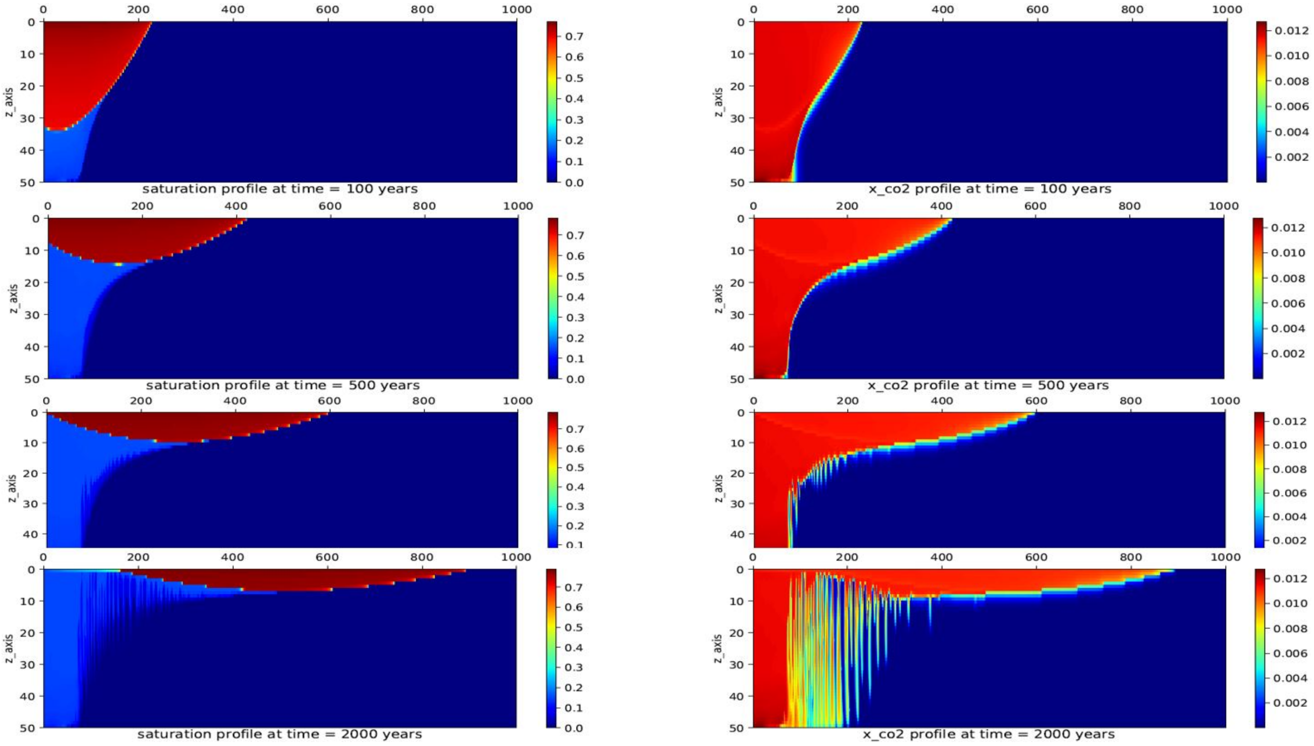

Figure 7.19: Results of plume migration shown by the gas saturation and dissolved CO_2 profile for a range of periods after injection. Here impure mixture has composition [CO_2, N2, CH4], z=[0.8, 0.09, 0.09].

Figure 7.19 shows the results of the post-injection migration of an impure gas stream. Comparing these results with those found for pure CO_2 migration in figure 7.15 a few interesting differences can be observed. The first most visible difference is the negative effect impurities have on the dissolution of CO_2. Here dissolution of CO_2 only reaches an average value of around 0.011 [-], while in the case of pure CO_2 gas plume the aqueous phase will be fully saturated with CO_2, ≈ 0.014 [-]. This negative effect due to the presence of impurities on CO_2 dissolution coincides with the validations made with literature for the thermodynamic model in figure 7.5. A higher effect of impurities on CO_2 dissolution is observed inside the gas plume compared to the residual gas trail as here, the concentration of impurities is at its highest since both impurities barely dissolve in the aqueous solution. The lower solubility of the impure components was found during the validation of the thermodynamic model in figures C.1 and C.2.

The second difference between the results of pure and impure gas plume migration is the propagation of the gas plume. Although not clearly visible, the plume with impurities will migrate slightly further than the plume with pure CO_2. An explanation for the further propagation of the gas plume can be found in the fact that less CO_2 dissolves due to the presence of impurities. How the amount of CO_2 dissolution affects the plume migration has been explained extensively in the previous subsection.

7.5.4. Plume with impurities for full physics

In figures 7.20 the results of the post-injection migration of an impure CO_2 gas mixture are presented. These results include additional physics of diffusion and capillarity and are simulated for various time periods up to 2000 years after injection. In these results, the model is fully physical for the scenario where CO_2 with impurities is injected. Very similar conclusion can be derived here as in pure CO_2 comparisons.

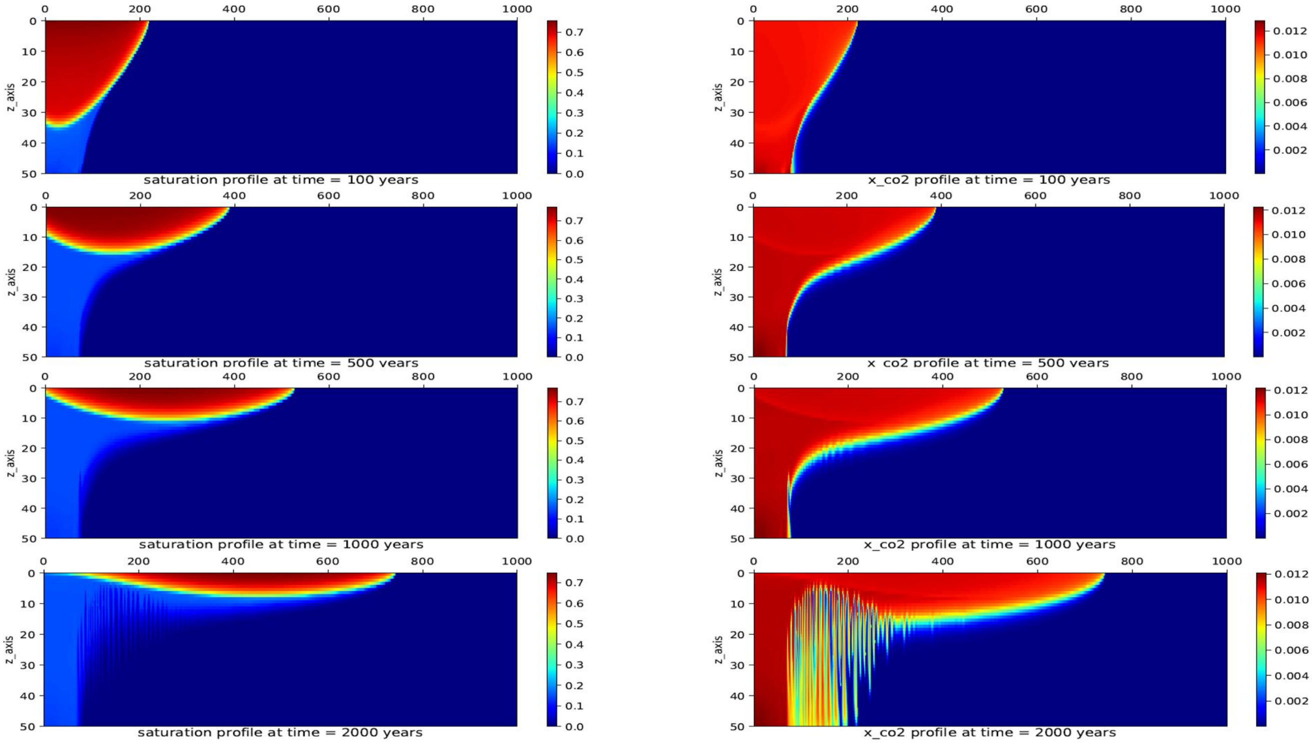

Figure 7.20: Results of plume migration accounting for gravity, diffusion and capillarity up to 2000 years after injection. Here impure gas mixture of [CO2, N2, CH4], with composition [0.8, 0.09, 0.09] is injected.

7.6. Behaviour of impure components

In this section the behaviour of the impure components in the injection CO_2 gas stream are analysed. In figure 7.21, the overall compositional (z), liquid mole fraction (x) and gaseous

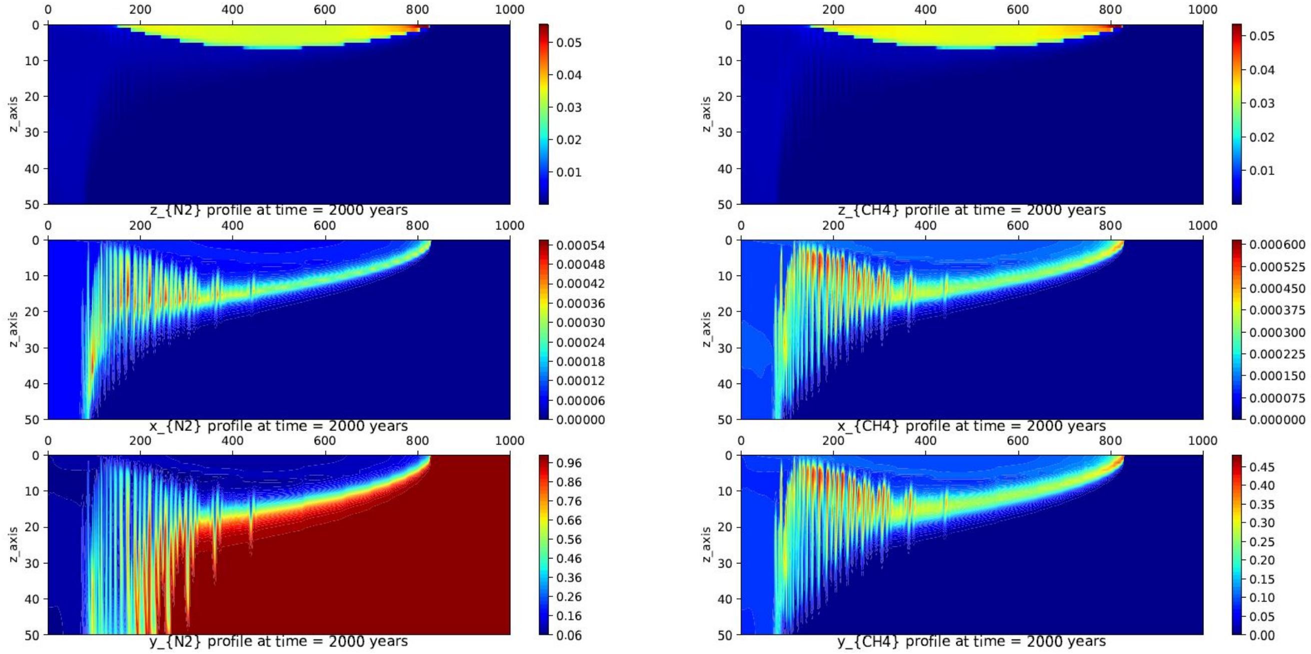

Figure 7.21: Results of the behaviour of impurities N_2 and CH_4, accounting for gravity and Diffusion at 2000 years after injection. Here impure mixture is [CO2, N2, CH4], [0.8, 0.09, 0.09].

mole fraction (y) profiles of impure components N_2 and CH_4 are presented. From the overall composition profile of both impurities, it can be observed that the highest concentration of these component is present at the leading tip of the gas plume. Note that this phenomenon was also observed at the injection results with a multi-component gas mixure, as the dissolution at the leading tip of the gas plume is lower due to the increased presence of impurities.

The tendency of the impure components to concentrate at the leading tip of the gas plume can be explained by the significant difference in solubility with CO_2. As explained in chapter 3, the physics regarding flow of the components through the reservoir are approached using operators that are component specific. The flow of each component is dependant on the compositional characteristics and chromatographic separation is expected [52].

When including capillarity to the model, the effect of increased concentration at the tip of the leading gas plume is no longer visible, see figure 7.22. The addition of capillarity will visually smooth the distribution of component compositions, but it will not take undo the the above mentioned physical behaviour completely.

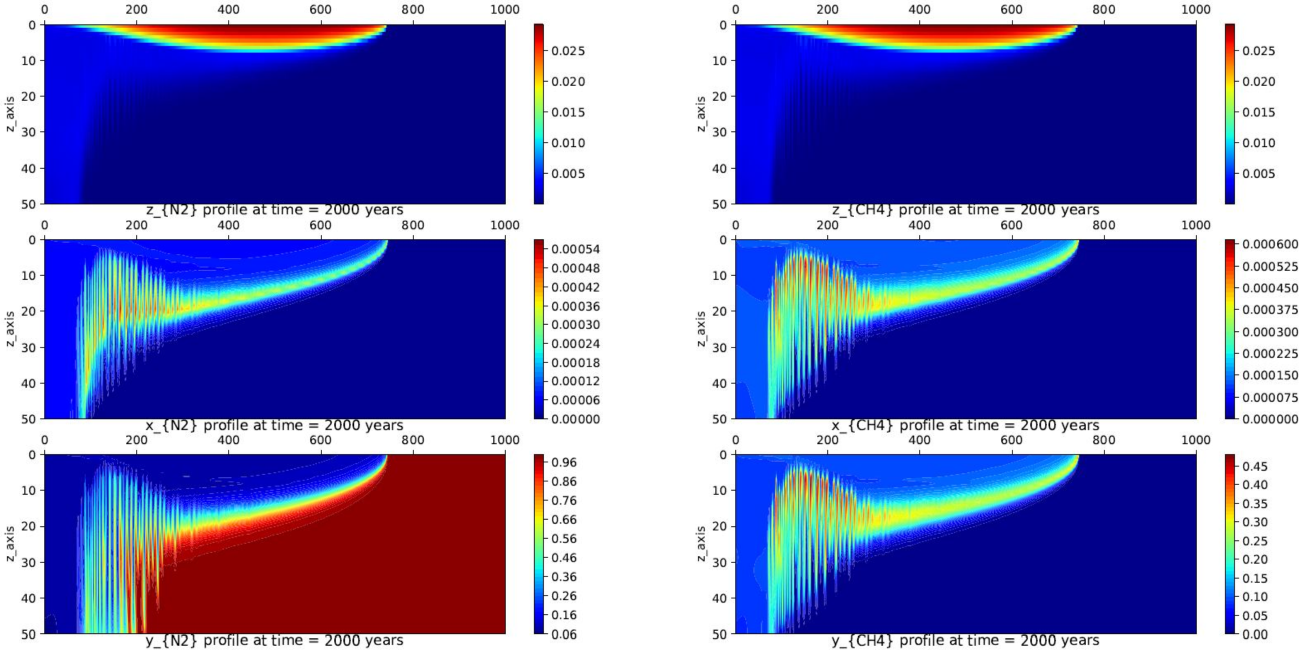

Figure 7.22: Results of the behaviour of impurities N_2 and CH_4, accounting for gravity, diffusion and Capillarity at 2000 years after injection, with 5 years of gas injection as input. Here impure mixture [CO2, N2, CH4], [0.8, 0.09, 0.09] is injected into an aquifer with 0 molal NaCl salinity

7.7. Process power consumption

In this section, the results are shown of the basic analysis of the power consumption build in chapter 6. Here the input parameters for the power consumption model can be found in table 7.3. The parameters selected for natural gas (NG) emission factor and powerplant efficiency were obtained from Eftekhari et al. [17]. The same parameters for coal fired powerplants were obtained from H.H.J. Vreuls [28]. The length of the transportation pipeline as well as the wellbore length were also taken as similar values to Eftekhari et al. [17] so allow comparison of the results. The gas densities at surface and supercritical conditions were taken as rough estimates from figure 7.9.

7.7.1. Natural Gas fired powerplant and post-combustion MEA separation

The results of the cumulative power consumption and power consumption of compressor B for a natural-gas-fired powerplant are presented in figures 7.23a and 7.23b respectfully. As the compression power necessary for compressor B is the only dynamic variable, its behaviour

Parameter	value	unit
η_{pump}	0.7	[-]
L_{pipe}	150	km
$L_{wellbore}$	1	km
$Em_{factor,NG}$	0.055	kg CO_2/MJ
$Em_{factor,coal}$	0.090	kg CO_2/MJ
$\eta_{pp,NG}$	0.45	[-]
$\eta_{pp,coal}$	0.38	[-]
purification cost MEA	3.5	MJ/kg CO_2
ρ_{gas}	20	kg/m^3
$\rho_{gas,sc}$	800	kg/m^3
$(\Delta P/km)_{pipe}$	0.25	bar/km
P_1	1	bar
P_3	80	bar

Table 7.3: Inputs for power consumption model. (Here subscript sc implies super-critical conditions.)

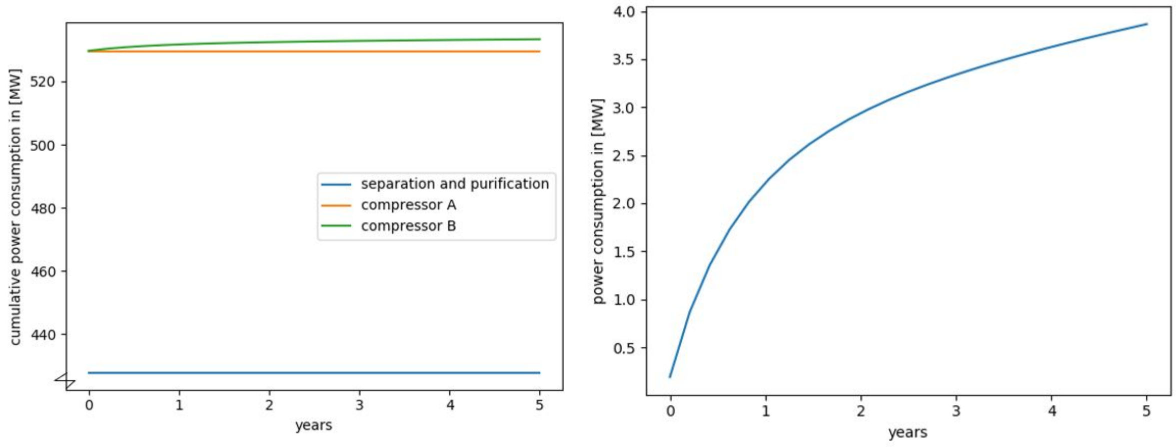

(a) cumulative power consumption

(b) power consumption compressor B

Figure 7.23: Results of power consumption (in [MW]) of the CCS process chain using natural gas fired power-plant and MEA separation.

with time is shown separately. As expected, the power consumption needed for compressor B increases with time as the pressure needed to maintain a constant flow-rate increases.

The most important observation that should be made from these results is that the majority (roughly 430 bar) of the total power consumption results from capture and purification processes. It must be noted that the average energy penalty used for MEA separation (3.5 MJ/kg CO_2) is at the low end of the suggested energy penalties by Eftekhari et al. [17], who suggests an energy consumption range of 3-7 MJ/kg CO_2. Furthermore, costs for injection and sequestration are found to be around roughly 105 bar. Both for purification, transport and injection power consumption, the results are reasonably similar to the predictions made by Eftekhari et al. [17]. Since the calculation and assumptions in [17] are slightly different, a perfect comparison cannot be made. In conclusion, for a NG fired powerplant using post-combustion MEA separation of CO_2 that produced 1000 MW of power, roughly 535 MW of the generated 1000 MW are needed to separate and store CO_2 from the emission stream.

As explained in chapter 6, the mass flow-rate used in injection simulation is equal to the emission rate, for NG fired powerplant this is 122 kg CO_2/s. Since the injection model is limited by 2-dimensions, the mass flow-rate used in the model is adjusted resulting in a volumetric flow-rate of roughly 36 m^3/day.

7.7.2. Coal fired powerplant and post-combustion MEA separation

For the determination of the power consumption of a 1000 MW coal fired powerplant simulation has to be performed for an injection rate equal to the emission rate. The emission rate is estimated at 236 kg CO_2/s, which in the 2-dimensional space is equal to roughly a volumetric flow-rate of 71 m^3/day. Regretfully, maintaining an injection rate of 71 m^3/day for 5 years in the developed injection model will lead to pressures that exceed the maximum pressure limit of 350 bar. Furthermore, high injection rates will lead to increased nonlinearity of the simulation and unphysical results due to non-converged solution. Therefore, the injection simulation was only performed for a duration of half a year. This compromise shows the limitations of using high constant injection rates in the injection model developed.

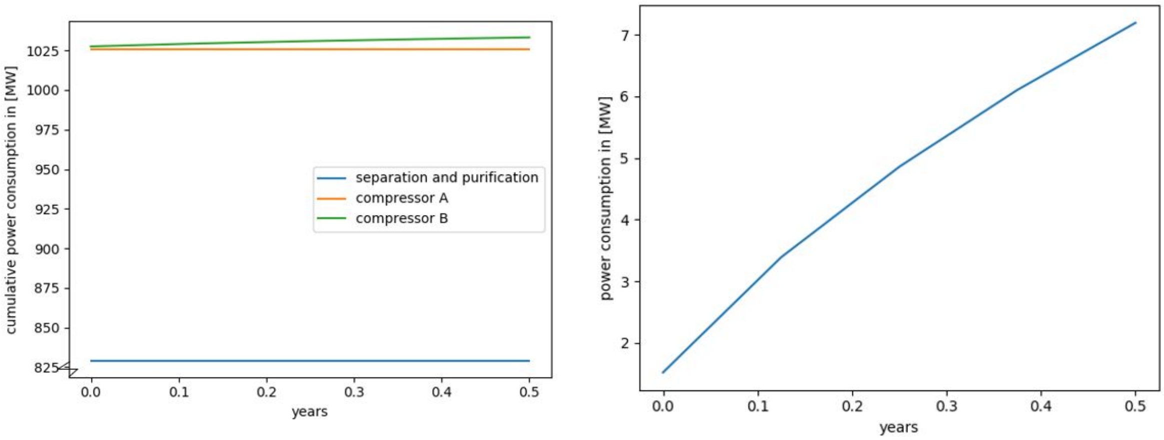

(a) cumulative power consumption

(b) power consumption compressor B

Figure 7.24: Results of power consumption CCS process chain using coal gas fired power-plant and MEA separation.

Nevertheless, the power consumption of the separation-purification and transport stages can be calculated as they are independent on the pressure changes in the reservoir. The power consumption of the separation and purification stage is calculated at roughly 825 MW, while the power consumption of compressor A is roughly 200 MW. This concludes that a 1000 MW coal fired powerplant using post-combustion MEA CO_2 purification uses roughly 1025 MW for purification, transport and injection. Evidently, this is a very interesting result as it is presented here that it would cost more power to capture, purify, transport and inject CO_2 than the power that is produced by the powerplant.

As the majority of the power consumption is the result of capture and separation (825 MW), the power consumption in this part was revised. The assumptions made for the efficiency of a coal power plant ($\eta_{pp,coal}$ = 0.38) and an emission factor (Em_{factor} = 0.090) are both reasonable assumptions as they are found in literature H.H.J. Vreuls [28]. The last parameter which could be suspected is the energy penalty of MEA separation which was obtained from Eftekhari et al. [17]. Although the estimated MEA separation energy costs found by Eftekhari et al. [17] are in regard of natarual gas powerplant, from the investigation in chapter 2 we know that the MEA separation procedure is a post-combustion process that can also be applied on coal fired powerplants. Seeing as we take 3.5 MJ/kg CO_2 at the low-end of the suggest range of 3-7 MJ/kg CO_2, this also does not seem like an unrealistic assumption.

To conclude, using a simplified framework with reasonable parameter to asses the power consumption of a coal fired powerplant, we find exceptionally high power costs.

8

Discussion

The choice for the composition of the gas mixture was chosen as these components were deemed most probable present in an emission stream. A gas mixture including hydrogen sulfide is also possible, however, due to time constraints has not been simulated for the large scale reservoirs. In chapter 2, additional impure components were found in the emission gas streams such as SO_2, H_2, O_2. Again due to time constraints these components were not added to the model, however, if all the component specific properties were obtained (most importantly the binary interaction parameters) it could be easily implemented into the thermodynamic model.

From the comparisons made between the results of the implemented thermodynamic model and the literature, we know that deviations between the two are very small. The only noticeable and worrisome result obtained from the thermodynamic model were produced for hydrogen sulfide, shown in figure 7.4. This erroneous results were further investigated by running the results for two different Peng-Robinson Equation of State (PR EoS) implementations but the erroneous results for H_2S are still present. We address them to the limitations of PR EoS for modeling of non-hydrocarbon mixtures. It must also be noted that the validation was made for a mixture including H_2S does fit literature nicely (shown in figure 7.3).

With the implementation of the thermodynamic model, several simplified assumptions were made. In the determination of the activity coefficient, the anion and cation concentrations were used. In this model, we assumed that the anion and cation concentration are only dependant on the NaCl concentration and not on other aqueous brine components. In reality, chemical reactions with the gas components may induce a formation of other cations and anions which will have an effect on their concentration and so also on the activity coefficient.

From the validation of the phase properties, we find that the determined phase properties fit literature generally well. To determine these phase properties, existing correlations from literature were used. For the aqueous phase, the density assumed to be only dependant on the mass weight and concentration of dissolved CO_2. The effect of impurities in this relation is only taken into account indirectly by the effect they have on the dissolution of CO_2. It can be argued that in gas mixture compositions for CO_2 injection, CO_2 is the heaviest and most dominant component present. So that the effect of impurities on the overall aqueous phase density would be limited.

The use of a constant gaseous phase viscosity will also have an effect on the simulated results. It can be argued that the effect is limited as viscosity of the gaseous phase is primarily sensitive to temperature changes compared to pressure changes. Since we are modeling an isothermal system, a good estimate of the gaseous viscosity would limit the deviation from real mixtures. The gas viscosity used in this model (15 cp) is quite high. At the reservoir conditions used in this paper, a gas viscosity of around 6 cp would be more realistic [49]. However, we chose to use a viscosity of 15 as to be comparable to the benchmark study in Elenius et al. [18].

In this model, the physics of diffusion was implemented using Fick's Law. For the diffusion coefficient, we used a value identical to one used by Elenius et al. [18]. It must be noted that Fick's Law of diffusion is only valid for binary components or for multi-components in assumption of infinite dilution. In our model for gas mixtures, the assumption of infinite dilution is not valid which results in the fact that the implementation of Fick's Law for a multiple component system is not accurate. For an accurate implementation of diffusion in a multi-component system, the generalized Maxwell-Stephan equation must be implemented with as many diffusion coefficients as there are pairs of components in the system. Due to time constraints, this relation has not been investigated further and has not been implemented. A major challenge for the implementation of this relation will be the determination of all the diffusion coefficients for all components. An accurate relation determining these must be found as the diffusion coefficients are also dependant on the pressure, temperature and salinity of the solution.

One of the deviations of this model results from reality lies in the fact that chemical reactions have not been taken into account. Assumption of no chemical reactions neglects the formation of cations and anions in the model which can affect the accuracy of property evaluation. These anions cations and anions are used to determine the activity coefficient and thus will eventually have an effect on the behaviour of the components in the aqueous phase. Another effect of neglecting chemical reactions is that the precipitation and dissolution of minerals due to phase behavior and CO_2 dissolution is ignored. In reality, the precipitation of salts can have an effect on the absolute permeability of rock which reduce injectivity and may lead to the pressure build-up in the vicinity of the well.

In chapter 6, a very basic framework is made to investigate the power consumption of the CCS process chain. It is important to note that this framework only gives a rough estimation of the total power consumption as a lot of simplifying assumptions have been made. The parameter that has the biggest effect on the total power consumption is the estimated energy penalty of the capture and separation techniques obtained from Eftekhari et al. [17]. As this parameter has the highest contribution to the total power consumption, it should be investigated in more detail.

One of the main objectives for the implementation of this energy process framework was to investigate the physics of injection has on the power consumption of the whole process chain. To a certain extent, this has been successful. However, the use of a 2D model to simulate injection does have significant limitations. One of these limitations is an estimate/conversion of the injection rate in the two-dimensional domain used in the model. For a realistic investigation of the total power consumption in the process chain, an appropriate transition from a 3D geometry should be performed.

9

Conclusion

In this research project, an extensive investigation was performed into the behaviour of pure CO_2 and impure gas mixtures in subsurface reservoirs. In the literature study presented in chapter 2, a description of various capturing and separation techniques with related impurities are presented. From this investigation, the most common impurity components found were chosen to be implemented into the thermodynamic model (N_2, CH_4 and H_2).

To predict the behaviour of an impure gas mixture at reservoir conditions in the practical range of P, T and salinity, an accurate thermodynamic model was implemented into the Delft Advanced Research Terra Simulator (DARTS). After extensive validation of the model results vs. results available in the literature, it can be concluded that the dissolution model was implemented successfully. Additionally, various correlations for phase properties were implemented into the model which were also validated against the literature.

The implementation of the thermodynamic model and phase property correlations were eventually used in the injection and post-injection migration models. The simulations of plume injection and migration in a large scale inclined reservoir have been run to investigate the effect of impurities on plume migration. The impurities have a negative effect on the dissolution of CO_2, leading to further propagation of the gas plume. This further propagation leads to an increased chance of leakage and so decreases CO_2 storage security. In comparison of the fully physical results for pure CO_2 injection with Elenius et al. [18], two important findings were made. The first finding is related to an accurate phase property evaluations implemented in our model. A lighter gas density was predicted in the simulation due to the full coupling of injection and post-injection period. This resulted in a higher plume velocity compared with Elenius et al. [18]. The second important finding is related to the residually trapped gas which dissolves faster with in the accurate thermodynamic model compared to results in Elenius et al. [18] where constant k-values have been used.

Furthermore, the simulation results of post-injection gas mixture migration shows that impurities concentrate at the leading tip of the gas plume. This effect can be addressed to the low solubility of these impure components and chromatographic separation due to different characteristic velocities of components.

Finally, a basic process energy framework was implemented to asses the power consumption over the whole CCS process chain. From this investigation it is shown that the physics of injection have a limited effect on the total power consumption of the process. The most significant power consumption are related to the capture and separation costs.

10

Recommendations and Future Work

As the work performed in this MSc thesis is limited to time constraints, not all ideas have been fulfilled. For future works I would recommend further investigation of the following subjects.

As has been addressed in the discussion, not all impurities found in the carbon capture and purification technique are implemented in the thermodynamic model. To make this thermodynamic model more complete for future use to simulate realistic CCS streams, these components must be added. Specifically, it would be interesting to test the effects of SO_2 which is increasing the dissolution according to [59]. Furthermore, the implemented thermodynamic model operates for varying salinity's up to 6 molal NaCl. Due to time constraints, the effects of salinity changes have not been investigated thoroughly. From literature, we know that increased salinity leads to decreased CO_2 dissolution.

It is highly suggested that before further use of the implemented model an extensive sensitivity study is performed. To make the developed model more accurate, chemical reactions (both equilibrium and kinetics) should be added. With the addition of chemical reactions, the addition CO_2 storage process of mineralization can be included as this is the most secure form of CO_2 storage. Additional benefits of adding chemical reactions would be a more accurate determination of anions and cations for the activity model and possible precipitation of salts in the near-wellbore area.

For an accurate use of diffusion in multi-component systems, further work must be done to implement the Maxwell-Stephan relation. The implementation of this relation is not a trivial task as the number of diffusion coefficients that need to be determined is equal to the pairs of components. Furthermore, the diffusion coefficients are dependant on temperature, pressure and salinity.

The most recommended future research suggestion is to benchmark the model against existing CO_2 sequestration pilots to check the real accuracy of the models predictions. After the model has been bench marked, it might be very interesting to investigate different injection strategies that could decrease plume propagation and therefore increase storage security.

A

Appendix chapter 4 - thermodynamic model

A.1. Derivation of Fugacity-Activity equilibrium definition

As discussed previously, the system is assumed to be in an instantaneous thermodynamic equilibrium which means that the chemical potential of each phase are equal to each other. To define this equilibrium first the definition of the chemical potential of the gas phase is defined as:

$$\mu^g(T,P) = \mu_g^0(T,P) + RT\ln(f). \tag{A.1}$$

Where μ is the chemical potential and μ^0 is the chemical potential at reference temperature. f is fugacity which is equal to:

$$f = P\Phi y, \tag{A.2}$$

where Φ is the fugacity coefficient and y the mole fraction in the vapor phase. The chemical potential of the liquid or aqueous phase can be defined in terms of activity a instead of fugacity as follows:

$$\mu^l(T,P) = \mu_l^0(T,P) + RT\ln(a). \tag{A.3}$$

Equating the chemical potentials of the gas and aqueous phase gives:

$$\frac{\mu_l^0(T,P) - \mu_l^0(T,P)}{RT} = \ln(\frac{a}{P\Phi y}) \tag{A.4}$$

and in terms of the equilibrium constant

$$\frac{\mu_l^0(T,P) - \mu_l^0(T,P)}{RT} = \ln(K^0). \tag{A.5}$$

Here $k_H = \frac{Nw}{K^0}$ is substituted in equation A.5 and is equated with equation A.4 to obtain equation A.6. The definition for k_H was obtained from John M. Prausnitz et al. [30] 1986 as

$$\frac{Nw}{k_H} = \frac{a}{P\Phi y}, \tag{A.6}$$

where Nw is the number of moles per kilogram of water and k_H is henry's constant. Further more the activity value a can be substituted by $a = Nw\gamma x$, which is a reasonable assumption because the solubility of the gas components is small [54]. The effect of salt is accounted for in the activity coefficient of the gas components as will be explained in more detail later on. Substitution of the activity parameter results the final expression of the thermodynamic phase equilibrium

$$P\Phi y = k_H\gamma x. \tag{A.7}$$

A.2. Derivation of water equilibrium constant

At equilibrium, the equilibrium reaction of water as shown by equation A.8 will have the equilibrium constant described by:

$$H_2O_{(l)} \Leftrightarrow H_2O_{(g)}, \tag{A.8}$$

$$f_{H2O} = \Phi_{H2O} y_{H2O} P = K_{H2O} a_{H2O}(l). \tag{A.9}$$

Where f is the fugacity of water in the gas phase and a is the activity of water in the aqueous phase. K_{H_2O} is the equilibrium constant of water is dependant on temperature and pressure as is described by equation A.10. The exponential part of the formulation is referred to by Spycher et al. [54] as a correction factor that needs to be applied to the equilibrium constant when pressures deviate significantly from the reference pressure. This correction is also known as the Poynting factor, which is a correction factor for the effect of pressure on the condensed phase [30]. The Poynting factor is shown as:

$$K(T,P) = K^0_{H_2O}(T,P_0) exp\Big[\frac{(P-P_0)V_{H_2O}}{RT}\Big]. \tag{A.10}$$

By combining equations 4.14,A.9 and A.10 the following expression for the gaseous molar fraction of H_2O is obtained:

$$y_{H_2O} = \frac{K^0_{H_2O} a_{H_2O}}{\Phi_{H_2O} P} \exp\Big[\frac{(P-P_0)V_{H_2O}}{RT}\Big]. \tag{A.11}$$

In the temperature and pressure range we are interested (5-110 $°C$, 0-600 bar), the solubility of gas in water is assumed to be low, so the activity of the water component can be approximated by its molar fraction in the aqueous phase. The substitution of the molar fraction of H_2O in the aqueous phase (x_{H_2O}) for the activity of water (a_{H_2O}) results in:

$$\Phi_{H_2O} P y_{H_2O} = K^0_{H_2O} x_{H_2O} exp\Big[\frac{(P-P_0)V_{H_2O}}{RT}\Big]. \tag{A.12}$$

By rewriting this equation a formulation for the equilibrium constant of water is obtained

$$K_{H_2O} = \frac{y_{H_2O}}{x_{H_2O}} = \frac{K^0_{H_2O}}{\Phi_{H_2O} P} exp\Big[\frac{(P-1)V_{H_2O}}{RT}\Big], \tag{A.13}$$

where K^0_{H2O} is the equilibrium constant of H_2O at the reference pressure of 1 bar, T is temperature in Kelvin. V_{H_2O} is the molar volume of water.

A.3. Derivation of Henry's Constant

Henry's constant is obtained using the viral-like correlation of Akinfiev and Diamond [5] given by:

$$\ln(h_i) = (1-\eta)\ln(f^0_{H2O}) + \eta \ln\Big(\frac{RT}{Mw_{H2O}}\rho^0_{H2O}\Big) + 2\rho^0_{H2O}\Delta B, \tag{A.14}$$

where temperature T is expressed in $[Kelvin]$, η is a constant for each gas component dissolved in water [-], the density of water ρ_{H_2O} is expressed in $[g/cm^3]$, R is the gas constant and ΔB is the difference in interaction between dissimilar molecules and that of identical solvent molecules expressed in $[g/cm3]$.

The last parameter, ΔB, can be derived as

$$\Delta B = \tau + \beta\Big(\frac{10^3}{T}\Big)^{0.5}, \tag{A.15}$$

where τ $(cm^3 g^{-1})$ and β $(cm^3 K^{0.5} g^{-1})$ are adjustable parameters. Values of τ, η and β can be found in reference table A.1.

Gas	η	τ	β
CO_2	-0.114535	-5.279063	6.187967
H_2S	0.77357854	0.27049433	0.27543436
N_2	-0.008194	-5.175337	6.906469
CH_4	-0.092248	-5.779280	7.262730

Table A.1: The calibrated input parameters for Henry's constant for various components

The fugacity of water is determined by correlation developed by King et al. [34] shown in equation A.16:

$$f^0_{H_2O} = P_s \exp\left[\frac{Vm_{H_2O}(P-P_s)}{\rho_{H_2O}RT}\right]. \tag{A.16}$$

Where the saturation pressure (P_s) is obtained using a correlation developed by Shibue [51] shown as:

$$\ln\frac{P_s}{P_c} = \frac{T_c}{T}[a_1\tau + a_2\tau^{1.5} + a_3\tau^3 + a_4\tau^{3.5} + a_5\tau^4 + a_6\tau^{7.5}], \tag{A.17}$$

where $\tau = 1 - \frac{T}{T_c}$ and T_c is the critical temperature of a component. The density of pure water is determined by correlation of Fine and Millero [19] shown by:

$$V^p = V^0 - \frac{V^0 P}{B + A_1 P + A_2 P}, \tag{A.18}$$

where $V^p = \frac{1}{\rho}$, resulting in:

$$\frac{1}{\rho_{H_2O}} = V^0 - \frac{V^0 P}{B + A_1 P + A_2 P}.. \tag{A.19}$$

Density here is the density of pure water in $[cm^3/g]$. V^0, B and A_1A_2 are empirical parameters dependant of Temperature in Celsius.

Parameter V^0, B, A_1 and A_2 are defined in equations A.20, A.21, A.22 and A.23 respectively as:

$$V^0 = \frac{1 + 18.159725 \times 10^{-3}\cdot}{0.9998396 + 18.224944 \cdot 10^{-3}\theta - 7.922210 \cdot 10^{-6}\theta^2 - 55.4486 \cdot 10^{-9}\theta^3 + 149.7562 \cdot 10^{-12}\theta^4 - 393.2952 \cdot 10^{-15}\theta^5}, \tag{A.20}$$

$$B = 19654.320 + 147.037\theta - 2.21554\theta^2 + 1.0478 \times 10^{-2}\theta^3 - 2.2789 \times 10^{-5}\theta^4, \tag{A.21}$$

$$A_1 = 3.2891 - 2.3910 \times 10^{-3}\theta + 2.8446 \times^{-4} \theta^2 - 2.8200 \times 10^{-6}\theta^3 + 8.477 \times 10^{-12}\theta^4, \tag{A.22}$$

$$A_2 = 6.245 \times 10^{-5} - 3.913 \times 10^{-6}\theta - 3.499 \times 10^{-8}\theta^2 + 7.942 \times 10^{-10}\theta^3 - 3.299 \times 10^{-12}\theta^4, \tag{A.23}$$

where θ is the temperature in degrees Celsius.

A.4. Derivation of Activity Coefficient

The Activity coefficient is a factor used to account for deviations from ideal behaviour in a mixture of chemical substances. In an ideal solution the microscopic interaction between a pair of chemical components are the same and as a result properties of the mixture can be expressed as simple concentrations and partial pressures of the components present (raoults law for an ideal solution) as:

$$p_i = p_i^* x_i. \tag{A.24}$$

Deviations from ideality are realized by modifying the concentration by a so called activity coefficient. Expressions involving gasses can be modified for non-ideality by scaling partial pressures using the fugacity coefficient. Raoults law for non-ideal mixing then becomes (modified raoults law) as:

$$y_i \Phi_{p,i} P = x_i \gamma_i P_i^*, \tag{A.25}$$

where P_i^* is the vapor pressure of pure component i.

The activity coefficients are obtained using the approach used by the correlation of Pitzer [47], shown in equation A.26:

$$\ln \gamma_i = \sum_c 2m_c \lambda_{i-Na} + \sum_a 2m_a \lambda_{i-Cl} + \sum_c \sum_a 2m_a m_c \xi_{i-Na-Cl}. \tag{A.26}$$

Here m_c and m_a are cation and anion molalities, λ_{i-Na} and $\xi_{i-Na-Cl}$ are second and third order interaction parameters respectively, both depend on pressure and temperature, λ_{i-Cl} is assumed to be equal to zero. λ_{i-Na} and $\xi_{i-Na-Cl}$ are calculated using:

$$Par(T,P) = c_1 + c_2 T + \frac{c_3}{T} + c_4 P + \frac{c_5}{P} + c_6 \frac{P}{T} + c_7 \frac{T}{P^2} + \frac{c_8 P}{630 - T} + c_9 T \ln(P) + c_1 0 \frac{P}{T^2}. \tag{A.27}$$

Values for constant c for the second-order (λ_{i-Na}) and third-order ($\xi_{i-Na-Cl}$) interaction parameters can be found in tables A.2 and A.3 respectively.

Constant	λ_{CO_2-Na}	λ_{N_2-Na}	λ_{H_2S-Na}	λ_{CH_4-Na}
c_1	-0.0652869	-2.0939363	1.03658689	-5.7066455E-01
c_2	1.6790636E-04	3.1445269E-03	-1.1784797E-03	7.2997588E-04
c_3	40.838951	3.9139160E+02	-1.7754826E+02	1.5176903E+02
c_4	0	-2.9973977E-07	-4.5313285E-04	3.1927112E-05
c_5	0	0	0	0
c_6	-3.9266518E-02	-1.5918098E-05	0	-1.6426510E-05
c_7	0	0	0	0
c_8	2.1157167E-02	0	0	0
c_9	6.5486487E-06	0	0	0
c_{10}	0	0	0.47751650E+02	0

Table A.2: The Calibrated second-order interaction parameters (λ) for various components used for calculation of the activity coefficient.

Constant	$\zeta_{CO_2-Na-Cl}$	$\zeta_{N_2-Na-Cl}$	$\zeta_{H_2S-Na-Cl}$	$\zeta_{CH_4-Na-Cl}$
c_1	-1.144624E-02	-6.3981853E-03	0.010274152	-2.9990084E-03
c_2	2.8274958E-05	0	0	0
c_3	0	0	0	0
c_4	0	0	0	0
c_5	0	0	0	0
c_6	1.3980876E-02	0	0	0
c_7	0	0	0	0
c_8	-1.4349005E-02	0	0	0
c_9	0	0	0	0
c_{10}	0	0	0	0

Table A.3: The Calibrated second-order interaction parameters (ζ) for various components used for calculation of the activity coefficient.

A.5. Derivation of empirical parameters for initial k-value estimation

As described in chapter 4 section 4.2.3 the Raoult's Law used to determine the initial k-value can be simplified to equation 4.23. Here the saturation pressure of each component i can be described by:

$$p_i^{sat} = P_{c,i} \exp[a_1 + \omega_i a_2]. \tag{A.28}$$

Where ω_i is the accentric factor of each component and the empirical parameters a_1 and a_2 are defined by:

$$a_1 = a_{11} + a_{12}\frac{T_{c,i}}{T} + a_{13} \ln\frac{T}{T_{c,i}} + a_{14}\frac{T^6}{T_{c,i}^6}, \tag{A.29}$$

$$a_2 = a_{21} + a_{22}\frac{T_{c,i}}{T} + a_{23} \ln\frac{T}{T_{c,i}} + a_{24}\frac{T^6}{T_{c,i}^6}, \tag{A.30}$$

where T is temperature in Kelvin and P_i^{sat} is the saturation pressure in bar. The parameters given in both equation can be found in table A.4.

a_{11}	5.927140	a_{21}	15.25180
a_{12}	-6.096480	a_{22}	-15.68750
a_{13}	-1.288620	a_{23}	-13.47210
a_{14}	0.169347	a_{24}	0.43577

Table A.4: Empirical parameters used in equations A.29 and A.30

The Antoine equation used to calculate the saturation pressure of water is given by:

$$p_i^{sat} = \exp\left[a_{1,i} - \frac{a_{2,i}}{T + a_{3,i}}\right], \tag{A.31}$$

where the empirical constants are given for water are; a_1 = 12.048399, a_2 = 4030.18245 and a_3 = -38.15.

The inifinite dilution activity coefficient for each component i is described by:

$$\gamma_i^{\infty} = \exp\left[a_1 + a_2 N_i + \frac{a_3}{N_i}\right]. \tag{A.32}$$

Here N_i is the number of carbon atoms in each component i and where the emperical parameters are given in table A.32.

	a_1	a_2	a_3
n-paraffins	0.688	0.642	0
n-primary alcohols	-0.995	0.622	0.558

Table A.5: Empirical parameters used in equations A.32

B

Appendix chapter 5 - Physical Properties

B.1. Derivation of Brine Density

To use the brine solution density correlation, shown in equation B.1, the participating parameters need to be determined by:

$$\rho_b(p,T,C_m) = \rho_{b0}(T,C_m)\exp\left[I_b(p,T,C_m) - I_b(p_0,T,C_m)\right], \tag{B.1}$$

where the brine density at reference pressure (ρ_{b0}) is defined as:

$$\rho_{b0} = \rho_{w0} + D_{Cm,2}(T)C_m^2 + D_{Cm,3/2}(T)C_m^{3/2} + D_{Cm,3}(T)C_m + D_{Cm,1/2}(T)C_m^{1/2}. \tag{B.2}$$

Here $D_{Cm,x}$ are empirically derived parameters (which will be addressed in section B.1.1), C_m is the molality of sodium chloride concentration in $[moles/kg]$ and ρ_{w0} is the density of pure water at reference pressure $70MPa$. The density of pure water at reference pressure is calculated using equation B.3:

$$\rho_{w,0}(T) = \frac{D_{w1}(\frac{T}{100})^2 + D_{w2}(\frac{T}{100}) + D_{w3}}{D_{w4}(\frac{T}{100})^2 + D_{w5}(\frac{T}{100}) + 1}, \tag{B.3}$$

where D_{wx} are empirical constants found in table B.1. From equation B.1 the empirical parameters I_b are derived from the following correlation:

$$I_b(p,T,C_m) = \int_p c_b dp = \frac{1}{E_b(T,C_m)} \ln|E_b(T,C_m)(\frac{p}{p0}) + F_b(T,C_m)|, \tag{B.4}$$

where c_b is the brine compressibility which is calculated using equation B.5:

$$c_b(p,T,C_m) = \left(\frac{1}{p_0}\right)\frac{1}{E_b(T,C_m)(\frac{p}{p_0}) + F_b(T,C_m)}. \tag{B.5}$$

B.1.1. Empirically Derived Parameters

The empirically based parameters D_w,E_w, F_w, E_{Cm} and F_{Cm} are all generated with equation B.6, and the corresponding empirical constants found in tables B.1, B.2 and B.3 as:

$$a(T) = \frac{a_1(\frac{T}{100})^2 + a_2(\frac{T}{100}) + a_3}{a_4(\frac{T}{100})^2 + a_5(\frac{T}{100}) + 1}. \tag{B.6}$$

Here temperature is given by degrees Celsius. The coefficients in equation E_b and F_b are expressed as function of the empirically based parameters as:

$$E_b(T,Cm) = E_w(T) + E_{Cm}(T) * Cm, \tag{B.7}$$

$$F_b(T,Cm) = F_w(T) + F_{C_m,2/3}(T)C_m^{2/3} + F_{C_m,1}(T)C_m + F_{C_m,1/2}(T)C_m^{1/2}. \tag{B.8}$$

Note that the brine solution density by Spivey correlations is calculated in $[g/cm3]$*, so before implementing Garcia correlation the density must be multiplied by 1000 to obtain results in* $[kg/m3]$.

i	$D_w(T)$	$E_w(T)$	F_w(T)
1	-0.127213	4.221	-11.403
2	0.645486	-3.478	29.932
3	1.03265	6.221	27.952
4	-0.070291	0.5182	0.20684
5	0.639589	-0.4405	0.3768

Table B.1: Coefficients for equation of state for pure water

i	$E_{C_m}(T)$	$F_{C_m,3/2}(T)$	$F_{C_m,1}$(T)	$F_{C_m,1/2}(T)$
1	0	-1.409	0	-0.1127
2	0	-0.361	5.614	0.2047
3	0.1353	-0.2532	4.6782	-0.0452
4	0	0	-0.307	0
5	0	9.216	2.6069	0

Table B.2: Coefficients for Brine compressibility

i	$D_{C_m,2}(T)$	$D_{C_m,3/2}(T)$	$D_{C_m,1}$(T)	$D_{C_m,1/2}(T)$
1	-7.925 $\times 10^{-5}$	1.0998 $\times 10^{-3}$	-7.6402 $\times 10^{-3}$	3.746 $\times 10^{-4}$
2	-1.93 $\times 10^{-6}$	-2.8755 $\times 10^{-3}$	3.6963 $\times 10^{-2}$	-3.328 $\times 10^{-4}$
3	-3.4254 $\times 10^{-4}$	-3.5819 $\times 10^{-3}$	4.36083 $\times 10^{-2}$	-3.346 $\times 10^{-4}$
4	0	-0.72877	-0.333661	0
5	0	1.92016	1.185685	0

Table B.3: Coefficients for density of brine as function of temperature at 70 MPa

B.2. Derivation of parameters for aqueous phase viscosity

The polynomial parameters in equation 5.11,A, B and C, are dependant on temperature which are derived using the following correlations:

$$A = a_0 + a_1T + a_2T, \tag{B.9a}$$

$$B = b_0 + b_1T + a_2T^2, \tag{B.9b}$$

$$C = c_0 + c_1T, \tag{B.9c}$$

where T is in $[K]$. The parameters a_i, b_i and c_i derived from a large number of experimental data and can be found in table B.4.

The viscosity of water is determined using a simplified version of the formulation of IAPWS. This simplified model was also developed by Mao and Duan [42] as:

$$\ln \mu_{H_2O} = \sum_{i=1}^{5} d_i T^{i-3} + \sum_{i=6}^{10} d_i \rho_{H_2O} T^{i-8}. \tag{B.10}$$

Where density of pure water is already obtained using equation A.19. Parameters d_i can also be found in table B.4

Parameters	$NaCl - H_2O$
a_0	-0.21219213
a_1	$0.13651689x10^{-}2$
a_2	$-0.12191756x10^{-}5$
b_0	$0.69161945x10^{-}1$
b_2	$-0.27292263x10^{-}3$
b_2	$0.20852448x10^{-}6$
c_0	$-0.25988855x10^{-}2$
c_1	$0.77989227x10^{-}5$

i	d_i
1	$0.28853170x10^{7}$
2	$-0.11073577x10^{5}$
3	$-0.90834095x10^{1}$
4	$0.30925651x10^{-1}$
5	$-0.27407100x10^{-4}$
6	$-0.19283851x10^{7}$
7	$0.56216046x10^{4}$
8	$0.13827250x10^{2}$
9	$-0.47609523x10^{-1}$
10	$0.35545041x10^{-4}$

Table B.4: Empirical input constants for equations B.9 and B.10

C

Appendix chapter 6

C.1. Validation of Thermodynamic model

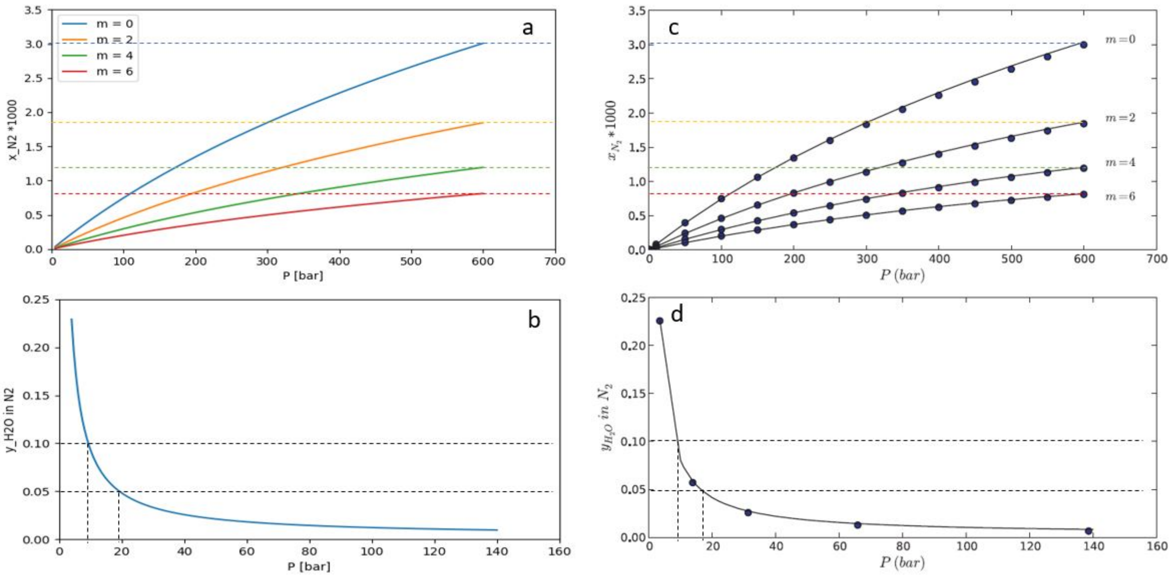

Figure C.1: Validation of liquid mol fraction N_2 at 60 degrees C and gaseous mol fraction H_2O at 366.45 Kelvin. (a) & (b) show the results generated by the developed F-A model, (c) & (d) show the results found in literature, [58]

The results presented in figures C.1 and C.2 are produced by the single component injection of N_2 and CH_4 respectively. In both figures the liquid mol fraction is plotted for pressures up to 600 bar for a range of salinity's and at a temperature of 60°C. The vapour mol fraction of H_2O in both figures C.1 and C.2 are generated a respectively at 366.45 and 377.59 Kelvin. The symbols found in the literature results are experimental data points used for validation and can be found in Ziabakhsh-Ganji and Kooi [58]. On visual comparison the model produces results that are very compatible with literature.

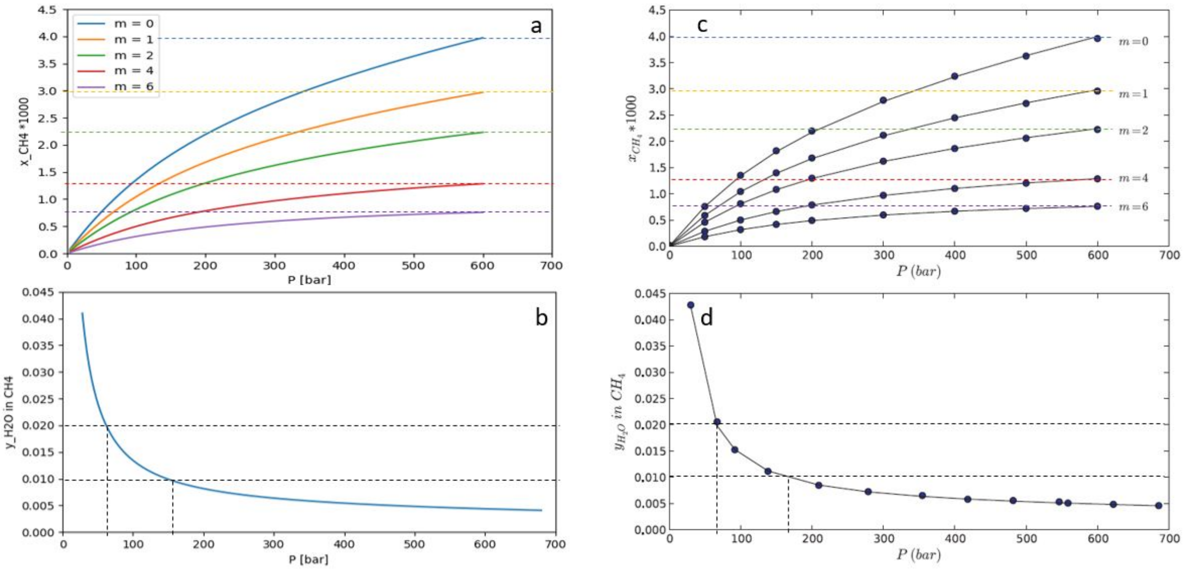

Figure C.2: Validation of liquid mol fractions of CH_4 for a range of salinity's at 60 degrees C and vapour mol fractions of H_2O at 377.59 kelvin. (a) & (b) show the results generated by the developed F-A model, (c) & (d) show the results found in literature, [58]

C.2. Additional plume migration results

C.2.1. Impure gas plume migration

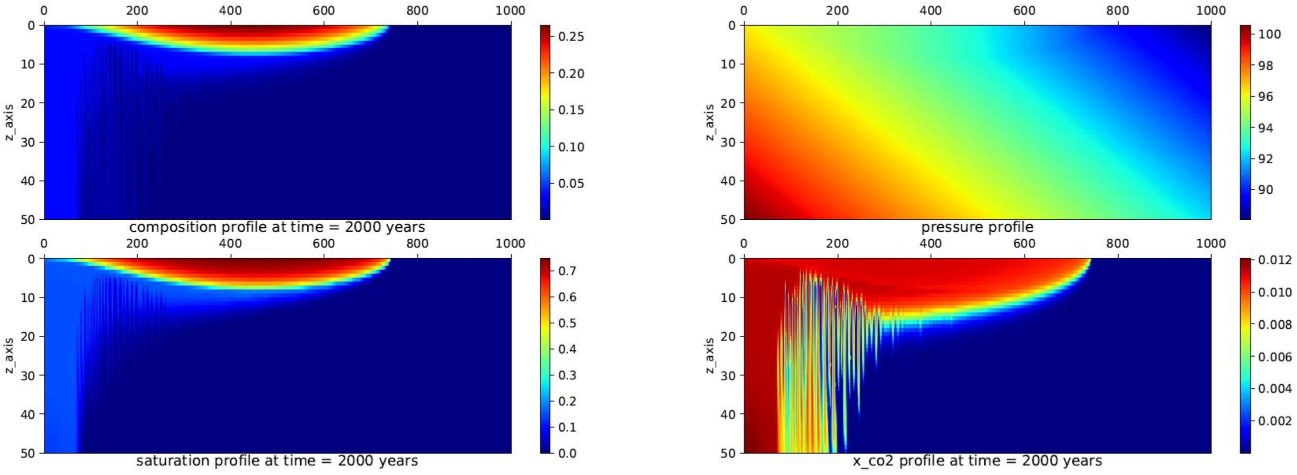

Figure C.3: Composition, pressure,saturation and dissolved CO_2 profiles for post-injection migration for an impure CO_2 gas mixture. Results include gravity, diffusion and capillarity physics. Gas mixture is consist of CO_2, N_2 and CH_4, [0.8, 0.09, 0.09].

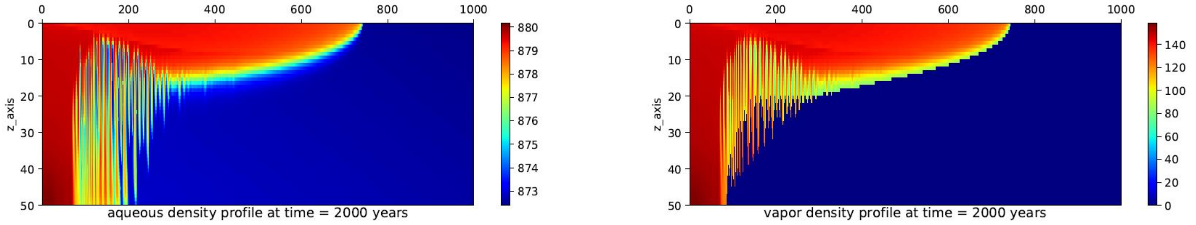

Figure C.4: Phase density profiles for post-injection migration for an impure CO_2 gas mixture. Results include gravity, diffusion and capillarity physics. Gas mixture is consist of CO_2, N_2 and CH_4, [0.8, 0.09, 0.09].

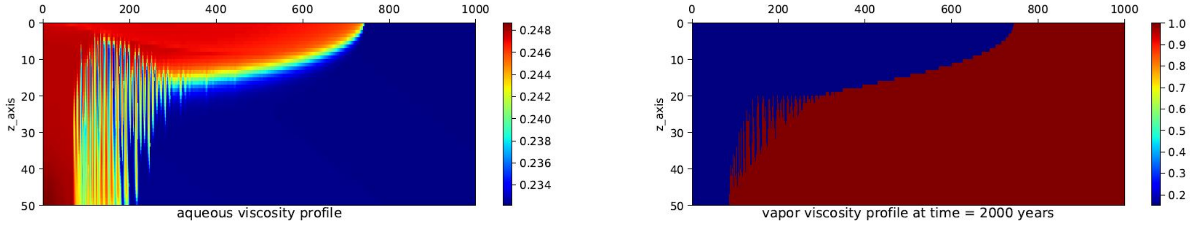

Figure C.5: Viscosity profiles for post-injection migration for an impure CO_2 gas mixture. Results include gravity, diffusion and capillarity physics. Gas mixture is consist of CO_2, N_2 and CH_4, [0.8, 0.09, 0.09].

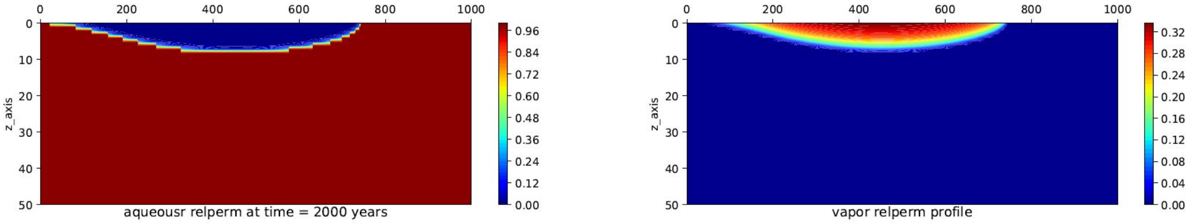

Figure C.6: Relative permeability profiles for post-injection migration for an impure CO_2 gas mixture. Results include gravity, diffusion and capillarity physics. Gas mixture is consist of CO_2, N_2 and CH_4, [0.8, 0.09, 0.09].

C.2.2. Pure CO_2 gas plume migration

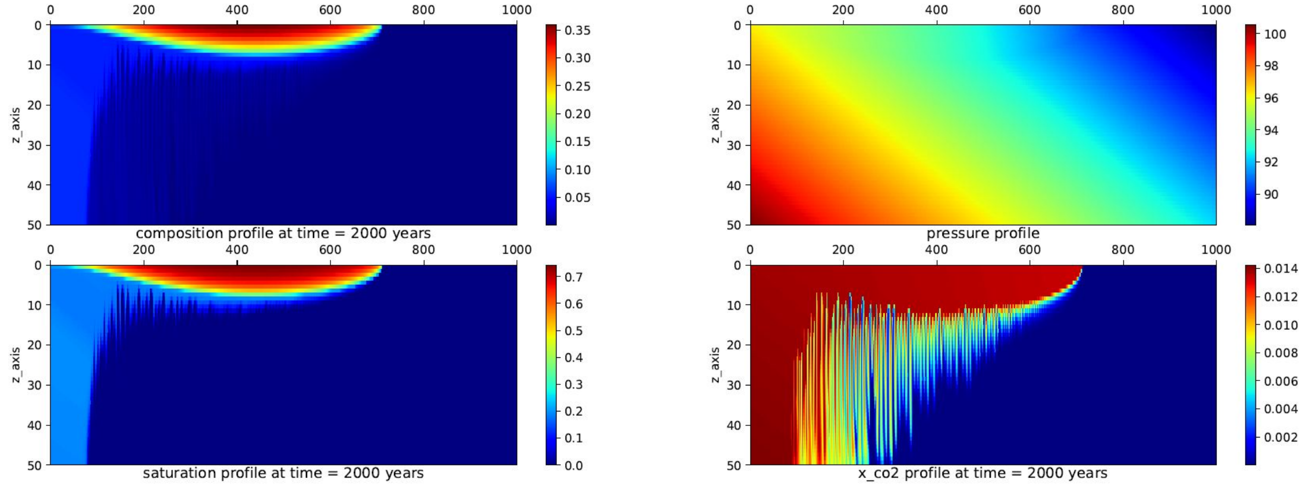

Figure C.7: Composition, pressure,saturation and dissolved CO_2 profiles for post-injection migration for pure CO_2 gas. Results include gravity, diffusion and capillarity physics.

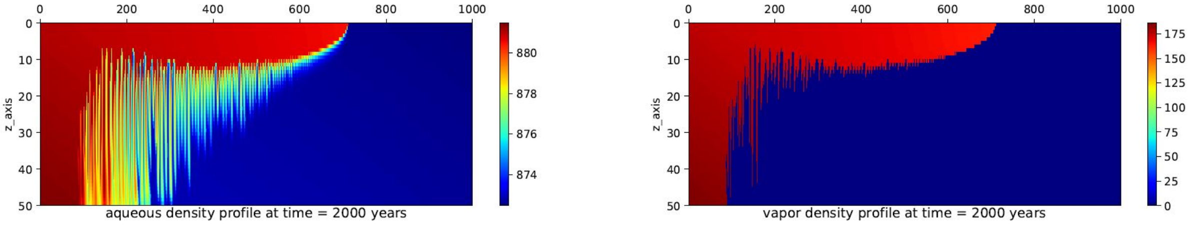

Figure C.8: Phase density profiles for post-injection migration for pure CO_2 gas. Results include gravity, diffusion and capillarity physics.

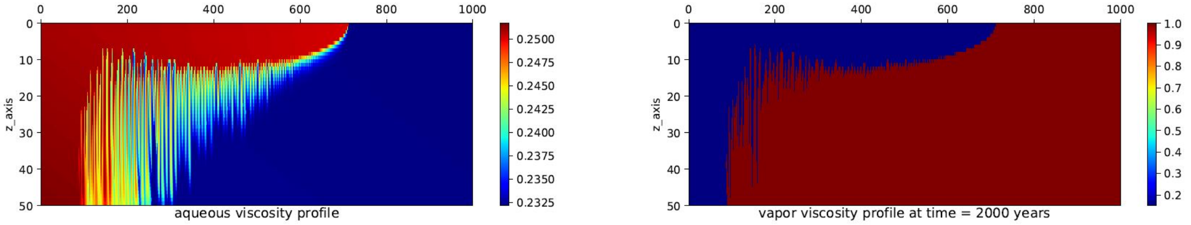

Figure C.9: Viscosity profiles for post-injection migration for pure CO_2. Results include gravity, diffusion and capillarity physics.

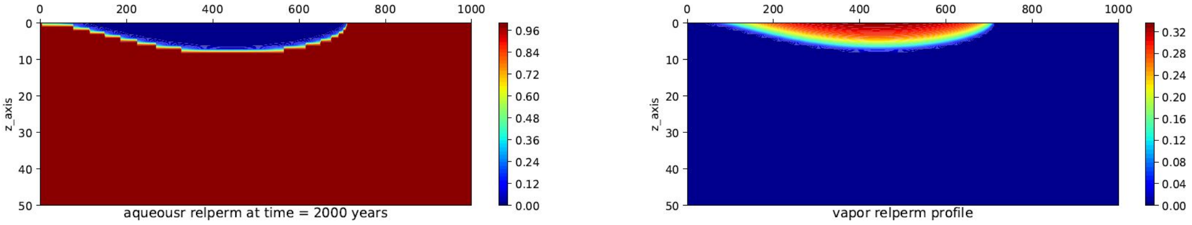

Figure C.10: Relative permeability profiles for post-injection migration for pure CO_2. Results include gravity, diffusion and capillarity physics.

Bibliography

[1] Kyoto Protocol to the United Nations Framework Convention on Climate Change, 11 December 1997. In *Documents in International Environmental Law*, pages 153–178. Cambridge University Press, 6 2012. doi: 10.1017/cbo9781139171380.013.

[2] *Energy Technology Perspectives 2017*. Energy Technology Perspectives. OECD, 6 2017. ISBN 9789264270503. doi: 10.1787/energy{_}tech-2017-en. URL `https://www.oecd-ilibrary.org/energy/energy-technology-perspectives-2017_energy_tech-2017-en`.

[3] Abass A. Olajire. CO2capture and separation technologies for end-of-pipe applicationse A review. *Journal of International Commercial Law and Technology*, 2010. doi: 10.1016/J.ENERGY.2010.02.030.

[4] Akand W. Islam and Eric S. Carlson. Viscosity models and effects of dissolved CO2. 2012.

[5] Nikolay N Akinfiev and Larryn W Diamond. Thermodynamic description of aqueous nonelectrolytes at infinite dilution over a wide range of state parameters. Technical report, 2003.

[6] Rodney John Allam. Purification of Oxyfuel-Derived CO2 for Sequestration or EOR. Technical report, 2006. URL `https://www.researchgate.net/publication/237433042`.

[7] S. Arrhenius. On the Influence of Carbonic Acid in the Air upon the Temperature of the Earth. *Publications of the Astronomical Society of the Pacific*, 9:14, 2 1897. ISSN 0004-6280. doi: 10.1086/121158.

[8] Adam L Ballard. A non-ideal hydrate solid solution model for a multi-phase equilibria program. Technical report, Colorado School of Mines, 2002.

[9] Sally M. Benson and Franklin M. Orr. Carbon dioxide capture and storage. *MRS Bulletin*, 33(4):303–305, 2008. doi: 10.1557/mrs2008.63.

[10] R. Byron Bird and Daniel J. Klingenberg. Multicomponent diffusion-A brief review. *Advances in Water Resources*, 62:238–242, 2013. ISSN 03091708. doi: 10.1016/j.advwatres.2013.05.010.

[11] Mai Bui, Claire S. Adjiman, André Bardow, Edward J. Anthony, and Andy Boston. Carbon capture and storage (CCS): The way forward, 2018.

[12] C P W Christiaanse. Offshore transport, conditioning and storage of Carbon Dioxide. Technical report, TU Delft, 2017. URL `http://repository.tudelft.nl/`.

[13] Holger Class, Anozie Ebigbo, Rainer Helmig, Helge K. Dahle, Jan M. Nordbotten, Michael A. Celia, Pascal Audigane, Melanie Darcis, Jonathan Ennis-King, Yaqing Fan, Bernd Flemisch, Sarah E. Gasda, Min Jin, Stefanie Krug, Diane Labregere, Ali Naderi Beni, Rajesh J. Pawar, Adil Sbai, Sunil G. Thomas, Laurent Trenty, and Lingli Wei. A benchmark study on problems related to CO2 storage in geologic formations : Summary and discussion of the results. *Computational Geosciences*, 13(4):409–434, 12 2009. doi: 10.1007/s10596-009-9146-x.

[14] Ding-Yu Peng and Donald B. Robinson. A New Two-Constant Equation of State. Technical report, 1973.

[15] Z. et al. Duan, N. Moller, J. Greenberg, and J. H. Weare. The prediction of methane solubility in natural waters to high ionic strength from 0 to 250°C and from 0 to 1600 bar. *Geochimica et Cosmochimica Acta*, 56(12):4303, 1 1992. doi: 10.1016/0016-7037(92) 90271-j.

[16] Zhenhao Duan and Rui Sun. An improved model calculating CO 2 solubility in pure water and aqueous NaCl solutions from 273 to 533 K and from 0 to 2000 bar. Technical report, 2003. URL `www.elsevier.com/locate/chemgeo`.

[17] Ali Akbar Eftekhari, Hedzer Van Der Kooi, and Hans Bruining. Exergy analysis of underground coal gasification with simultaneous storage of carbon dioxide. *Energy*, 45(1): 729–745, 2012. ISSN 03605442. doi: 10.1016/j.energy.2012.07.019.

[18] M. T. Elenius, D. V. Voskov, and H. A. Tchelepi. Interactions between gravity currents and convective dissolution. *Advances in Water Resources*, 83:77–88, 9 2015. ISSN 03091708. doi: 10.1016/j.advwatres.2015.05.006.

[19] Rana A. Fine and Frank J. Millero. Compressibility of water as a function of temperature and pressure. *The Journal of Chemical Physics*, 59(10):5529–5536, 1973. ISSN 00219606. doi: 10.1063/1.1679903.

[20] Jean-Baptiste Joseph Fourier. On the Temperatures of the Terrestrial Sphere and Interplanetary Space. Technical report, 1824. URL `www.wmc.care4free.net/sci/fourier`.

[21] Jr Franklin M. Orr. *Theory of Gas Injection processes.* Tie-Line Publications, Holte, Denmark, 1st edition edition, 2007.

[22] Hans-Martin Füssel. Climate change, impacts and vulnerability in Europe 2016 — An indicator-based report. 2016.

[23] G. van Loenen, D.J. Jansen, J. Bruining, and A. Barnhoorn. The effect of impurity of CO 2 stream on enhanced gas dissolution. Technical report, 2017.

[24] Guang-Hua Gao, Zhi-Qiang Tan, and Yang-Xin Yu. Calculation of high-pressure solubility of gas in aqueous electrolyte solution based on non-primitive mean spherical approximation and perturbation theory. Technical report, 1999. URL `www.elsevier.nlrlocaterfluid`.

[25] Julio E Garcia, Escholarship Org, and Julio E García. Publication Date Density of Aqueous Solutions of CO 2 *. Technical report, 2001. URL `https://escholarship.org/uc/item/6dn022hb`.

[26] Allan H. Harvey and John M. Prausnitz. Thermodynamics of high□pressure aqueous systems containing gases and salts. *AIChE Journal*, 35(4):635–644, 1989. ISSN 15475905. doi: 10.1002/aic.690350413.

[27] Christian Hermanrud, Terje Andresen, Ola Eiken, Hilde Hansen, Aina Janbu, Jon Lippard, Hege Nordgård Bolås, Trine Helle Simmenes, Gunn Mari Grimsmo Teige, and Svend Østmo. Storage of CO 2 in saline aquifers-Lessons learned from 10 years of injection into the Utsira Formation in the Sleipner area. In *Energy Procedia*, volume 1, pages 1997–2004, 2 2009. doi: 10.1016/j.egypro.2009.01.260.

[28] H.H.J. Vreuls. The Netherlands: list of fuels and standard CO 2 emission factors. Technical report, Ministerie VROM, 2004. URL `www.broeikasgassen.nl`.

[29] A. Iranshahr, D. Voskov, and H. A. Tchelepi. Generalized negative-flash method for multiphase multicomponent systems. *Fluid Phase Equilibria*, 299(2):272–284, 12 2010. ISSN 03783812. doi: 10.1016/j.fluid.2010.09.022.

[30] John M. Prausnitz, Reudiger N. Lichtenthaler, and Edmundo Gomes de Azevedo. *Molecular thermodynamics of fluid-phase equilibria.* New Jersey, 1986. ISBN 0-13-599564-7.

[31] J.P. Spivey and W.D. McCain Jr. Estimating Density, Formation Volume Factor, Compressibility, Methane Solubility, and Viscosity for Oilfield Brines at Temperatures From 0 to 275° C, Pressures to 200 MPa, and Salinities to 5.7 mole/kg. Technical report, Schlumberger - Beijing Science Centre, Texas, 2004.

[32] K. Kala and D. Voskov. Parameterization Of Element Balance Formulation In Reactive Compositional Flow And Transport Automatic Differentiation General Purpose Research Simulator (AD-GPRS) View project Simulation And Optimization Of In-Depth Water Diversion View project. 2018. doi: 10.3997/2214-4609.201802113. URL `https://www.researchgate.net/publication/327403611`.

[33] Mark Khait and Denis V. Voskov. Operator-based linearization for general purpose reservoir simulation. *Journal of Petroleum Science and Engineering*, 2017. ISSN 09204105. doi: 10.1016/j.petrol.2017.08.009.

[34] M B King, A Mubarak, and T R Bott. The Mutual Solubilities of Water with Supercritical and Liquid Carbon Dioxide. Technical report, 1992.

[35] I. KRITCHEVSKY and A. ILIINSLAYA. Partial molal volumes of gases dissolved in liquids. *Acta Physicochimica (URSS)*, 1945.

[36] Dennis Y.C. Leung, Giorgio Caramanna, and M. Mercedes Maroto-Valer. An overview of current status of carbon dioxide capture and storage technologies, 2014. ISSN 13640321.

[37] Jun Li and Zhenhao Duan. A thermodynamic model for the prediction of phase equilibria and speciation in the H 2 O-CO 2 -NaCl-CaCO 3 -CaSO 4 system from 0 to 250°C, 1 to 1000 bar with NaCl concentrations up to halite saturation. *Geochimica et Cosmochimica Acta*, 75(15):4351–4376, 8 2011. ISSN 00167037. doi: 10.1016/j.gca.2011.05.019.

[38] Jun Li, Lingli Wei, and Xiaochun Li. An improved cubic model for the mutual solubilities of CO2-CH4-H2S-brine systems to high temperature, pressure and salinity. *Applied Geochemistry*, 54:1–12, 3 2015. ISSN 18729134. doi: 10.1016/j.apgeochem.2014.12.015.

[39] C. W. MacMinn, M. L. Szulczewski, and R. Juanes. CO 2 migration in saline aquifers. Part 2. Capillary and solubility trapping. *Journal of Fluid Mechanics*, 688:321–351, 12 2011. ISSN 00221120. doi: 10.1017/jfm.2011.379.

[40] Christopher W. Macminn and Ruben Juanes. Buoyant currents arrested by convective dissolution. *Geophysical Research Letters*, 40(10):2017–2022, 5 2013. ISSN 00948276. doi: 10.1002/grl.50473.

[41] Shide Mao and Zhenhao Duan. A thermodynamic model for calculating nitrogen solubility, gas phase composition and density of the N2-H2O-NaCl system. *Fluid Phase Equilibria*, 248(2):103–114, 10 2006. ISSN 03783812. doi: 10.1016/j.fluid.2006.07.020.

[42] Shide Mao and Zhenhao Duan. The viscosity of aqueous alkali-chloride solutions up to 623 K, 1,000 bar, and high ionic strength. *International Journal of Thermophysics*, 30 (5):1510–1523, 2009. ISSN 0195928X. doi: 10.1007/s10765-009-0646-7.

[43] Shide Mao, Dehui Zhang, Yongquan Li, and Ningqiang Liu. An improved model for calculating CO2 solubility in aqueous NaCl solutions and the application to CO2-H2O-NaCl fluid inclusions. *Chemical Geology*, 347:43–58, 6 2013. ISSN 00092541. doi: 10.1016/j.chemgeo.2013.03.010.

[44] Abass A. Olajire. CO2 capture and separation technologies for end-of-pipe applications - A review, 2010. ISSN 03605442.

[45] J. C.M. Pires, F. G. Martins, M. C.M. Alvim-Ferraz, and M. Simões. Recent developments on carbon capture and storage: An overview. *Chemical Engineering Research and Design*, 2011. ISSN 02638762. doi: 10.1016/j.cherd.2011.01.028.

[46] Mohamed Pourkashanian Robert M. Woolley Richard T.J. Porter, Michael Fairweather. The range and level of impurities in CO2streams from different carbon capture sources. *International Journal of Greenhouse Gas Control 36 (2015) 161–174*, 2015.

[47] P S Z Rogers and K S Pitzer. Lawrence Berkeley National Laboratory Recent Work Title VOLUMETRIC PROPERTIES OF AQUEOUS SODIUM CHLORIDE SOLUTIONS Publication Date. Technical report.

[48] Piers J. Sellers, David S. Schimel, Berrien Moore, Junjie Liu, and Annmarie Eldering. Observing carbon cycle–climate feedbacks from space. *Proceedings of the National Academy of Sciences*, 115(31):7860–7868, 7 2018. ISSN 0027-8424. doi: 10.1073/pnas.1716613115.

[49] Babak Shabani and Javier Vilcáez. Prediction of CO2-CH4-H2S-N2 gas mixtures solubility in brine using a non-iterative fugacity-activity model relevant to CO2-MEOR. *Journal of Petroleum Science and Engineering*, 150:162–179, 2017. ISSN 09204105. doi: 10.1016/j.petrol.2016.12.012.

[50] Babak Shabani and Javier Vilcáez. A fast and robust TOUGH2 module to simulate geological CO2 storage in saline aquifers. *Computers and Geosciences*, 111:58–66, 2 2018. ISSN 00983004. doi: 10.1016/j.cageo.2017.10.012.

[51] Yasuhiro Shibue. Vapor pressures of aqueous NaCl and CaCl2 solutions at elevated temperatures. *Fluid Phase Equilibria*, 213(1-2):39–51, 10 2003. ISSN 03783812. doi: 10.1016/S0378-3812(03)00284-X.

[52] Irina Sin, Vincent Lagneau, and Jérôme Corvisier. Integrating a compressible multicomponent two-phase flow into an existing reactive transport simulator. *Advances in Water Resources*, 100:1339–1351, 2 2017. ISSN 03091708. doi: 10.1016/j.advwatres.2016.11.014.

[53] Nicolas Spycher and Karsten Pruess. CO 2-H 2 O Mixtures in the Geological Sequestration of CO 2. II. Partitioning in Chloride Brines at 12−100°C and up to 600 bar. Technical report, 2004.

[54] Nicolas Spycher, Karsten Pruess, and Jonathan Ennis-King. CO2-H2O mixtures in the geological sequestration of CO2. I. Assessment and calculation of mutual solubilities from 12 to 100°C and up to 600 bar. *Geochimica et Cosmochimica Acta*, 67(16):3015–3031, 8 2003. ISSN 00167037. doi: 10.1016/S0016-7037(03)00273-4.

[55] UNFCCC. Adoption of the Paris Agreement. Technical report, 2015.

[56] United Nations. United nations framework convention on climate change. Technical report. Technical report, United Nations, New York, 1992.

[57] Curtis H Whitson and Michael L Michelsen. The negative flash. Technical report, 1989.

[58] Zaman Ziabakhsh-Ganji and Henk Kooi. An Equation of State for thermodynamic equilibrium of gas mixtures and brines to allow simulation of the effects of impurities in subsurface CO2 storage. *International Journal of Greenhouse Gas Control*, 11(SUPPL): 21–34, 2012. ISSN 17505836. doi: 10.1016/j.ijggc.2012.07.025.

[59] Zaman Ziabakhsh-Ganji and Henk Kooi. Sensitivity of the CO2 storage capacity of underground geological structures to the presence of SO2 and other impurities. *Applied Energy*, 135:43–52, 12 2014. ISSN 03062619. doi: 10.1016/j.apenergy.2014.08.073.

[60] Mohsen Zirrahi, Reza Azin, Hassan Hassanzadeh, and Mahmood Moshfeghian. Mutual solubility of CH 4, CO 2, H 2S, and their mixtures in brine under subsurface disposal conditions. *Fluid Phase Equilibria*, 324:80–93, 6 2012. ISSN 03783812. doi: 10.1016/j.fluid.2012.03.017.

[61] You-Xiang Zuo, Tian-Min Guot, and Beijing Graduate School. Extension of the patelteja equation of state to the prediction of the solubility of natural gas in formation water. Technical report, 1991.